Computer Aided Diagnosis of Emphysema Based on Multi-Slice X-Ray CT Using Multi-Threshold Classification and Bullae Distribution Analysis

March 2010

Tan Kok Liang

A Thesis for the Degree of Ph.D. in Engineering

Computer Aided Diagnosis of Emphysema Based on Multi-Slice X-Ray CT Using Multi-Threshold Classification and Bullae Distribution Analysis

March 2010

Graduate School of Science and Technology

Keio University

Tan Kok Liang

Abstract

Radiologists diagnose emphysema based on the pulmonary function tests results and visual recognition of the computed-tomography (CT) images of the lung. Based on the CT images, radiologists have to imagine the three-dimensional visual representation of the distribution of emphysema in the lung. Accuracy of the diagnosis depends significantly on the radiologist's experience and skill. Therefore, manual diagnosis of emphysema is subjective and laborious.

Classical CT-based methods for measuring emphysema include the pixel index (PI), the mean lung density method (MLD), the bullae (a bulla is a continuous low attenuation area in the CT) index (BI) and texture-based methods. However, these methods are subject to some limitations. The goal of this research is to devise more effective and expressive emphysema describing features. Three methods are proposed to describe the severity and distribution of emphysema. The proposed methods complement the existing set of emphysema describing features contributing to a more informative diagnosis of emphysema. A diagnostic tool that encompasses all the proposed methods is implemented using graphical user interface.

The goal of the first method is to produce a more practical emphysema-quantification algorithm that has higher correlation with the parameters of pulmonary function tests compared to the classical methods. The use of the threshold range from approximately –900 Hounsfield Unit to –990 Hounsfield Unit for extracting emphysema from CT has been reported in many papers. However, in this research, correlation analyses between PIs calculated based on different thresholds and the parameters of pulmonary function tests show that a threshold which is optimal for a particular CT data set might not be optimal for

the other CT data sets due to the subtle radiographic variations in the CT images. Consequently, the author proposes a multi-threshold method that utilizes ten thresholds between and including –900 Hounsfield Unit and –990 Hounsfield Unit for identifying the different potential emphysematous regions in the lung. Subsequently, the author divides the lung into eight sub-volumes. From each sub-volume, the author calculates the ratio of the voxels with intensity below a certain threshold. A total of ten thresholds are used. The respective ratios of the voxels below the ten thresholds are employed as the features for classifying the sub-volumes into four emphysema severity classes. Neural network is used as the classifier. The neural network is trained using 80 training sub-volumes. The performance of the classifier is assessed by classifying 248 test sub-volumes of the lung generated from 31 subjects. Actual diagnoses of the sub-volumes are hand-annotated and consensus-classified by radiologist. The four-class classification accuracy of the proposed method is 89.82%. The sub-volumetric classification results produced in this study encompass not only the information of the local emphysema severity but also the emphysema distribution from the top to the bottom of the lung. The author hypothesizes that besides emphysema severity, the distribution of emphysema severity in the lung also plays an important role in the assessment of the overall functionality of the lung. The author confirms his hypothesis by showing that the proposed sub-volumetric classification results correlate with the parameters of pulmonary function tests better than the classical methods. The author also visualizes emphysema using a technique called the transparent lung model that enables medical experts to observe the distribution of emphysema inside the lung from any orientation.

Features generated from the former texture-based methods are not expressive for describing emphysema. Thus, the author proposes a method called low attenuation gap length matrix (LAGLM) to produce features that are more closely related to the definition of emphysema. The LAGLM method is inspired by but different from the former texture-based methods. Features generated from the LAGLM method are more relevant to emphysema and therefore easier to interpret. The LAGLM method is used to classify the regional

radiographic lung regions into four emphysematous patterns distinguishing, in particular, radiographic patterns that imply obvious or subtle bullous emphysema from those that imply diffuse emphysema or minor destruction of airway walls. Neural network is used for discrimination.

Classical methods including the former texture-based methods are not expressive for describing the distribution of bullae in the lung. Consequently, the author proposes an emphysema describing index called bullae congregation index (BCI) that describes whether bullae gather in a specific area of the lung and form a nearly single mass, and if so, how dense the mass of bullae is in the lung. The BCI is calculated based on the relative distance between every pair of bullae and the sizes of bullae in the lung. The BCI ranges from zero to ten corresponding to sparsely distributed bullae to densely distributed bullae. Four bullae congregation classes are defined based on the BCI. The BCI is especially useful for comparing the distribution of bullae for cases with approximately the same PI, BI or PI and BI.

Contents

List of Abbreviations

ASM	angular second moment
BCI	Bullae Congregation Index
BI	Bullae Index
CNT	contrast
CRR	correlation
DAD	distribution of average distance
DEP	difference entropy
DGD	distribution of gray level difference
DOD	distribution of average difference
DVR	difference variance
EPY	entropy
GLD	gray level distribution
GLF	gray level fluctuation
GLN	gap length non-uniformity
GP	gap percentage
$HGGE$	high gray level gaps emphasis
$HGRE$	high gray level run emphasis
$HTGE$	high threshold gap emphasis
IDM	inverse difference moment
$IM1$	information measure of correlation

$IM2$ ..... information measure of correlation
LDE ..... large difference emphasis
$LDEL$ ..... long distance emphasis for large difference
LGE ..... long gap emphasis
$LGGE$ ..... low gray level gaps emphasis
$LGRE$ ..... low gray level run emphasis
LRE ..... long run emphasis
$LRHGE$ ..... long run high gray level emphasis
$LRLGE$ ..... long run low gray level emphasis
$LTGE$ ..... low threshold gap emphasis
$MEAN$ ..... mean
MLD ..... Mean Lung Density
PI ..... Pixel Index
RLD ..... run length distribution
RP ..... run percentage
SAV ..... sum average
SEP ..... sum entropy
SGE ..... short gap emphasis
SHP ..... sharpness
SMG ..... second moment of DGD
SMO ..... second moment of DOD
SRE ..... short run emphasis
$SRHGE$ ..... short run high gray level emphasis
$SRLGE$ ..... short run low gray level emphasis
SVR ..... sum variance
TD ..... threshold distribution
$TGLD$ ..... thresholded gap length distribution

TGP	thresholded gap percentage
$TLGE$	thresholded long gap emphasis
$TSGE$	thresholded short gap emphasis
VAR	variance
AFC	average four-class classification accuracy
AMFM	Adaptive Multiple Feature Method
BCC	Bullae Congregation Class: radiological consensus-classified bullae congregation class
BE	Bullous Emphysema: visually rough lung tissues that imply severe destruction of airway walls or with big-sized bullae
BEDE	Bullous Emphysema and Diffuse Emphysema: visually rough lung tissues that imply moderate destruction of airway walls or with medium-sized bullae (with or without concomitant small-sized bullae)
COPD	Chronic Obstructive Pulmonary Disease
CT	Computed Tomography
DE	Diffuse Emphysema: visually smooth lung tissues but with diffuse small-sized bullae
$DL_{co}VA$	Diffusing capacity of the Lung for Carbon Monoxide (DL_{co}) divided by the Alveolar Volume (VA)
FEV_1	Forced Expiratory Volume in One Second
$FEV_1\%$	Forced Expiratory Volume in One Second (FEV_1) divided by Forced Vital Capacity (FVC)
FVC	Forced Vital Capacity
GLDM	Gray Level Difference Matrix
GLGLM	Gray Level Gap Length Matrix

GLRLM	Gray Level Run Length Matrix
HU	Hounsfield Unit
LAAs	Low-Attenuation Areas
LAGLM	Low Attenuation Gap Length Matrix
N	Normal: visually smooth lung tissues without apparent bullae
NaN	Not-a-Number
PFTs	pulmonary function tests
SGLDM	Spatial Gray Level Dependence Matrix
SS	Steady-State
SSID	Steady-State Identification algorithm

List of Figures

List of Tables

Chapter 1

Introduction

1.1 Computed tomography

X-ray imaging is a transmission-based technique in which X-rays from a source pass through the patient and are detected either by film or an ionization chamber on the opposite side of the body [1]. Contrast in the image between different tissues arises from differential attenuation of X-rays in the body. For example, X-ray attenuation is particularly efficient in bone, but less so in soft tissues. X-ray attenuation is usually measured in Hounsfield Unit (HU). The HU scale is a linear transformation of the original linear attenuation coefficient measurement into one in which the radiodensity of distilled water at standard pressure and temperature is defined as zero HU [1, 2]. Table 1.1 shows the HU of common substances from the low to high attenuation substance. In planar X-ray radiography, the image produced is a simple two-dimensional projection of the tissues lying between the X-ray source and the film. Planar X-ray radiograph is used for a number of different purposes: intravenous pyelography to detect diseases of the genitourinary tract including kidney stones; abdominal radiography to study the liver, bladder, abdomen, and pelvis; chest radiography for diseases of the lung and broken ribsl and X-ray fluoroscopy (in which images are acquired continuously over a period of several minutes) for a number of different genitourinary and gastrointestinal

Table 1.1: The HU of common substances.

Substance	Hounsfield Unit (HU)
Air	–1000
Fat	–120
Water	0
Muscle	+40
Contrast	+130
Bone	+400

diseases [1].

Planar X-ray radiography of overlapping layers of soft tissue or complex bone structures can often be difficult to interpret, even for a skilled radiologist. In theses cases, X-ray computed tomography (CT) is used. The basic principles of CT are shown in Fig. 1.1 [1]. The X-ray source is tightly collimated to interrogate a thin "slice" through the patient. The source and detectors rotate together around the patient, producing a series of one-dimensional projections at a number of different angles. These data are reconstructed to give a two-dimensional image, as shown on the right of Fig. 1.1. CT images have a very high spatial resolution (∼1mm) and provide reasonable contrast between soft tissues. The major disadvantage of both X-ray and CT imaging is the fact that the technique uses inoizing radiotion. Because ionizing radiation can cause tissue damage, there is a limit on the total radiation dose per year to which a patient can be subjected [1].

Figure 1.2 shows an example of a CT image of the lung.

1.2 Emphysema

Chronic Obstructive Pulmonary Disease (COPD) is a respiratory disorder most commonly caused by smoking. COPD involves progressive airway obstruction with breathlessness,

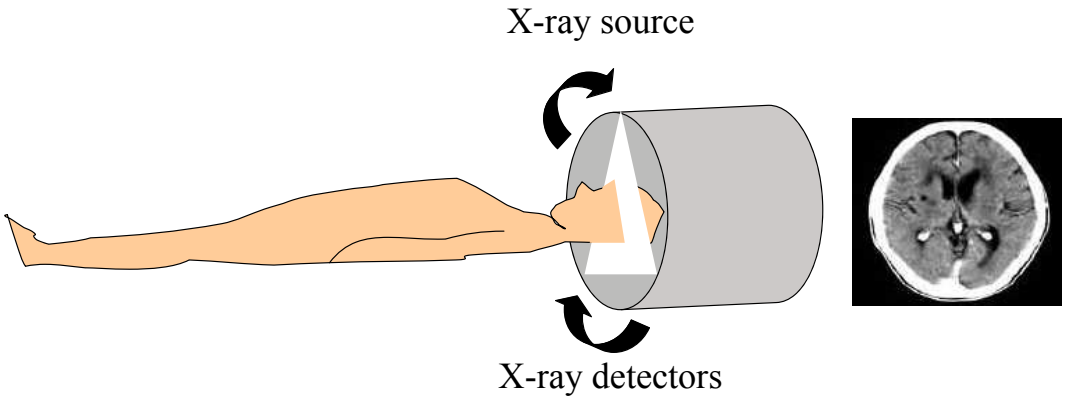

Fig. 1.1: (Left) The principle of computed tomography with an X-ray source and detector unit rotating synchronously around the patient. Data are essentially acquired continuously during rotation. (Right) An example of the single-slice CT image of the brain.

Fig. 1.2: (a) An example of the CT image of the lung. The dark regions surrounded by the bright mass in the center of the image represent the right and left lung.

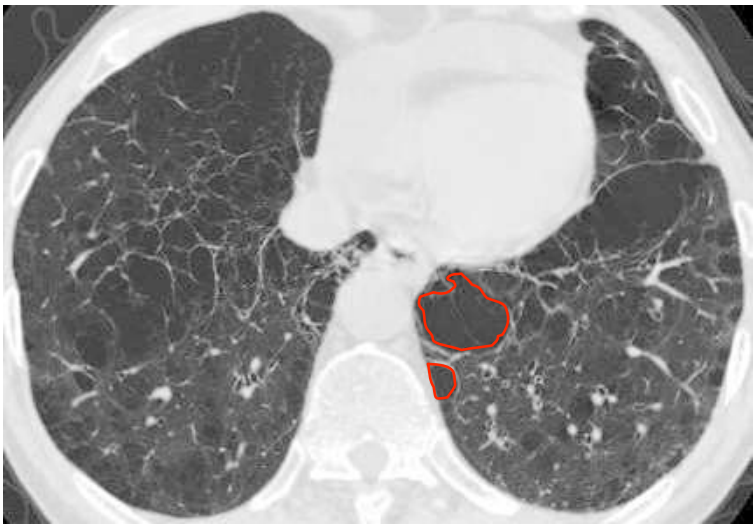

Fig. 1.3: An example of CT image with the examples of LAA outlined in red.

cough and sputum production and increasing frequency and severity of exacerbations [3]. COPD is a major cause of chronic morbidity and mortality throughout the world. Many people suffer from this disease for years and die prematurely of it or its complications.

COPD refers to chronic bronchitis and emphysema, two commonly co-existing diseases of the lung. Emphysema is defined histologically as the enlargement of the air spaces distal to the terminal bronchioles, with destruction of their walls [4]. The destruction of airway walls results in air-filled regions in the lung. These air-filled regions represent the emphysematous regions. Since X-ray attenuation for air is low, the emphysematous regions appear as continuous low-attenuation areas (LAAs) in CT image as shown in Fig. 1.3 where two examples of LAAs are outlined in red. The appearances of LAAs in CT resemble dark holes. An LAA is also called as a bulla [5, 6]. From the CT, three of the most important features of LAAs are the size of LAAs, the pixel intensity of LAAs and the distribution of LAAs.

Emphysema is the physical destruction of lung tissue that results in obstruction to air flow and development of enlarged air sacs [7, 8]. It is a smoking related disease that causes progressive obstruction of the airways and destruction of lung tissue. Because the airway

is obstructed, more energy is required to ventilate the lung. The patient will experience shortness of breath, and as the disease progresses, will become progressively limited in the ability to exercise [7].

1.3 Standard clinical diagnosis of emphysema

Spirometry (meaning the measuring of breath) [7, 8, 9, 10] is the most common of the pulmonary function tests (PFTs). Spirometry parameters such as $FEV_1\%$ predicted [Forced Expiratory Volume in One Second (FEV_1) divided by Forced Vital Capacity (FVC)] and FEV_1 (see Table A.3 in Appendix A.4) are often used as the guidelines for classifying emphysema severity into five classes (see Table A.4 in Appendix A.5). Radiologists usually diagnose emphysema based on the following four aspects:

1. Pulmonary function tests (PFTs) results.
2. Visual recognition of the radiographic patterns of emphysema in CT images.
3. Presence of chronic respiratory symptoms.
4. Medical knowledge about emphysema.

The following features are observed when radiologists recognize emphysema visually from the lung CT:

1. Regional radiographic emphysematous patterns (micro observation).
2. Bullae sizes.
3. Bullae distribution in the lung (macro observation).

However, radiographic patterns observed from CT images are often varied and subtle and that human observer does not usually see early abnormal lung pathology on CT images [11]. Since it is extremely laborious and time-consuming to examine all CT images in the patient's

data set, radiologists usually diagnose emphysema severity by gathering information from just a few CT images that originate from the top, middle and bottom of the lung alongside extensive reference to PFTs results augmented by medical knowledge. Most of the time, radiologists have to imagine the distribution of emphysema severity over the entire lung in three dimensions based on the mere 2D information gathered from a few CT slices. The problems that arise from this standard practice of diagnosis are elaborated as follows.

1. The best tests for determining the presence of emphysema and managing its response to treatment are PFTs. The gold standard test is spirometry. Spirometry test measures the amount (volume) and/or speed (flow) of air that can be inhaled and exhaled [9]. However, the maneuver of spirometry test is highly dependent on patient's cooperation and effort, and is normally repeated at least three times to ensure reproducibility. Since spirometry test results are dependent on patient's cooperation, the test values: FEV_1 and FVC, can only be underestimated, never overestimated. Hence, review of just the PFT's parameters is not sufficient for an accurate diagnosis of emphysema.

2. There is always a possibility that radiologists might miss the CT slices where the significant emphysematous destructions are located.

3. Accurate examination of CT images requires experience. Consequently, the variance of accuracy between the diagnosis produced by an experienced radiologist and that produced by an unexperienced radiologist can not be ignored.

Automated computer aided diagnosis of emphysema [12] is in demand because it helps medical experts verify their findings and thus shorten the time and labor involved in the diagnosis. Nowadays, researchers are making effort to devise not only new emphysema describing indices and but new computer graphics that are more expressive and easy to interpret to assist medical experts to achieve objective, accurate and informative diagnosis of emphysema. The following are brief introductions of the classical methods and the author's proposed methods for diagnosing emphysema.

1.4 Classical computer aided diagnosis of emphysema

Classical CT-based methods for quantifying emphysema include:

1. Pixel Index (PI).
2. Mean Lung Density (MLD).
3. Bullae Index (BI).
4. Texture-based methods.
5. Other approaches.

Among these methods, two of the most widely used methods for evaluating emphysema severity are PI and BI. This is because these two emphysema describing indices are more direct and easier to interpret.

1.4.1 Pixel Index (PI)

Many papers have proposed objective methods of quantification of emphysema by focusing on the overall lung density histogram (number of pixels falling below a threshold) [13, 14, 15] in the image. One of the most widely used classical CT-based methods for assessing emphysema severity is PI. Figure 1.4 shows an example of the histogram of the lung area in the CT image. PI represents the percentage of lung area that has pixel values lower than a certain limit value [14]. Pixels below the limit are thought to be the air-filled regions [16] in the lung and therefore represent the emphysematous regions. Continuous pixels below the limit are considered as low attenuation areas (LAAs). LAAs represent the emphysematous lesions in the CT. Consequently, PI describes the amount of air presented in the CT and thus detects the extent of emphysematous lesions [15].

The advantage of PI is that it is a simple and direct emphysema describing index that is easy to calculate and interpret. However, PI is susceptible to the problems of averaging

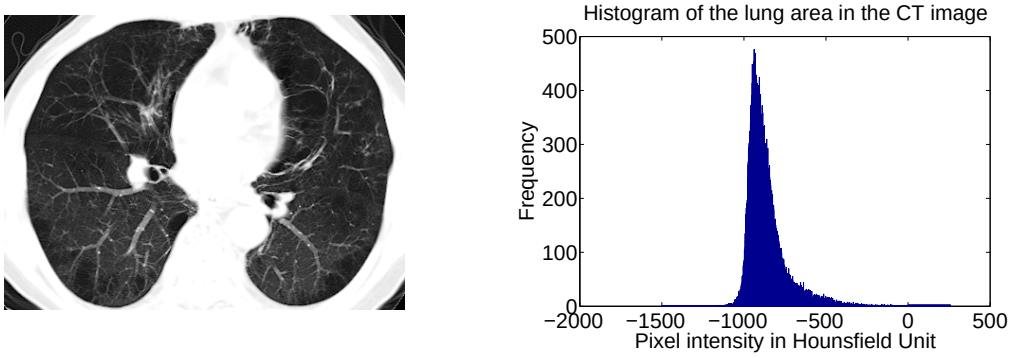

(a) (b)

Fig. 1.4: An example of the histogram of the lung area in the CT image.

effect [6]. For instance, PI of a lung with a large number of small-sized diffuse LAAs might approximate that of a lung with a small number of big-sized LAAs. As a result, PI is unable to discriminate the different sizes of bullae and the distribution of bullae in the CT. It is just a general emphysema describing index that indicates the extent of emphysema severity.

1.4.2 Mean Lung Density (MLD)

MLD [17, 18, 19] represents the fifth or tenth percentile of the CT histogram data [20, 21]. Higher MLD indicates more severe emphysema. MLD is also an index that indicates emphysema severity. It is unable to discriminate the different sizes of bullae and the distribution of bullae.

1.4.3 Bullae Index (BI)

Bullae* index proposed by Blechschmidt [6], is derived by extending PI so that it is enabled to differentiate between small, medium, and large bullae. Blechschmidt sorted bullae into four size classes [22] and calculated how much area the different classes take up of all low-

*Bullae are continuous low-attenuation areas in CT image. They represent the air-filled regions in the lung. Bullae are regarded as emphysematous lesions.

attenuation pixels in the lung region. BI is not a texture-based method. BI proposed by Blechschmidt [6] used –930 HU as the threshold for extracting bullae. The calculation of BI is described as follows:

$$BI = (\frac{g_2 + 2 \times g_3 + 3 \times g_4}{2.4}), \tag{1.1}$$

where

$$g_2 = \begin{cases} PARC_2 & : 0 \leq PARC_2 \leq 4, \\ 4 & : PARC_2 > 4, \end{cases} \tag{1.2}$$

$$g_3 = \begin{cases} PARC_3 & : 0 \leq PARC_3 \leq 4, \\ 4 & : PARC_3 > 4, \end{cases} \tag{1.3}$$

$$g_4 = \begin{cases} PARC_4 & : 0 \leq PARC_4 \leq 4, \\ 4 & : PARC_4 > 4, \end{cases} \tag{1.4}$$

and

$$PARC_k = \frac{\text{Area of bullae of size class } k}{\text{Area of lung}} \times 100. \tag{1.5}$$

$k = 1$, 2, 3 and 4, and $PARC_k$ equals the percentage of bullae of size class k. The bigger the size class, the larger the bullae size range. Definition about the size class is usually provided by radiologists based on the radiologist's experience and knowledge. The 2D bullae size classes proposed by Blechschmidt are: class 1: $d \leq$2.5mm, class 2: 2.5mm$< d \leq$5mm, class 3: 5mm$< d \leq$7.1mm, and class 4: $d >$ 7.1mm where d refers to the average diameter of bulla. BI ranges from zero to ten, corresponding to no emphysema bullae to many emphysema bullae in all size classes, respectively. BI applies higher weight for bigger sized bullae as shown in Eq. (1.1). The weights are manually determined based on a particular CT data set [6] and are fixed values.

By inferring mathematically from Eq. (1.1), the author noticed that the calculation of BI is susceptible to averaging effect. For instance, let us consider the following two cases:

1. A case with very high g_2 coupled with very low g_3 and g_4.

2. A case with very low g_2 coupled with low g_3 and/or low g_4.

The first case is likely to be diffuse emphysema which is less severe, even if the affected areas are large, compared to the second case which is probably characterized by slightly bullous emphysema. However, owing to averaging effect, it is possible that BI of the first case approximates that of the second case. As a result, BI is unable to discriminate the difference between these kinds of cases.

Besides BI, Blechschmidt [6] also introduced another emphysema describing index named emphysema type (ET). ET defines the relation of large emphysema bullae ($PARC_4$) to small emphysema bullae ($PARC_2$). It varies from -1 to +1, corresponding to nonbullous type to bullous type, respectively. The calculation of ET is shown as follow:

$$ET = \begin{cases} \dfrac{PARC_4 - PARC_2}{s} & : s > 1\%, \\ \text{not calculated} & : s \leq 1\%, \end{cases} \tag{1.6}$$

where

$$s = \sum_{i=2}^{4} PARC_i. \tag{1.7}$$

1.4.4 Texture-based methods

Texture-based approach using image classification with evolutionary programming invented by Uppaluri [23, 24] quantifies emphysema by detecting the radiographic texture in the lung CT. Texture-based methods include the Spatial Gray Level Dependence Matrix (SGLDM), Gray Level Gap Length Matrix (GLGLM), Gray Level Run Length Matrix (GLRLM) and Gray Level Difference Matrix (GLDM) [25, 26, 27, 28, 29, 30, 31]. Xu *et al* [11] proposed

multi-detector-CT-based 3D textures to classify the lung in the CT slice region-by-region using Adaptive Multiple Feature Method (AMFM). Texture-based methods coupled with evolutionary programming is a potential method for quantifying the radiographic patterns of emphysema. However, these methods are computationally costly. Moreover, it is very hard to find a generic texture feature subset for the quantification of emphysema [11, 32, 33]. This is because a selected texture feature subset which is useful for the CT data set A might not be useful for the CT data set B. These drawbacks encourage researchers to devise features that are easier to interpret and correspond more closely to the particular radiographic patterns of emphysema. The theories and calculations of SGLDM, GLGLM, GLRLM and GLDM are illustrated in Appendix A.1.

1.4.5 Other approaches

Cederlund *et al* [34] devised a 2D-based method to indicate the heterogeneity of lung. The method plotted the graph of emphysema index for 10 CT slices taken from the upper to the lower lobe of the lung with 20mm of separation between each slice and the slope of the best-fit line for the graph was proposed to be an indicator of the heterogeneity of the lung, such as heterogeneous emphysema with upper lobe predominance, heterogeneous emphysema with lower lobe predominance, intermediately heterogeneous emphysema and homogeneous emphysema [34, 35]. Besides, measurement of airway dimensions for assessing emphysema severity is reported in [36, 37, 38, 39].

Chapter 2

The Proposed System and Pre-Processing

2.1 The proposed computer aided diagnostic system

The ultimate goal of this research is to produce a more informative diagnosis of emphysema by devising new emphysema describing features. In order to achieve the goal, three methods are invented. The methods are encompassed in the proposed computer aided diagnostic system as shown in Fig. 2.1. The system allows user to assess both regional and total emphysema severity in the lung. Besides, it also analyzes the distribution of emphysema severity from the top to the bottom of the lung in a sub-volumetric-classification framework. In addition, visual aids in both two and three dimensions are provided to assist radiologists to verify their diagnoses. The system is also equipped with algorithms for navigating CT slices in different planes and identifying emphysema severity in the CT slice based on different colors.

Radiologists recognize the following features when performing a manual CT-based diagnosis of emphysema:

1. The different regional radiographic emphysema patterns in the lung CT [40].

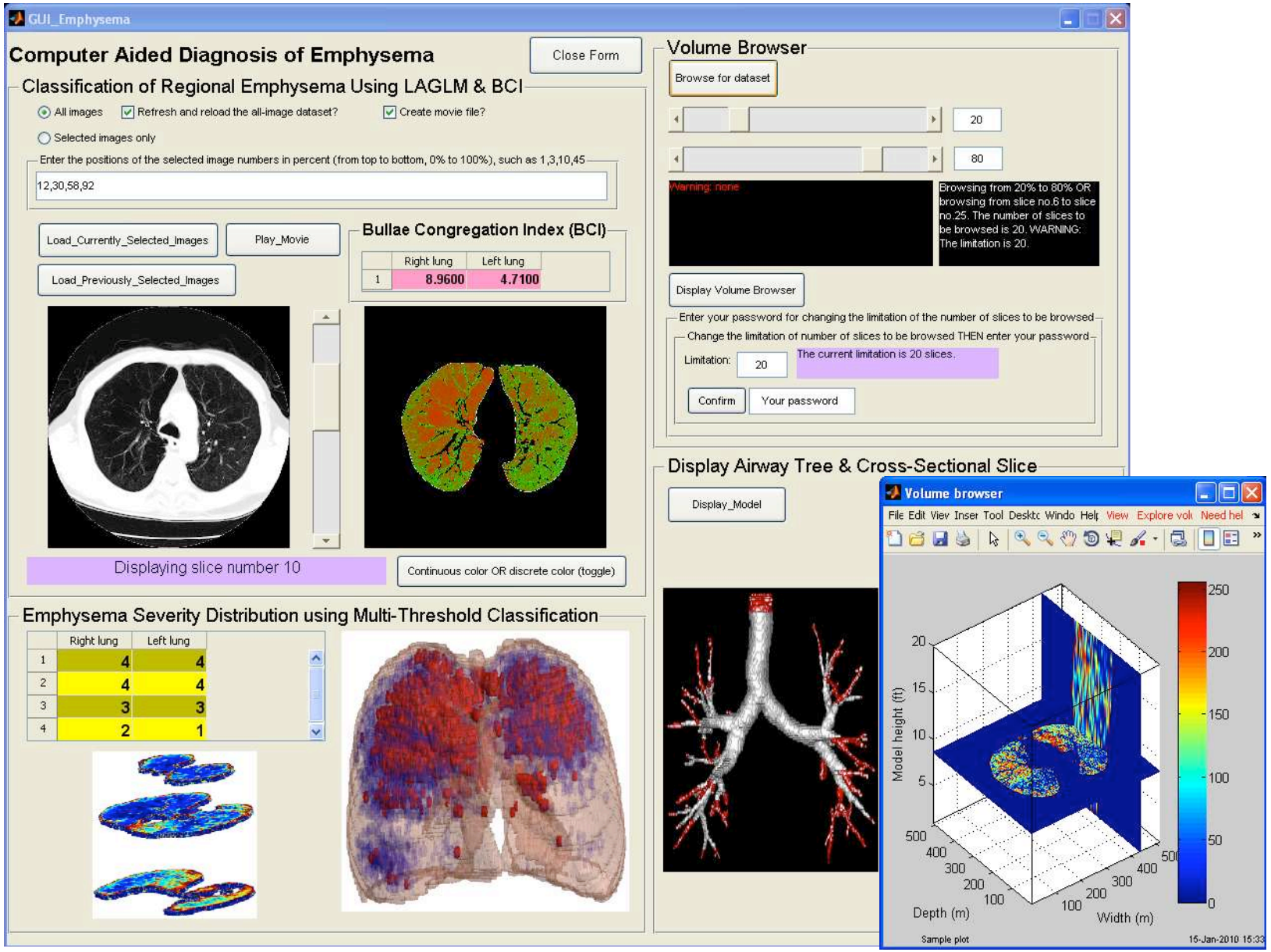

Fig. 2.1: The graphical user interface of the computer aided diagnosis of emphysema produced in this research.

2. The sizes of bullae.

3. The 2D and 3D distribution of bullae in the lung [41, 42].

In this dissertation, the author proposes three efficient methods to create new emphysema describing features:

1. The multi-threshold method and visualization of emphysema (see the lower left of Fig. 2.1).

2. The Low Attenuation Gap Length Matrix (LAGLM) (see the upper left of Fig. 2.1).

3. The bullae congregation index (BCI) (see the upper left of Fig. 2.1).

All three methods share the same final goal which is to further describe and/or quantify emphysema to assist medical experts to realize more objective, thorough and informative diagnosis of emphysema. The proposed methods can be used in follow-up study for progressive monitoring [43, 44] of emphysema. All algorithms in this research are written in Matlab.

2.2 Experiment data

The CT data sets of 41 subjects (29 males and 12 females) are used for the purpose of this research. The number of CT images in each data set ranges from 80 to 258. The age and height of the subjects are 67 ± 13 years and 164.50 ± 8.87cm, respectively. All the CT images are captured from the transverse plane of human thorax using a General Electric Multi-slice CT scanner. The images are provided by the Division of Pulmonary Medicine, Department of Medicine, Keio University, Japan. The images are stored in digital image and communications in medicine (DICOM) format and made anonymous beforehand. The images are 16 bits in depth. The size of the images is 512×512 pixels. The thickness of the CT slices ranges from 1mm to 7mm but most of the images are 1mm thick. The pixel size of the images varies between and including 0.5918×0.5918mm^2 and 0.7410×0.7410mm^2. All

the proposed algorithms in this dissertation are implemented based on the original signed 16-bit images.

2.3 Pre-processing

Pre-processing is applied to all three of the proposed methods to identify lung region(s) in 2D slices. The original DICOM images used in this research are signed 16 bits in depth. The lung region(s) can hardly be seen in the original image as shown in Fig. 2.2(a).

To identify the lung region(s) in a 2D slice, the author first linearly converts the original image to unsigned 8-bit representation. Pixel intensities from –1000 HU to 0 HU in the original image are linearly converted to the range between and including 0 to 255. The range of pixel intensities from -1000 HU to 0 HU is chosen because it includes all important information of the substances in the lung like air, fat and water (see Table 1.1. Pixel intensities below –1000 HU and above 0 HU are converted to 0 and 255, respectively. The image after the linear conversion is shown in Fig. 2.2(b).

From Fig. 2.2(b), the author can visually divide the image into three different parts: the dark borders, the bright mass that surrounds the lung regions and the lung regions. In many images, the bright mass in the middle of the image cuts the dark border into two parts (upper part and lower part) such as the image in Fig. 2.2(b). In order to make sure that the upper border and the lower border of the image are connected, the author expands the left border and the right border of the image by 10 pixels and pad the expanded areas with gray level of zero [see Fig. 2.2(c)]. The purpose of doing this is to facilitate the process of labeling [27] in the next step. After border expansion, the author computes the complement[†] of the image. Then the author binarizes [45] the image using a threshold of 100 and finally label [27] the image. The labeled image is shown in Fig. 2.2(d). Each white region in the labeled

[†]In the complement of an intensity image, each pixel value is subtracted from the maximum pixel value supported by the class (such as 255 for unsigned 8-bit images) and the difference is used as the pixel value in the output image.

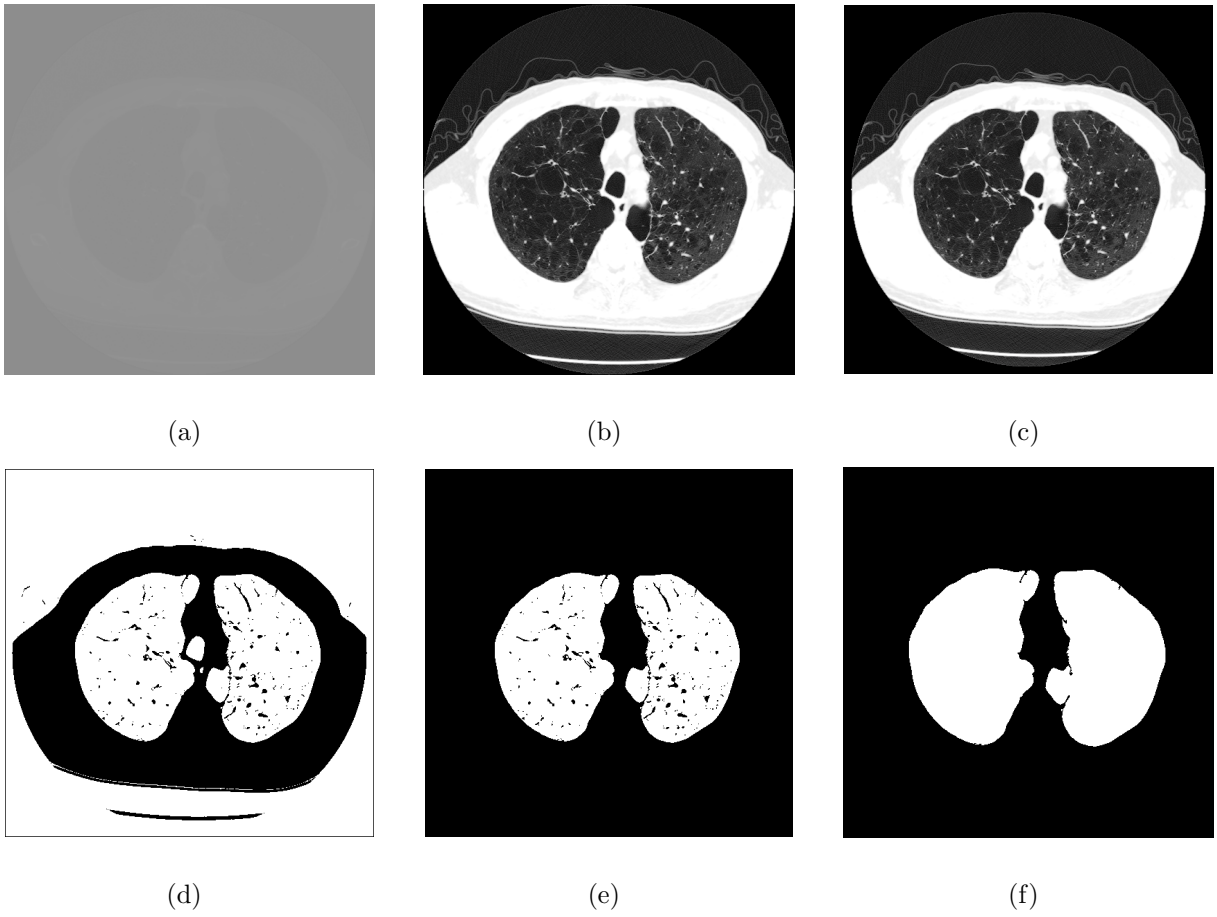

(a) (b) (c)

(d) (e) (f)

Fig. 2.2: The procedure for lung region(s) identification: (a) original image, (b) image after linear conversion of intensity, (c) image after border expansion, (d) image after intensity complementation and binarization, (e) identified lung regions (before filling holes), and (f) identified lung regions (after filling holes).

image is regarded as a labeled region.

From the labeled image, the biggest labeled region is the border of the image. The area of the image border is consistently at least twice larger than the lung region. This phenomenon was verified using 200 randomly selected images from five subjects. If the area of the third biggest labeled region is more than 20% of the area of the second biggest labeled region, then the right lung region and the left lung region in the image are considered as separated. Consequently, the union of the second and the third biggest labeled regions represents the lung regions. Otherwise, the right lung region and the left lung region are considered as being joined together where the second biggest labeled region represents the lung region. The identified lung regions are shown in Fig. 2.2(e). Finally, the author fills [27] the dark holes that are located within the lung regions. The final identified lung regions are shown in Fig. 2.2(f). The accuracy of the lung region(s) identification procedure was successfully verified using 2000 randomly selected transverse-plane images from 31 subjects.

Note that emphysema is represented by the air-filled regions in the lung. Since the HU of air in CT is close to the lower end of the scale which is –1000 HU (see Table 1.1), therefore emphysema appears as LAAs in the CT. The gray level threshold for extracting the LAAs from CT ranges from –900 HU to –1000 HU [6, 11, 23, 24, 33, 46].

Chapter 3

Methodology 1: Multi-threshold method

3.1 Background

The two significant factors that radiologists are considering when diagnosing emphysema include local emphysema severity and emphysema distribution. To take into account these two factors, the proposed method incorporates two notions: 1) multi thresholds, and 2) sub-volumetric classification of the lung. By combining these two notions, the author managed to meet the goal of the study which is to produce a more practical and effective emphysema-quantification algorithm that correlates with the PFT's parameters better than the classical methods.

Emphysematous regions correspond to the regions in the lung where airway wall collapse. When airway wall collapse, air-filled regions are formed. X-ray attenuation for air is low (see Table 1.1 for the Hounsfied Unit of air). Thus, the air-filled regions appear as low-attenuation areas (LAAs) in CT images (see Fig. 1.3). In short, emphysema is represented by LAAs with pixel intensity towards the lower end of the Hounsfield Unit scale which is –1000 HU. The use of the thresholds between –900 HU and –990 HU for extracting LAAs from CT

Table 3.1: Correlation between PIs and the PFT's parameters based on the CT data set A that consists of 15 subjects.

method	PFT's parameters			
	$FEV_1\%$		FEV_1/FVC	
	correlation coefficient	p-value	correlation coefficient	p-value
PI_{-900HU}	0.3854	< 0.05	0.6392	< 0.01
PI_{-910HU}	0.4128	< 0.05	0.6750	< 0.01
PI_{-920HU}	0.4345	< 0.01	0.6965	< 0.01
PI_{-930HU}	0.4483	< 0.01	0.7002	< 0.01
PI_{-940HU}	0.4530	< 0.01	0.6866	< 0.01
PI_{-950HU}	0.4521	< 0.01	0.6628	< 0.01
PI_{-960HU}	0.4492	< 0.01	0.6364	< 0.01
PI_{-970HU}	0.4444	< 0.01	0.6108	< 0.01
PI_{-980HU}	0.4356	< 0.01	0.5867	< 0.01
PI_{-990HU}	0.4057	< 0.01	0.5451	< 0.01

Table 3.2: Correlation between PIs and the PFT's parameters based on the CT data set B that consists of 15 subjects.

method	PFT's parameters			
	$FEV_1\%$		FEV_1/FVC	
	correlation coefficient	p-value	correlation coefficient	p-value
PI_{-900HU}	0.5036	< 0.01	0.7638	< 0.01
PI_{-910HU}	0.5288	< 0.01	0.7729	< 0.01
PI_{-920HU}	0.5452	< 0.01	0.7655	< 0.01
PI_{-930HU}	0.5484	< 0.01	0.7423	< 0.01
PI_{-940HU}	0.5505	< 0.01	0.7105	< 0.01
PI_{-950HU}	0.5515	< 0.01	0.6771	< 0.01
PI_{-960HU}	0.5569	< 0.01	0.6447	< 0.01
PI_{-970HU}	0.5467	< 0.01	0.6141	< 0.01
PI_{-980HU}	0.5316	< 0.01	0.5851	< 0.01
PI_{-990HU}	0.5081	< 0.01	0.5532	< 0.01

images has been reported in many studies [6, 11, 23, 24, 33, 46]. However, the optimal or generic threshold remains unknown. For this reason, the author initially hypothesized that there was an optimal threshold for extracting LAAs. To verify the hypothesis, the author collected two different CT data sets: the CT data set A and B. The CT data set A and B consist of 15 subjects, respectively. The author carried out a series of correlation analyses between PIs (see Section 1.4.1 for the theory of PI) that were calculated using different thresholds and the PFT's parameters (see Appendix A.4 for the explanation on the PFT's parameters). The correlation analyses results in Table 3.1 and 3.2 were computed based on the CT data set A and B, respectively. From the correlation coefficients of PIs versus $FEV_1\%$, the optimal PI for the CT data set A is $PI_{-940\text{HU}}$ while the optimal PI for the CT data set B is $PI_{-960\text{HU}}$. From the correlation coefficients of PIs versus FEV_1/FVC, the optimal PI for the CT data A is $PI_{-930\text{HU}}$ while the optimal PI for the CT data set B is $PI_{-910\text{HU}}$. In other words, a particular threshold, for instance, $PI_{-940\text{HU}}$, which is optimal for the CT data set A might not be optimal for the CT data set B. Based on this observation, the author concludes that it is unlikely or extremely difficult to find the optimal or generic threshold for extracting LAAs from CT images owing to the subtle radiographic variations.

The author hypothesizes that the entire threshold range from –900 HU and –990 HU contains important emphysema related information and therefore choosing just one threshold for quantifying emphysema is premature. Consequently, instead of finding a generic threshold, the author proposes a multi-threshold method to fully extract all essential emphysema related information from the entire spectrum of the lower threshold range (from –900 HU to –990 HU). Again, the author chooses this lower threshold range because emphysema is represented by air-filled regions in the lung and air-filled regions appear as LAAs in CT images. Therefore, the lower threshold range is more relevant to the definition of emphysema.

In order to facilitate a more insightful knowledge about the distribution of emphysema severity across the entire lung (from the top to the bottom of the lung) [10, 38, 37, 34], the author divides the lung into eight sub-volumes and classify the sub-volumes into four classes

of emphysema severity using neural network [47]. The author hypothesizes that different emphysema distributions might differently affect the overall functionality of the lung. Since the sub-volumetric classification results encompass both the information of local emphysema severity and the distribution of emphysema severity from the top to the bottom of the lung, the author accordingly hypothesizes that the proposed sub-volumetric classification results correlate with the PFT's parameters better than the classical methods. Besides, to help radiologists verify their diagnoses pertaining to the distribution of emphysematous destruction [48] in the patient's lung, the author proposes a transparent lung model that allows users to visualize the distribution [49, 50, 51] of emphysema in the lung in three dimensions.

3.2 Implementation of the multi-threshold method

The implementation of the proposed multi-threshold method is organized into three parts:

1. Color-coding processing.
2. Visualization of emphysema.
3. Sub-volumetric classification of emphysema using neural network.

3.2.1 Color-coding processing

Ten gray-level thresholds that correspond to ten confidence levels of emphysematous destruction are determined as shown in Table 3.3 [52]. The author supposes that the lower the gray level, the higher the confidence level of emphysematous destruction becomes. The author color-codes the lung based on the color-coding rules in Table 3.3. This idea is originally inspired by the notion of LAA owing to its effectiveness in detecting emphysematous radiographic patterns in the CT image. The color-coding processing consists of the following steps:

Table 3.3: Color-coding rules.

Gray-level range (HU), α	Color (emphysematous destruction)
$\alpha \leq$–990	Red (level-10 severity)
$\alpha \leq$–980	Blue (level-9 severity)
$\alpha \leq$–970	Yellow (level-8 severity)
$\alpha \leq$–960	Cyan (level-7 severity)
$\alpha \leq$–950	Green (level-6 severity)
$\alpha \leq$–940	Magenta (level-5 severity)
$\alpha \leq$–930	Biege (level-4 severity)
$\alpha \leq$–920	Dark green (level-3 severity)
$\alpha \leq$–910	Purple (level-2 severity)
$\alpha \leq$–900	Gray (level-1 severity)

1. From the pre-processed image, extract the pixels that correspond to the gray level range of a particular color code (see Table 3.3).
2. Binarize the image by highlighting only the extracted pixels.
3. Filter the image with a 3×3 median filter to eliminate small noise.
4. Dilate the image with a disk-shaped structuring element of the size of two pixels in radius.
5. Color-code the highlighted pixels.
6. Repeat step one to five for all other color codes listed in Table 3.3.
7. Overlap all ten colors in the image in such a manner that if two or more colors overlap, priority will be given to the color that correspond to the lower or lowest gray-level range.

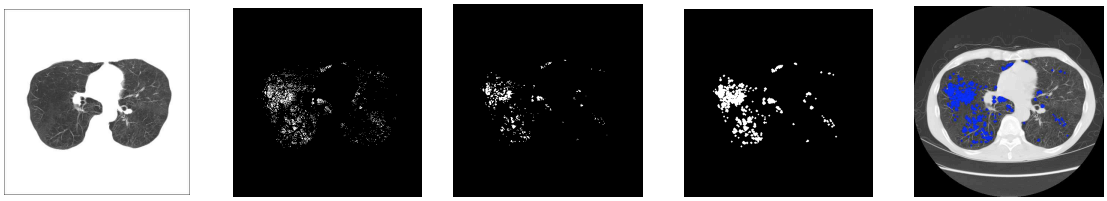

(a) (b) (c) (d) (e)

Fig. 3.1: Color-coding processing from (a) to (e) for an individual color: (a) pre-processed image, (b) image after direct extraction of pixels that correspond to the gray level range of blue (binarized iamge), (c) image after 3×3 median filtering, (d) image after dilation, and (e) the individually color-coded image.

Fig. 3.1 shows an example of the flow of color-coding processing for the individual color of blue. Fig. 3.2 shows the ten individually color-coded images. The product of the color-coding processing is the multi-color-coded image as shown in Fig. 3.3(b).

By using the proposed color-coding processing, the author is able to extract the lung areas that correspond to the potential emphysematous areas seen in the original CT image. In a preliminary assessment, the author requested radiologists to visually compare 30 multi-color-coded images with their original CT images. The extracted color-coded areas are in good agreement with both the visually perceivable and fuzzy emphysematous areas in the CT images not only in terms of locations but also sizes and shapes as shown in the comparison between Fig. 3.3(a) and Fig. 3.3(b). From the multi-color-coded image, the author accordingly computed the 2D gray-coded image as shown in Fig. 3.3(c) where the darker area corresponds to lower gray-level range. The author stacks up the 2D gray-coded images to build the 3D volume data for implementing the 3D visualization of emphysema.

3.2.2 Visualization of emphysema

Four 3D lung visualization techniques are implemented in this research:

1. 3D contour slices of the lung.

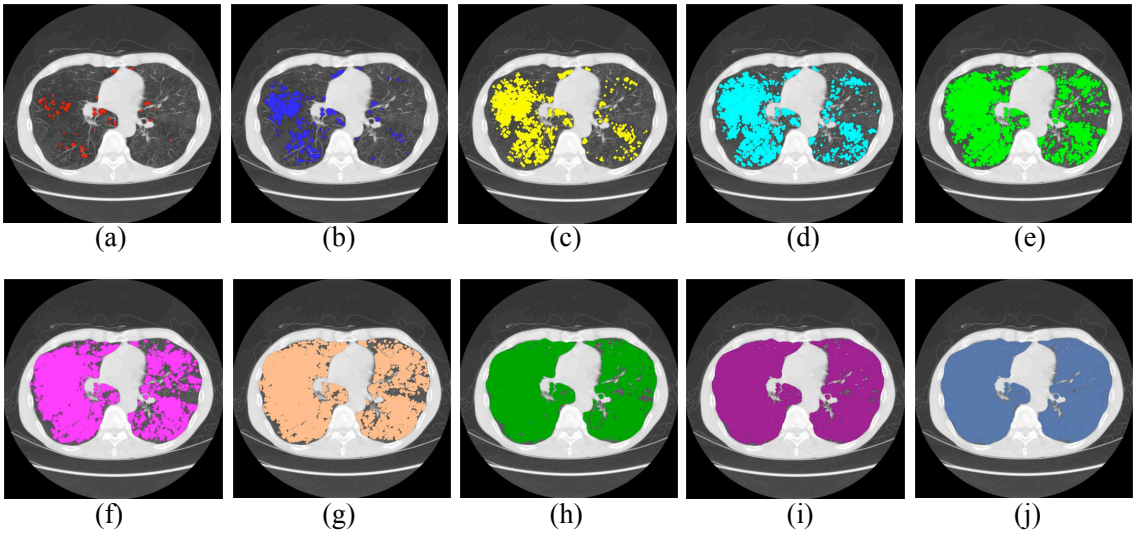

Fig. 3.2: Individually color-coded images: (a) red-coded image (≤–990 HU), (b) blue-coded image (≤–980 HU), (c) yellow-coded image (≤–970 HU), (d) cyan-coded image (≤–960 HU), (e) green-coded image (≤–950 HU), (f) magenta-coded image (≤–940 HU), (g) biege-coded image (≤–930 HU), (h) dark-green-coded image (≤–920 HU), (i) purple-coded image (≤–910 HU), and (j) gray-coded image (≤–900 HU).

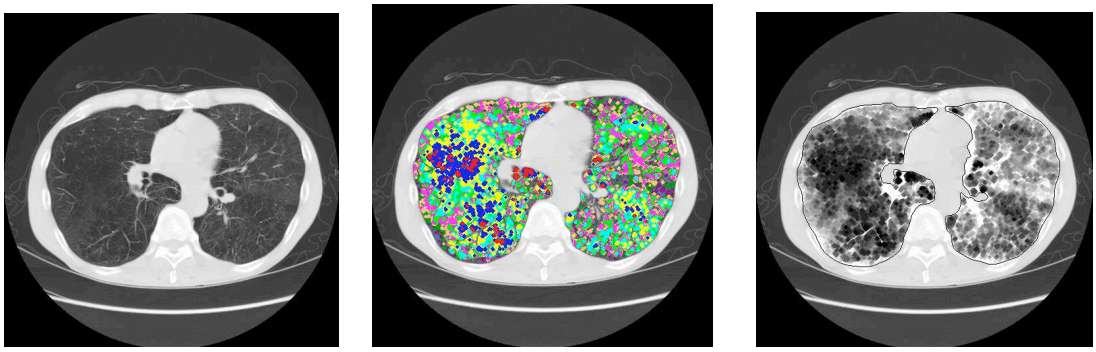

Fig. 3.3: Comparison between the original image and the multi-color-coded image: (a) image before color-coding processing (original image), (b) image after color-coding processing (multi-color-coded image), and (c) the 2D gray-coded image.

2. 3D solid lung model.

3. 3D sliced-away lung model.

4. 3D transparent lung model.

All 3D lung models in this research are programmed using Matlab graphics [53, 54] and OpenGL [55]. 3D visualization techniques such as isosurfaces and patches [53] and Gouraud lighting [53, 55] are utilized. Isosurface [56] is used to returns triangle vertices in a manner similar to Delaunay triangulation [53] which plots the triangles. Isocaps are used to create the faces on the outer surfaces of the lung volume [53]. A patch graphics object is composed of one or more polygons that may or may not be connected [54]. Patches [55] are useful for modeling real-world objects and for drawing 3D polygons of arbitrary shape. Isonormals modifies properties of the drawn patches so that lighting works correctly [53]. Although the volume data can be visualized quite clearly, the realism of the scene can be enhanced or diminished by creating different lighting effects. In this research, the Gouraud lighting [53, 55] was employed to enhance the user's ability to visualize the volume data being analyzed.

The four proposed 3D lung models are shown in Fig. 3.4. The 3D contour slices of the lung are computed from the patient's 18^{th}, 60^{th} and 129^{th} CT slice. On the other hand, the 3D solid lung model is computed using 150 CT slices. The 3D sliced-away lung model is generated by slicing the lung model at the 85^{th} slice. The transparent lung model is produced by first generating the transparent surface of the lung then overlapping the model with the red- and blue-coded voxels where the blue-coded voxels are programmed to be slightly transparent for a better overall visual display. The red and blue volumes in the interior of the transparent lung model correspond to the level-10 and level-9 emphysematous destruction, respectively, in the lung. Note that PFT-based class [class 1 (normal) to 5 (very severe)] is the diagnosis made based on the post-bronchodilator spirometry test where spirometry test is one of PFTs (see Appendix A.4). All of the generated 3D lung models can be viewed from any orientation.

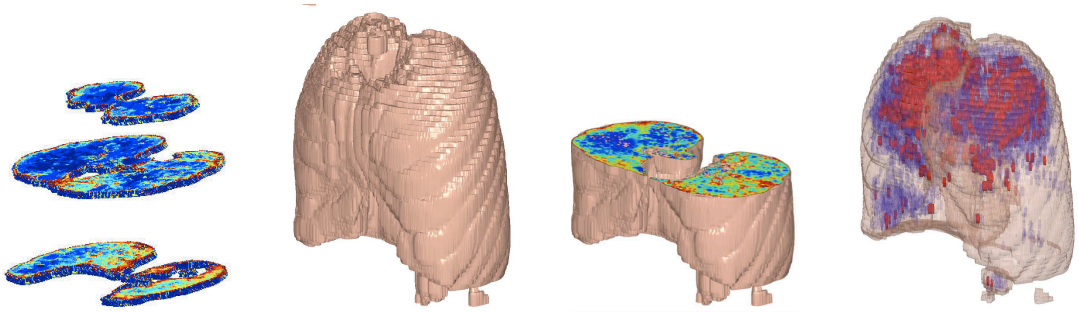

(a) (b) (c) (d)

Fig. 3.4: The 3D visualization techniques employed in this study: (a) the 3D contour slices of lung, (b) the 3D solid lung model, (c) the sliced-away lung model, and (d) the 3D transparent lung model (PFT-based class of class 4).

The proposed 3D transparent lung model is generated using all the available images in the patient's CT data set. The model is intended to be used to assist radiologists in realizing the distribution of emphysematous destruction across the entire lung in a more comprehensive, effective and time-efficient manner.

3.2.3 Sub-volumetric classification of emphysema using neural network

Assuming that the transparent lung model is fitted tightly in a cube, the author divides the 3D transparent lung model into eight sub-volumes by first halving the cube in the coronal plane and consequently quartering the cube in the transverse plane. Then, the author calculates the ratios of voxels that correspond to the ten different color codes in each sub-volume. The divided 3D lung is shown in Fig. 3.5 where the locations of the eight sub-volumes are described in Table 3.4. The author extracts ten features from each sub-volume. The extracted features are illustrated in Table 3.5. Subsequently, the features are pumped into the input layer of a neural network. The author chooses to use neural network as the classifier after comparing its performance with other classifiers like k-nearest neighbor

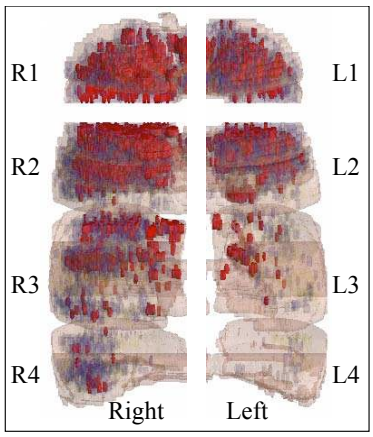

Fig. 3.5: The 3D transparent lung model after being divided into eight sub-volumes.

Table 3.4: Locations of the sub-volumes.

Sub-volume	Abbreviation	Location of the sub-volume
sub-volume 1	R1	top right
sub-volume 2	L1	top left
sub-volume 3	R2	upper-middle right
sub-volume 4	L2	upper middle left
sub-volume 5	R3	lower-middle right
sub-volume 6	L3	lower-middle left
sub-volume 7	R4	bottom right
sub-volume 8	L4	bottom left

Table 3.5: Sub-volumetric features.

Sub-volumetric feature, $feat$	Description of feature
$feat(1)$	ratio of red voxels in the sub-volume
$feat(2)$	ratio of blue voxels in the sub-volume
$feat(3)$	ratio of yellow voxels in the sub-volume
$feat(4)$	ratio of cyan voxels in the sub-volume
$feat(5)$	ratio of green voxels in the sub-volume
$feat(6)$	ratio of magenta voxels in the sub-volume
$feat(7)$	ratio of biege voxels in the sub-volume
$feat(8)$	ratio of dark-green voxels in the sub-volume
$feat(9)$	ratio of purple voxels in the sub-volume
$feat(10)$	ratio of gray voxels in the sub-volume

algorithm, support vector machine and discriminant analysis. The comparisons are included in Section 3.3.2.

Neural network topology

The author implements a multilayer perceptron neural network as the classifier [57] (see Appendix A.3 for the detailed explanation bearing on the implementation of a multi-class neural network) for classifying the sub-volumes of the lung into four classes of emphysema severity. The neural network consists of ten input nodes in the input layer to receive the ten sub-volumetric features and four output nodes in the output layer that correspond to the four classes of sub-volumetric emphysema severity. One hidden layer is implemented in the

neural network because the author desires a neural network that is capable of approximating any function that contains a continuous mapping from one finite space to another (see Table A.1 in Appendix A.3.2 for the theory in determining the number of hidden layers [58, 59]). There are many rule-of-thumb methods [59] for determining the correct number of neuron to use in the hidden layer to avoid the problems of overfitting and underfitting [59]. In this research, the number of neurons in the hidden layer is determined as the rounded value of $(2n/3+m)$ [59], respectively (see Table A.2 in Appendix A.3.2 for the rationale in determining the number of neurons in the hidden layer [59]) where n is the number of input nodes in the input layer and m is the number of output nodes in the output layer. Since the number of input nodes, n, and the number of output nodes, m, are ten and four, respectively, the number of neurons in the hidden layer equals to 11.

Neural network training

The author adopts the back-propagation learning algorithm [58] for the neural network training. In this study, a total of 80 sub-volumes of the lung obtained from ten subjects are used for neural network training. The author shall herefater refer these sub-volumes as the training sub-volumes. These training sub-volumes are manually consensus-classified into four classes of emphysema severity beforehand by radiologist based on the subjects' PFT results, visual recognition of the subjects' CT images and medical knowledge about emphysema. In order to ease the manual classification of the training sub-volumes, the author creates eight movie files per subject for the purpose of reference where each movie file shows the particular region in the CT images that correspond to the sub-volume of interest. The detailed explanation pertaining to the implementation of a multi-class neural network is written in Appendix A.3.

Stopping criteria

For stoping the neural network training, the author employs the automated stopping criteria inspired by the Steady-State Identification algorithm (SSID) [60] (see Appendix A.3.8 for the detailed explanation on the implementation of the SSID algorithm). After each epoch, about 25% of the data are randomly selected as the validation set for that epoch [60]. Therefore this method enables the use of 100% of the data for training. The trained neural network is used for classifying the sub-volumes of the lung into four emphysema severity classes. Since the logistic function is adopted as the activation function in the input nodes, neurons and output nodes (see Appendix A.3.5), the amplitude of the neural network output lies inside the range of $0 \leq output \leq 1$. The output node of the neural network that has the largest output value corresponds to the emphysema severity class of the sub-volume in which output node one to four correspond to emphysema severity class 1, 2, 3 and 4, respectively.

3.3 Results

For the visualization part, the author compared the implemented lung models with radiologists' hand annotations and confirmed that the models are in good agreement with radiologists' comments. The neural network is trained using 80 training sub-volumes of the lung obtained from ten subjects. The author validated the predictive performance of the trained neural network by classifying a total of 248 sub-volumes of the lung obtained from 31 subjects. The author shall hereafter refer these 248 sub-volumes as the test sub-volumes. The author compared the correlation between the proposed method and the PFT's parameters with those of the classical methods.

3.3.1 Visualization of emphysema

The implemented transparent lung models can be observed from any orientation as shown in Fig. 3.6. Figure 3.7 shows the transparent model of a mildly [61] emphysematous lung

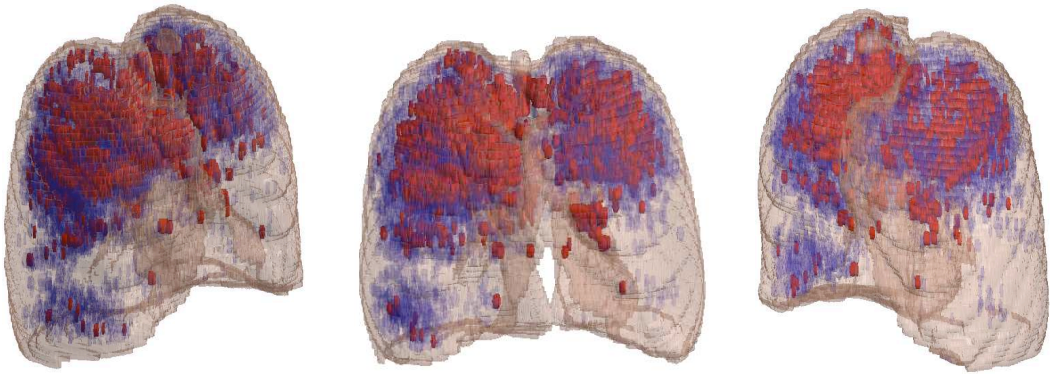

(a) (b) (c)

Fig. 3.6: 3-D emphysema-based transparent lung model viewed from: (a) azimuth angle = -45, elevation angle = 20, (b) azimuth angle = 0, elevation angle = 20 and (c) azimuth angle = 45, elevation angle = 20. The red and blue voxels in the image correspond to the volume below –990 HU and –980 HU, respectively.

(PFT-based class of class 2).

3.3.2 Four-class sub-volumetric classification results

The author classified the 248 test sub-volumes of the lung. The actual emphysema severity of the sub-volumes are consensus-classified by radiologist. The classification results are shown in Table 3.6. From Table 3.6, the four-class classification accuracy (average two-class classification accuracy) of the classifier is 89.82%. The author compares the classification accuracy of the neural network with those of other classifiers like the k-nearest neighbor algorithm, the support vector machine and discriminant analysis based on the 248 test sub-volumes of the lung. The two-class and four-class classification accuracies of the neural network, k-nearest neighbor algorithm, support vector machine and discriminant analysis are tabulated in Table 3.7. Although the performance of the support vector machine closely approximates that of the neural network, the author chose neural network as the classifier for this study.

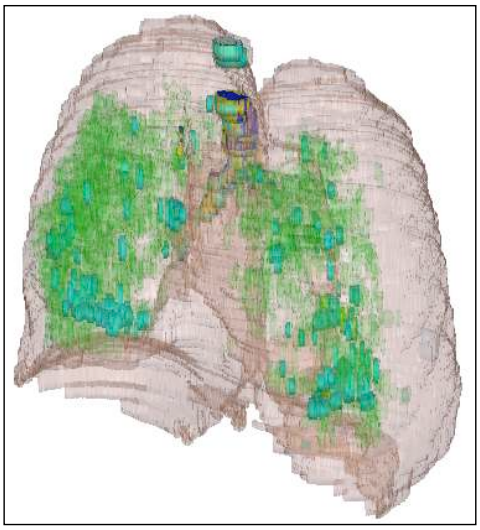

Fig. 3.7: An example of a mildly emphysematous lung (PFT-based class of class 2). The blue, yellow, cyan and green voxels in the image correspond to the volume below –980 HU, –970 HU, –960 HU and –950 HU, respectively.

Table 3.6: The contingency table of the four-class sub-volumetric classification of 248 test sub-volumes of the lung.

		Actual sub-volumetric class			
		1 (%) (case)	2 (%) (case)	3 (%) (case)	4 (%) (case)
Predicted sub-volumetric class	1 (%) (case)	95.00 (133)	5.00 (2)	0	0
	2 (%) (case)	5.00 (7)	85.00 (34)	3.57 (1)	0
	3 (%) (case)	0	10.00 (4)	89.29 (25)	10.00 (4)
	4 (%) (case)	0	0	7.14 (2)	90.00 (36)

Table 3.7: Comparisons of the classification accuracies of the neural network, k-nearest neighbor algorithm, support vector machine and discriminant analysis based on the 248 test sub-volumes of the lung.

	Classification accuracy (%) of the classifier			
	neural network	k-nearest neighbor algorithm	support vector machine	discriminant analysis
Class 1	95.00	94.29	79.29	93.57
Class 2	85.00	85.00	95.00	75.00
Class 3	89.29	89.29	89.29	85.71
Class 4	90.00	87.50	95.00	85.00
Four-class classification accuracy (%)	89.82	89.02	89.65	84.82

3.3.3 Correlation analyses

In order to validate how close the proposed sub-volumetric classification correlates with the subjects' PFT results, the author performed a series of correlation analyses between the sub-volumetric classification results and the PFT's parameters using multiple linear regression. The author also calculated the correlations between the classical methods and the PFT's parameters and compare them with that of the proposed method. The classical methods evaluated are the MLD, $PI_{-900\text{HU}}$, $PI_{-910\text{HU}}$, $PI_{-920\text{HU}}$, $PI_{-930\text{HU}}$, $PI_{-940\text{HU}}$, $PI_{-950\text{HU}}$, $PI_{-960\text{HU}}$, $PI_{-970\text{HU}}$, $PI_{-980\text{HU}}$, $PI_{-990\text{HU}}$, $BI_{-900\text{HU}}$, $BI_{-910\text{HU}}$, $BI_{-920\text{HU}}$, $BI_{-930\text{HU}}$, $BI_{-940\text{HU}}$, $BI_{-950\text{HU}}$, $BI_{-960\text{HU}}$, $BI_{-970\text{HU}}$, $BI_{-980\text{HU}}$, $BI_{-990\text{HU}}$, the entire-lung multi-threshold PIs and the entire-lung multi-threshold BIs. Note that the entire-lung multi-threshold PIs and BIs are comprised of ten PIs and BIs, respectively, calculated using the thresholds of –900 HU,

–910 HU, –920 HU, –930 HU, –940 HU, –950 HU, –960 HU, –970 HU, –980 HU and –990 HU.

Table 3.8 shows the four-class sub-volumetric classification results and the corresponding PFT-based classes (see Table A.4 in Appendix A.5 for the rules for determining the PFT-based class of a subject) of 15 sample subjects. The PFT's parameters, FEV_1/FVC and $FEV_1\%$ predicted (see Table A.3 in Appendix A.4) of the sample subjects are shown in Table A.5 in Appendix A.6. Table 3.9 shows the correlation coefficients and p-values of the proposed method and the classical methods, respectively, in correlation with the PFT's parameters (see Table A.3 in Appendix A.4) including $FEV_1\%$, $FEV_1\%$ and $DL_{co}VA$ [Diffusing capacity of the Lung for Carbon Monoxide (DL_{co}) divided by the Alveolar Volume (VA)]. Three conclusions are drawn from the results of the correlation analyses.

First conclusion drawn from the results of the correlation analyses

The author analyzed the correlation between the single-threshold PIs ($PI_{-900\text{HU}}$, $PI_{-910\text{HU}}$, $PI_{-920\text{HU}}$, $PI_{-930\text{HU}}$, $PI_{-940\text{HU}}$, $PI_{-950\text{HU}}$, $PI_{-960\text{HU}}$, $PI_{-970\text{HU}}$, $PI_{-980\text{HU}}$ and $PI_{-990\text{HU}}$) with the PFT's parameters. The author finds that $PI_{-940\text{HU}}$ achieves generally the highest correlation with the PFT's parameters compared to those of the other PIs. The author implemented the same analysis on BI. The author finds that $BI_{-950\text{HU}}$ achieves generally the highest correlation with the PFT's parameters compared to those of the other BIs. These findings suggest that the particular threshold value that yields the best correlation with the PFT's parameters for PI and BI is uncertain. Therefore, it is extremely difficult to find a generic threshold for the CT-based quantification of emphysema owing to the subtle variations of radiographic gray levels. Two of the PIs and BIs ($PI_{-940\text{HU}}$, $PI_{-950\text{HU}}$, $BI_{-930\text{HU}}$ and $BI_{-950\text{HU}}$) that achieve the highest correlation with the PFT's parameters are shown in Table 5.6.

Second conclusion drawn from the results of the correlation analyses

The author also analyzed the correlations between the entire-lung multi-threshold PIs and

Table 3.8: The four-class sub-volumetric classification and the corresponding PFT-based class of 15 sample subjects.

Subject	Sub-volumetric classification								PFT-based class
	R1	L1	R2	L2	R3	L3	R4	L4	
1	4	4	4	4	4	4	3	3	5
2	4	4	4	4	3	3	3	3	5
3	4	4	4	4	4	4	4	4	5
4	4	4	4	4	2	2	2	2	4
5	2	1	4	4	4	4	2	2	4
6	1	1	3	3	4	4	3	4	4
7	4	3	3	4	2	3	2	2	3
8	1	1	3	3	4	4	2	2	3
9	2	3	2	3	2	2	2	2	2
10	1	1	1	2	1	2	1	1	2
11	1	2	1	2	2	2	1	1	2
12	1	1	1	1	1	1	1	1	1
13	1	1	2	1	1	1	1	1	1
14	1	1	1	1	1	1	1	1	1
15	1	1	1	1	1	1	1	1	1

Table 3.9: Correlation of the proposed method, PI, BI, and MLD with the PFT's parameters based on the sub-volumetric classification results of 31 subjects.

method	PFT's parameters							
	$FEV_1\%$		FEV_1/FVC		$DL_{co}VA$		PFT-based class	
	correlation coefficient	p-value	correlation coefficient	p-value	correlation coefficient	p-value	correlation coefficient	p-value
MLD	0.4344	< 0.05	0.5716	< 0.01	0.7380	< 0.01	0.3382	< 0.1
$PI_{-940\text{HU}}$	0.5785	< 0.01	0.7725	< 0.01	0.6646	< 0.01	0.5350	< 0.01
$PI_{-950\text{HU}}$	0.5936	< 0.01	0.7505	< 0.01	0.6444	< 0.01	0.5124	< 0.01
$BI_{-930\text{HU}}$	0.2023	< 0.5	0.3094	< 0.1	0.5168	< 0.01	0.2518	< 0.2
$BI_{-950\text{HU}}$	0.4415	< 0.02	0.5585	< 0.01	0.7515	< 0.01	0.4058	< 0.05
Entire-lung multi -threshold PIs	0.6814	< 0.01	0.8264	< 0.01	0.8505	< 0.01	0.6435	< 0.01
Entire-lung multi -threshold BIs	0.5002	< 0.05	0.6933	< 0.01	0.8167	< 0.01	0.5246	< 0.05
proposed method (sub-volumetric classification results)	0.7748	< 0.01	0.8827	< 0.01	0.7835	< 0.01	0.7223	< 0.01

the parameters of PFT, and between the entire-lung multi-threshold BIs and the parameters of PFT. The entire-lung multi-threshold PIs and BIs from Table 5.6 are calculated based on ten thresholds: –900 HU, –910 HU, –920 HU, –930 HU, –940 HU, –950 HU, –960 HU, –970 HU, –980 HU and –990 HU. The correlation performance of the entire-lung multi-threshold PIs is higher than those of the single-threshold PIs ($PI_{-940\text{HU}}$ and $PI_{-950\text{HU}}$) while the correlation performance of the entire-lung multi-threshold BIs is generally higher than those of the single-threshold BIs ($BI_{-930\text{HU}}$ and $BI_{-950\text{HU}}$). These suggest that multi-threshold methods are more effective for quantifying emphysema compared to the classical single-threshold methods.

Third conclusion drawn from the results of the correlation analyses

Finally, the author correlated the proposed sub-volumetric classification results with the PFT's parameters. From the results in Table 5.6, the proposed method achieves higher correlation with the PFT's parameters compared to the classical single-threshold methods ($PI_{-940\text{HU}}$, $PI_{-950\text{HU}}$, $BI_{-930\text{HU}}$ and $BI_{-950\text{HU}}$). This is within our expectation because the proposed method is a multi-threshold-based method and therefore its performance is better than the single-threshold methods. On the other hand, the proposed method also achieves higher correlation compared to the entire-lung multi-threshold PIs and BIs. Note that the entire-lung multi-threshold PIs and BIs do not include the information of emphysema distribution. In comparison, the proposed sub-volumetric classification results encompass both the information of emphysema severity and the distribution of emphysema severity across the entire lung. The author hypothesizes that besides emphysema severity, the distribution of emphysema severity also plays an important role in diagnosing emphysema. The author confirms his hypothesis based on the results of the correlation analyses in Table 5.6 in which the proposed method performs better than the entire-lung multi-threshold PIs and BIs in correlation with the PFT's parameters.

3.4 Discussion

Three subjects were avoided in this study due to the significant discrepancy between the subjects' CT-based visual recognition and PFT results. The volume thresholds used in the calculation of BI are: class 0: $\geq$2mm^3, class 1: $\geq$8mm^3, class 2: $\geq$65mm^3, and class 3: $\geq$120mm^3 [62].

The best tests for determining the presence of emphysema and managing its response to treatment are PFTs. The gold standard test is spirometry. Spirometry test measures the amount (volume) and/or speed (flow) of air that can be inhaled and exhaled [9]. However, the maneuver of spirometry test is highly dependent on patient's cooperation and effort, and is normally repeated at least three times to ensure reproducibility. Since spirometry test results are dependent on patient's cooperation, the test values such as FEV_1 and FVC, can only be underestimated, never overestimated. Hence, review of both the PFT's parameters and CT images by radiologist is necessary for accurate diagnosis of emphysema. In this study, the emphysema severities of both the sub-volumes of lung and entire lung are consensus-classified beforehand by radiologist from Keio University Hospital, Japan. In order to ease the process of manual classification, the author collects all images from the patient's data set and create movie files that show the region in the CT images that correspond to the particular sub-volume of interest. The movie files are used by radiologists as references when performing manual classification of emphysema.

Based on the author's experience, thresholds like -910 HU and -915 HU, for example, usually result in just slight difference in the ratio of thresholded areas in the CT image. Thus the author tries not to use thresholds that are too close to each other to prevent from generating irrelevant features. Consequently, the ten thresholds utilized in this paper are between and including -900 HU to -990HU with an interval of 10 HU.

Chapter 4

Methodology 2: Low Attenuation Gap Length Matrix

4.1 Background

Features generated from the former texture-based methods like GLGLM, GLRLM, SGLDM and GLDM [11, 23, 24, 25, 63, 64, 65, 66] are not expressive for describing emphysema because the underlying rationales in these methods are not significantly related to the definition of emphysema. Emphysema is defined as the low-attenuation areas in the CT. A continuous low-attenuation area is called a bulla [6] or an LAA [14, 15].

Methodology 2 is created following the confirmation from the results of Methodology 1 that the use of multi-threshold method is more efficient than the classical single-threshold method for the quantification of emphysema. To illustrate why the former texture-methods are not efficient for describing emphysema, the author cuts out a region from the lung area of a CT. The region is shown in Fig. 4.1. Then, the author analyzes the pixel intensity profile of the highlighted horizontal line in the region as shown in Fig. 4.2. The pixel intensity from pixel number 20 to 30 along the highlighted horizontal line is tabulated in Table 4.1. The corresponding schematic diagram representing the change of pixel intensity

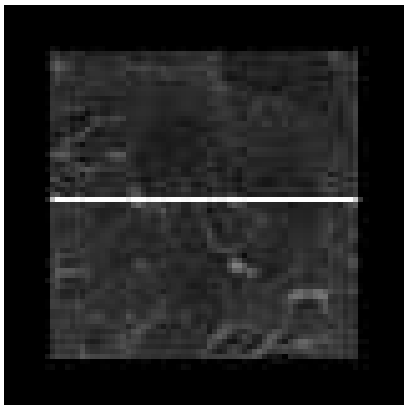

Fig. 4.1: The pixel intensity profile of the highlighted horizontal line in the region.

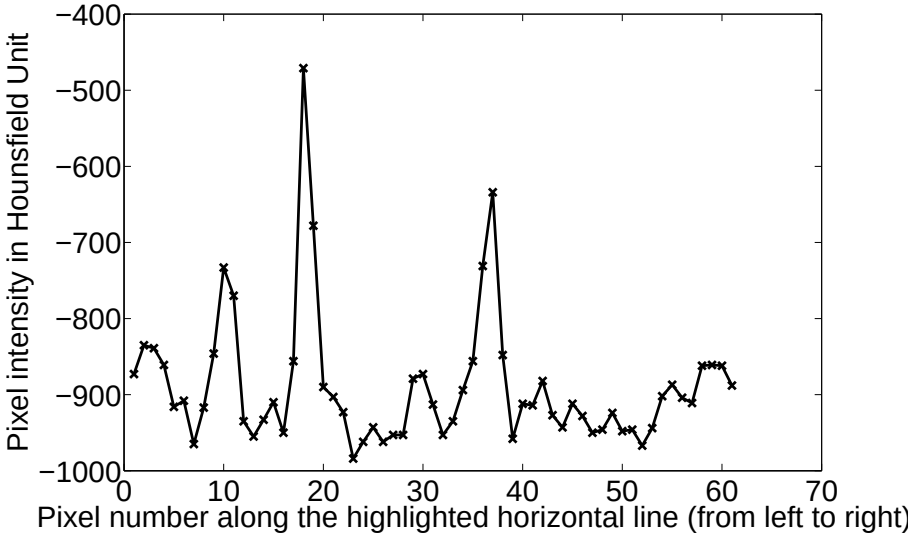

Fig. 4.2: The pixel intensity profile of the highlighted horizontal line in the region.

Table 4.1: Pixel intensity from pixel number 20 to 30 along the highlighted horizontal line in the region.

Pixel number	20	21	22	23	24	25	26	27	28	29	30
Hounsfield Unit	–890	–903	–923	–984	–962	–943	–962	–953	–953	–879	–873

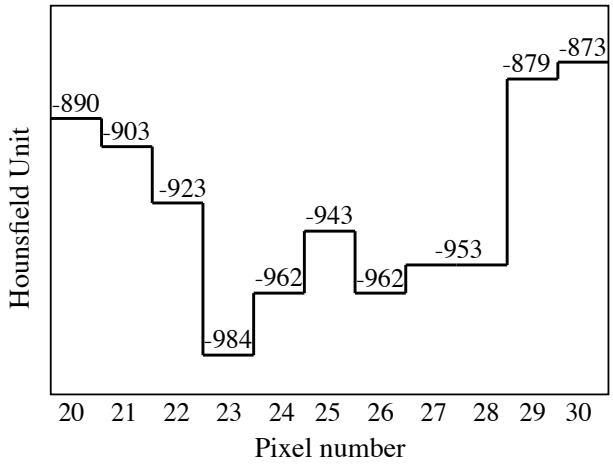

Fig. 4.3: Schematic diagram of the pixel intensity from pixel number 20 to 30 along the highlighted horizontal line.

from pixel number 20 to 30 is shown in Fig. 4.3. Please note that to analyze emphysema, the continuous colinearly adjacent pixels with gray level below a certain threshold should be taken into account. From Fig. 4.4(a), GLGLM calculates the gap length between two pixels with the same gray level [25, 67]; GLRLM calculates the run length of colinearly adjacent pixels with the same gray level [25, 68, 69]; SGLDM calculates the probability of going from a certain gray level to the other gray level [25, 67, 70]; GLDM calculates the gray level difference between two pixels given a certain inter-sample spacing [25, 67]. The underlying rationales in all the above mentioned former texture-based methods are not sufficiently significant for measuring emphysema. Therefore, the texture features generated

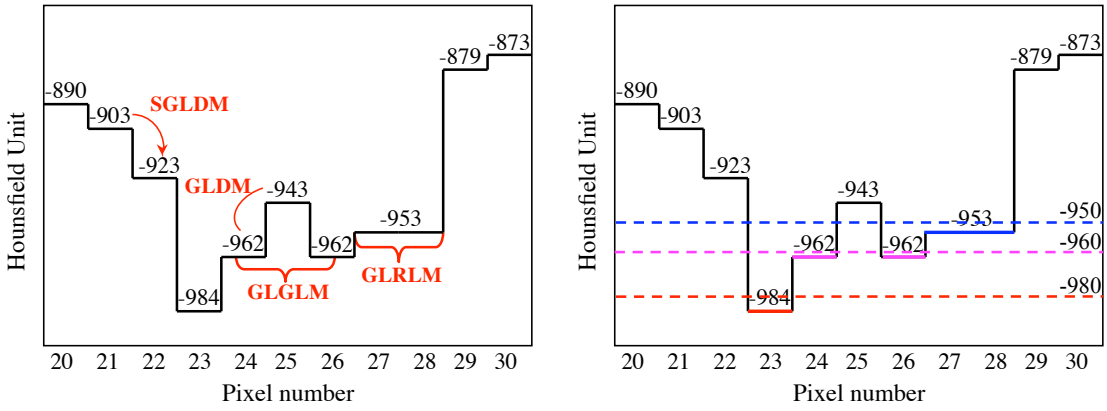

Fig. 4.4: (a) Explanation on GLGLM, GLRLM, SGLDM and GLDM using the schematic diagram. (b) Explanation on LAGLM using the schematic diagram.

from these methods are difficult to interpret and use when it comes to diagnosing emphysema. It is hard to know which feature is useful and which is not. Accordingly, when using these former texture-based methods for measuring emphysema, feature subset selection is always required as a pre-processing step to machine learning for reducing dimensionality, eliminating irrelevant data and improving classifier performance [32]. However, the generic usefulness of the selected texture feature subset is often dependent on the CT data set in use. For instance, a selected texture feature subset which is useful for the CT data set A might not be useful for the CT data set B. CT images are often varying and subtle. Thus, it is very hard to find a generic texture feature subset [71] based on the former texture-based methods for the quantification of emphysema [11, 32, 33]. As a result, the author proposes a method called Low Attenuation Gap Length Matrix (LAGLM) that takes into account the varying gap lengths of the continuous colinearly adjacent pixels withe gray level below a certain threshold. For instance, from Fig. 4.4(b), there is one short gap length (highlighted as red line) below the threshold of –980 HU; there is an addition of two short gap lengths (highlighted as magenta lines) if the threshold is increased to –960 HU; and there is an addition of one longer gap length (highlighted as blue line) if the threshold is further increased to –950

HU. Following the confirmation from the results of Methodology 1 that the use of multi-threshold method is more efficient than the classical single-threshold method for quantifying emphysema, the author uses multiple thresholds from –900 HU to –1000 HU in the LAGLM. The goal of the LAGLM is to produce texture features that are more relevant to the definition of emphysema, more generic, easier to interpret and easier to use for diagnosing emphysema. The author hypothesized that the features generated from the LAGLM are more efficient for quantifying regional emphysematous patterns [50, 72, 73] as compared to the features generated from the former texture-based methods. Please note that detailed explanations on the former texture-based methods are written in Appendix A.1.

4.2 Implementation of the LAGLM

When analyzing a lung CT, radiologists visually divide the radiographic lung tissues presented in the CT into a few emphysema types before concluding the overall emphysema severity of the lung. Consequently, the author proposes to use the features generated from the LAGLM to discriminate four different regional emphysematous patterns. Neural network is employed as the classifier. The characteristics of four regional emphysema patterns/types, namely, N, DE, BEDE and BE, are defined as follows:

1. N (Normal) — visually smooth lung tissues without apparent bullae.

2. DE (Diffuse Emphysema) — visually smooth lung tissues but with diffuse small-sized bullae [6, 61, 74].

3. BEDE (Bullous Emphysema and Diffuse Emphysema) — visually rough lung tissues that imply moderate destruction of airway walls or with medium-sized bullae (with or without concomitant small-sized bullae).

4. BE (Bullous Emphysema) — visually rough lung tissues that imply severe destruction of airway walls or with big-sized bullae [6, 74].

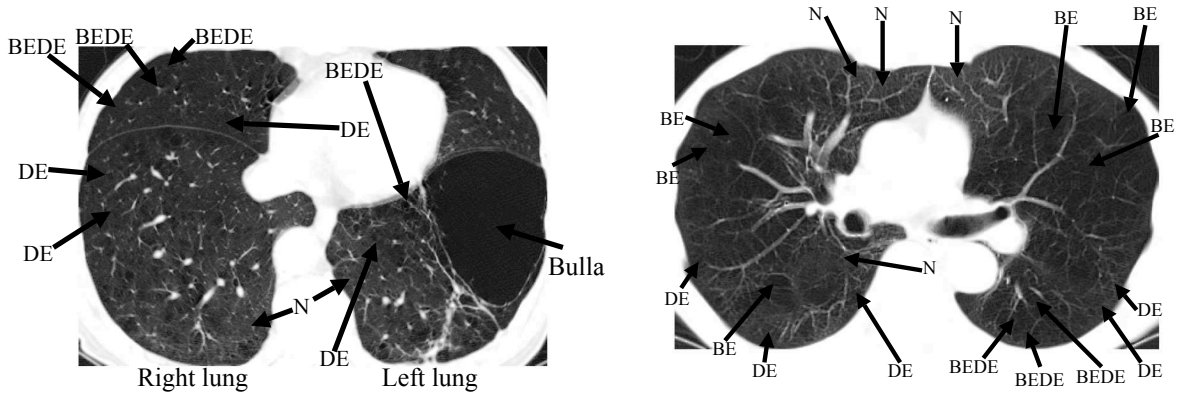

(a) (b)

Fig. 4.5: (a) An example of CT with an apparent big-sized bulla. (b) An example of CT where the radiographic patterns of emphysema are visually harder to recognize.

Figure 4.5(a) shows a typical thoracic CT with regions being labeled as N, DE, BEDE and BE. From the figure, the big-sized bulla in the left lung is visually easier to detect compared to the right lung that has less obvious emphysematous patterns. Having said that, compared to images that have apparent emphysematous pattern like the left lung in Fig. 4.5(a), most of the images used in this research have rather varied and subtle radiographic patterns which are visually harder to recognize like the CT in Fig. 4.5(b).

The flow of the implementation of the LAGLM is as follows:

1. Selection of 2D slices.

2. Region-by-region processing.

3. Regional feature calculation.

4. Classification of region using neural network.

4.2.1 Selection of 2D slices

For each patient, 10 images captured from the upper to the lower lung are retrieved for processing. A total of 27 subjects were evaluated. The selection of the 10 images is based on Eq. (4.1):

$$index(\beta) \quad = \quad \left(\frac{\beta}{10}\right) \times S, \tag{4.1}$$

where S is the sum of CT images in the patient's CT data set and $index(\beta)$ represents the index of the β^{th} selected image for integer $1 \leq \beta \leq 10$. $index(\beta)$ is rounded toward infinity. The author chooses 10 images as a result of trade-off between time of processing and comprehensiveness of processing data.

4.2.2 Region-by-region processing

After pre-processing, region-by-region processing was implemented. The main goal of the processing was to classify the selected regions in the image into four emphysema types: N, DE, BEDE and BE, which were corresponded by four different colors: green, blue, magenta and red, respectively.

The size of region under examination can be adjusted. The size of most 2D lung regions used in this research ranged approximately between 60-by-60 pixels to 200-by-300 pixels. Basically, the smaller the size of region under examination, the finer the classified regions appear in the classified image. However, the selected size of region can not be too small because if the size of region selected is as small as one diffuse emphysematous area, the region showing a small diffuse emphysema will look the same as the region showing a partial bullous emphysema and this makes the algorithm fail to discriminate between diffuse and bullous emphysema. The author examined 270 images and concluded that small diffuse emphysema consistenly appear in the size of smaller than 60-by-60 pixels. Thus, the author believes that the size of 60-by-60 pixels is generally appropriate for capturing both the emphysematous patterns of small diffuse emphysema and bullous emphysema without sacrificing the fineness

of classified regions in the classified image. Accordingly, the author decided to use the size of 60-by-60 pixels as the size of region under examination. For each image, the following steps are implemented.

1. Starting from the top left corner of the image, overlap an empty 60-by-60-pixel mask region on the image.

2. If more than 70% of the overlapped region comprises lung region, calculate regional features for the region, classify the emphysema type of the region using the trained neural network, paint the region with the color that corresponds to it's emphysema type, then slide the mask region by 10 pixels horizontally to the right. Otherwise, slide the mask region to the right by one pixel.

3. If the mask region spans beyond the horizontal limit of the image, slide it horizontally back to the leftmost position and then slide it vertically by 10 pixels down towards the bottom. If the mask region spans beyond the vertical limit of the image, then proceed to step 4. Otherwise, repeat step 2 and 3.

4. Calculate the area of green, blue, magenta and red regions in the image, respectively.

After gathering the area of green, blue, magenta and red regions for all 10 images, the author computes the percentage of area of each of the colors across the 10 images. The detailed algorithm of the region-by-region processing is described in Appendix A.2 where "{*/}" denotes side notes, p represents subject number, s represents image number, c represents color number from one to four corresponding to N- (green), DE- (blue), BEDE- (magenta) and BE-oriented (red) regions, respectively, TA represents the area of each color on each classified image for 27 subjects and MPA represents the percentage of total area of each color across 10 images for the 27 subjects.

4.2.3 Regional feature calculation

From the algorithm of region-by-region processing, regional feature calculation is implemented in step 24 (see Appendix A.2). In order to calculate the regional features, the algorithm scans a region from the first to the last row of pixels from the top to the bottom of the region and for each row of pixels, it scans from left to right pixel-by-pixel. The algorithm uses multiple thresholds between and including –1000 HU to –930 HU where pixels less than a particular threshold are considered as the low-attenuation pixels. Figure 4.6(a) and 4.6(b) show a highlighted horizontal line in sample region A and B, respectively. The highlighted horizontal line represents the row of pixels being scanned in the region. Figure 4.6(c) and 4.6(d) show the pixel profile for the highlighted row of pixels in region A and B, respectively. In this research, a gap is defined as some collinearly adjacent low-attenuation pixels where the gap length of a single low-attenuation pixel that has no collinearly adjacent low-attenuation pixels is one. For instance, the parts of the pixel profile in Fig. 4.6(d) that are below the lower horizontal line are the thresholded gaps for the case of threshold = –960 HU. There are a total of six thresholded gaps in this case where the gap length of the first gap is six pixels.

The detailed explanation bearing on the proposed regional feature calculations are described in the following. For illustration, Table 4.2(b) shows an example of the element of LAGLM, $r_{LAGLM}(t, g|\theta)$, based on a simple image [see Table 4.2(a)]. $r_{LAGLM}(t, g|\theta)$ specifies the estimated number of times a region contains a thresholded gap length g, for threshold t, in the direction of angle θ.

Emphysema in CT image is represented by low-attenuation areas. Therefore, to quantify regional emphysematous patterns, two key factors are considered: gray level distribution and low-attenuation ($\leq$ –930) gap lengths. Basically, the lower the gray level and the longer the low-attenuation gap length, the more extensive the severity of emphysema becomes. Standard texture methods like GLGLM and GLRLM are not adequately relatable to the descriptions of emphysema owing to their definitions. Therefore, the author proposes to use the

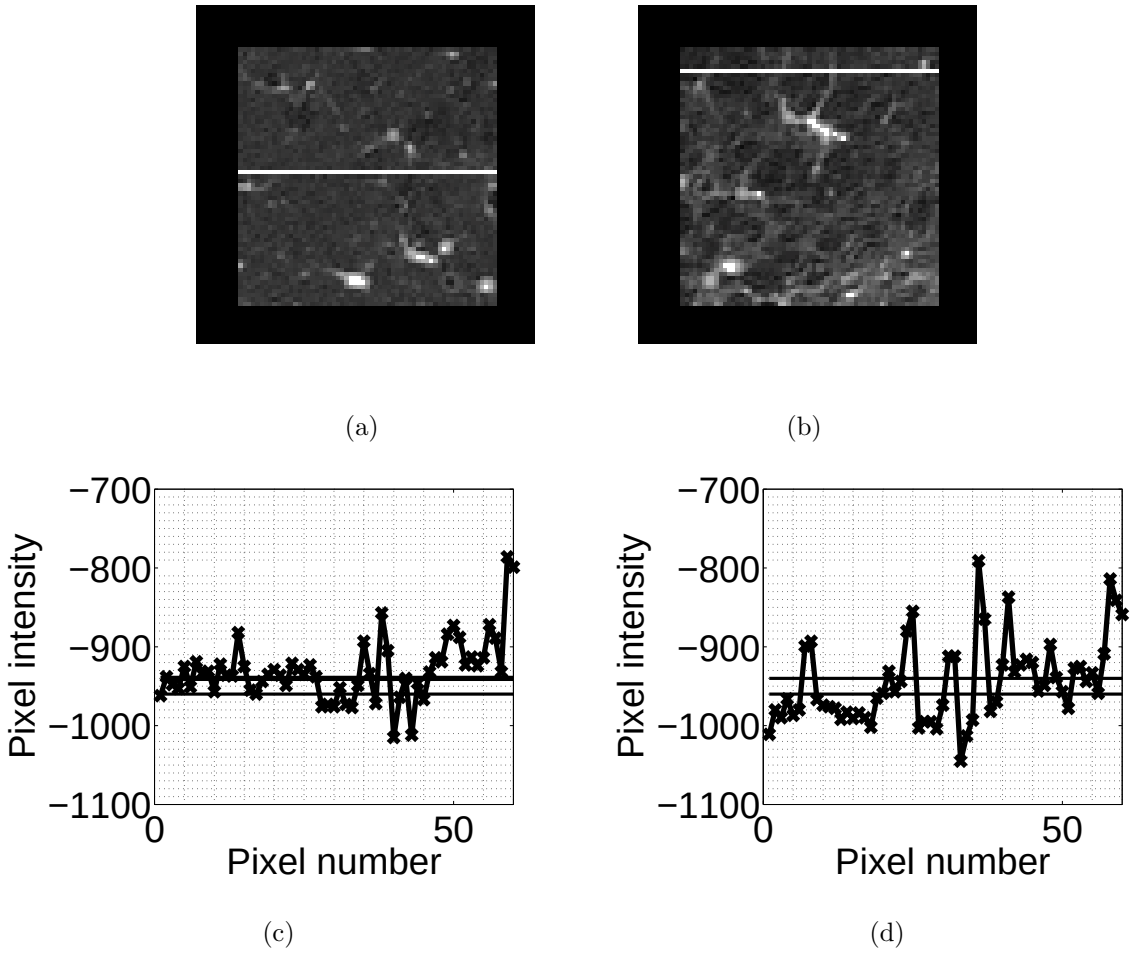

Fig. 4.6: Region profile: (a) region A with a particular row of pixels being highlighted, (b) region B with a particular row of pixels being highlighted, (c) pixel profile for the highlighted row of pixels in region A, and (d) pixel profile for the highlighted row of pixels in region B. The upper and lower horizontal lines in (c) and (d) represent the threshold levels of –940 HU and –960 HU, respectively.

Table 4.2: An example of LAGLM based on a simple image.

(a) a 4×10 simple image

–942	–920	–945	–960	–980	–941	–888	–896	–950	–960
–946	–962	–958	–974	–971	–963	–982	–991	–963	–963
–934	–950	–943	–962	–974	–967	–984	–994	–962	–963
–923	–941	–922	–962	–953	–943	–963	–951	–958	–943

(b) LAGLM: $r_{LAGLM}(t, g|\theta)$ for t =–1000,–990,...,–900

$\theta = 0°$		gap length, L									
		1	2	3	4	5	6	7	8	9	10
threshold,	–1000	0	0	0	0	0	0	0	0	0	0
t	–990	2	0	0	0	0	0	0	0	0	0
	–980	0	2	0	0	0	0	0	0	0	0
	–970	2	3	0	0	0	0	0	0	0	0
	–960	4	0	0	0	0	0	2	0	0	0
	–950	1	2	1	0	0	0	1	0	1	0
	–940	2	1	0	1	0	0	1	0	1	1
	–930	2	1	0	1	0	0	1	0	0	2
	–920	1	1	0	1	0	0	0	0	0	3
	–910	0	1	0	0	0	1	0	0	0	3
	–900	0	1	0	0	0	1	0	0	0	3

LAGLM for quantifying regional emphysematous patterns because features generated from the LAGLM collectively takes into account both gray level distribution (multiple gray level thresholds) and low-attenuation gap lengths. Features derived from LAGLM are expected to be able to reflect the degree of regional severity of emphysema.

For comparison purposes, two categories of features were derived from LAGLM. The first category of features were texture-based features which consisted of thresholded short gap emphasis ($TSGE$), thresholded long gap emphasis ($TLGE$), threshold distribution (TD), thresholded gap length distribution ($TGLD$), thresholded gap percentage (TGP), low threshold gap emphasis ($LTGE$) and high threshold gap emphasis ($HTGE$). The calculations of these features are shown in the following:

$$TSGE = \frac{1}{T_g} \sum_{t=-1000}^{-900} \sum_{g=1}^{IS} \frac{r_{LAGLM}(t,g|\theta)}{g^2}, \tag{4.2}$$

$$TLGE = \frac{1}{T_g} \sum_{t=-1000}^{-900} \sum_{g=1}^{IS} g^2 r_{LAGLM}(t,g|\theta), \tag{4.3}$$

$$TD = \frac{1}{T_g} \sum_{t=-1000}^{-900} \left[\sum_{g=1}^{IS} r_{LAGLM}(t,g|\theta) \right]^2, \tag{4.4}$$

$$TGLD = \frac{1}{T_g} \sum_{g=1}^{IS} \left[\sum_{t=-1000}^{-900} r_{LAGLM}(t,g|\theta) \right]^2, \tag{4.5}$$

$$TGP = \frac{1}{T_p} \sum_{t=-1000}^{-900} \sum_{g=1}^{IS} r_{LAGLM}(t,g|\theta), \tag{4.6}$$

$$LTGE = \frac{1}{T_g} \sum_{t=-1000}^{-900} \sum_{g=1}^{IS} t^2 r_{LAGLM}(t,g|\theta), \tag{4.7}$$

$$HTGE = \frac{1}{T_g} \sum_{t=-1000}^{-900} \sum_{g=1}^{IS} \frac{r_{LAGLM}(t,g|\theta)}{t^2}, \tag{4.8}$$

where IS is the maximum possible gap length in the region and

$$T_g = \sum_{t=-1000}^{-900} \sum_{g=1}^{IS} r_{LAGLM}(t,g|\theta), \tag{4.9}$$

where t =–1000,–995,–990,...,–900, and T_p is the number of points in the image. In this research, $T_p = 360$ because the size of region under examination is 60-by-60 pixels.

As compared to texture features generated from GLGLM and GLRLM, LAGLM-based texture features are more direct, more relevant and easier to interpret when it comes to describing radiographic emphysematous patterns. Thus, this makes the selection of optimal feature subset easier. For instance, $TSGE$ and $TLGE$ indicate the distribution of short and long low-attenuation gap lengths in the region, respectively. Higher $TSGE$ indicates less severe type of emphysema, usually diffuse and smaller-sized emphysema while higher $TLGE$ indicates more severe type of emphysema, usually bullous emphysema. $LTGE$ and $HTGE$ indicate how extensive the low-attenuation gap lengths are toward the lower end and upper end, respectively, of the range of gray-level threshold. Higher $LTGE$ indicates more severe emphysema owing to the more extensive low-attenuation areas toward the lower end of the range of gray-level threshold while higher $HTGE$ indicates milder emphysema owing to the low-attenuation areas toward the upper end of the range of gray-level threshold. From the seven texture features derived from LAGLM, the author selects $TLGE$, $LTGE$ and $HTGE$ as the features for the first category because the author hypothesizes that these features are more relevant to the descriptions of emphysema. The author shall hereafter refer these features as the LAGLM-based texture features.

The second category of features were directly derived from $r_{LAGLM}(t, g|\theta)$. The features consisted of the average frequency of gap lengths based on two thresholds and four gap length classes. For each row of pixels in a region, the algorithm identifies the low-attenuation gap lengths and divides the gap lengths into four gap length classes as shown in Table 4.3. After that, the algorithm calculates the average frequency of gap lengths across all rows of pixels within the region based on the gap length classes. For each region, the same calculation was executed from four principle directions: $\theta = 0°$, $45°$, $;0°$ and $135°$, and the average values across the four directions became the features for the region. Consequently, let $f(n, c|t, \theta)$ be the frequency of gap lengths that belong to gap length class c along the n^{th} row of pixels

Table 4.3: Gap length classes for the case of threshold equals –940 HU and –960 HU.

gap length class, c	range of gap length, L, for threshold = –940 HU	range of gap length, L, for threshold = –960 HU
1	$2 \leq L \leq 4$	$1 \leq L \leq 3$
2	$5 \leq L \leq 7$	$4 \leq L \leq 6$
3	$8 \leq L \leq 11$	$7 \leq L \leq 9$
4	$L > 11$	$L > 9$

in an image which has been rotated by an angle = θ given threshold = t, the author defines $M(c|t,\theta)$ as the average frequency of gap lengths across all rows of pixels that belong to gap length class c in an image which has been rotated by an angle = θ given threshold = t, for integers $1 \leq n \leq N$, $1 \leq c \leq 4$, t = –960 and –940, and $\theta = 0°$, $45°$, $90°$ and $135°$ where N is the sum of row of pixels in the rotated image. Pixels on the border of the rotated image that were not part of the image were ignored in the calculation. The calculation of $M(c|t,\theta)$ is shown in Eq. (4.10):

$$M(c|t,\theta) = \frac{1}{N}\sum_{n=1}^{N} f(n,c|t,\theta). \tag{4.10}$$

feature1 and ***feature2*** are row vectors containing the first and the second four regional features, respectively, as shown in Eq. (4.11) and (4.12):

$$feature1(c) = \frac{\sum_{\theta=0}^{135} M(c|\text{–}940,\theta)}{4}, \tag{4.11}$$

$$feature2(c) = \frac{\sum_{\theta=0}^{135} M(c|\text{–}960,\theta)}{4}. \tag{4.12}$$

Hence, a total of eight regional features were produced. These features were then directly fed into the neural network for classification. The author shall hereafter refer these features as the LAGLM-based two-threshold features.

The reason why the author separates gap lengths into multiple classes instead of just calculating the overall average gap length is to avoid the problem of averaging effect that originates from the difference between small gap lengths and large gap lengths. The range of threshold that reflects the existence of emphysema is from and including –1000 HU to –930 HU. The author defines the gap length classes based on the reasoning that generally, the lower the threshold, the smaller the low-attenuation gap length becomes. Therefore, the gap length classes defined for –960 HU is just slightly smaller than that of the case of –940 HU. Despite the small difference, the effects are significant. For instance, see the significant difference between the gap length distribution for threshold –960 HU and –940 HU in Table 4.2(b). The purpose of calculating the frequency of gap length in a row-by-row manner within a region from four different angles is to gather the small detail bearing on the radiographic emphysematous patterns along each row of pixels within the 60-by-60-pixel region meticulously.

The author proposes a two-threshold algorithm because the author has learned from Methdology 1 (see Table 3.1 and 3.2) that a threshold which is optimal for a particular CT data set might not be optimal for the other CT data sets. Therefore, the author employs two thresholds, –940 HU and –960 HU, for generating the second category of features. –940 HU and –960 HU are chosen because these thresholds are the optimal thresholds for CT data set A and B, respectively, in the author's experiment in the previous chapter (see Table 3.1 and 3.2).

4.2.4 Classification of region using neural network

From the algorithm of region-by-region processing, classification of region using neural network is implemented in step 25 (see Appendix A.2).

Neural network topology

The author adopted a four-class multilayer perceptron neural network [57] (see Appendix A.3 for the detailed explanation bearing on the implementation of a multi-class neural network) as the classifier for classifying the 60-by-60-pixel regions of lung into four emphysema types. The neural network consists of eight input nodes in the input layer to receive the eight regional features, and four output nodes in the output layer that correspond to the four regional emphysema types: N, DE, BEDE and BE, respectively. Based on trial and error, two hidden layers are implemented in the neural network. The underlying rationale for using two hidden layers is to produce a neural network that is capable of representing an arbitrary decision boundary to arbitrary accuracy with rational activation functions as illustrated in Table A.1 [58, 59]) in Appendix A.3.2. There are many rule-of-thumb methods [59] for determining the correct number of neurons to use in the hidden layer. The number of neurons in the hidden layer is determined as the rounded value of $(2n/3 + m)$ [59] (see Table A.2 in Appendix A.3.2 for the rationale in determining the number of neurons in the hidden layers [59]) where n is the number of input nodes in the input layer and m is the number of output nodes in the output layer. Since the number of input nodes, n, and the number of output nodes, m, is eight and four, respectively, the number of neurons in the two hidden layers equals to seven, respectively.

Neural network training

In this study, a total of 55 60-by-60-pixel regions, which had been consensus-classified into N, DE, BEDE, and BE by radiologists, were used as the training regions for neural network classification. The 55 training regions were gathered from a total of 40 images from the data sets of 4 subjects. Please refer to Appendix A.3 for the detailed implementation of neural network as a multi-class classifier. Figure 4.7 shows the training regions.

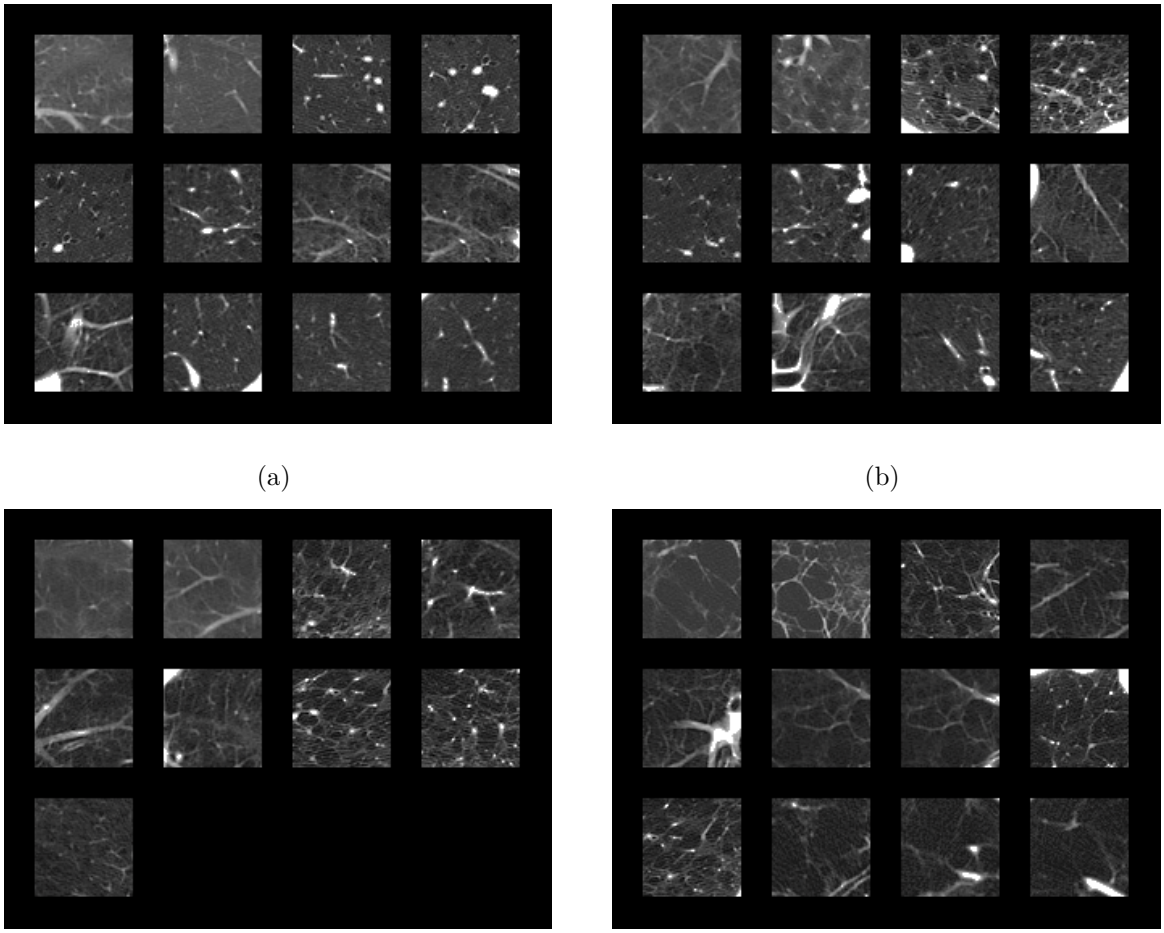

(a) (b)

(c) (d)

Fig. 4.7: The four emphysema types: (a) N-oriented training regions, (b) DE-oriented training regions, (c) BEDE-oriented training regions, and (d) BE-oriented training regions. All regions are 60-by-60 pixels in size.

Stopping criteria

The author employs automated stopping criteria inspired by the Steady-State Identification algorithm (SSID) [60] for stopping the neural network training (see Appendix A.3.8 for the detailed explanation on SSID). After each epoch, about 25% of the data are randomly selected as the validation set for that epoch [60]. Therefore this method enables the use of 100% of the data for training. The trained neural network is used for classifying the regions. Since the logistic function is adopted as the activation function in the input nodes, neurons and output nodes (see Appendix A.3.5), the amplitude of the neural network output lies inside the range of $0 \leq output \leq 1$. The output node of the neural network that has the largest output value corresponds to the emphysema type of the region in which output node one to four correspond to N, DE, BEDE and DE, respectively.

4.3 Results

In order to evaluate the LAGLM, the author first validated the 55 training regions of the lung using cross validation method. Again, the 55 training regions were gathered from a total of 40 images from the data sets of 4 subjects. Then, the author evaluated the predictive performance of the trained neural network by classifying 105 regions that were randomly selected from 270 images. The 270 images were obtained from the data sets of 27 subjects. The author shall hereafter refer these regions as the test regions. The 55 training regions were excluded from the 105 test regions. The author also showed some examples of the classified images produced by the algorithm along with their corresponding original images. To validate the correlation of the classification results to PFT-based results, the author carried out a series of correlation analyses.

Table 4.4: The contingency table of the cross-validation of 55 regions using LAGLM-based two-threshold features.

		Actual regional emphysema type			
		N (%) (case)	DE (%) (case)	BEDE (%) (case)	BE (%) (case)
Predicted regional emphysema type	N (%) (case)	93.75 (15)	0 (0)	0	0
	DE (%) (case)	6.25 (1)	92.31 (12)	11.11 (1)	0
	BEDE (%) (case)	0	7.69 (1)	88.89 (8)	0
	BE (%) (case)	0	0	0	100.00 (17)

4.3.1 Cross-validation of 55 regions

The author cross-validated 55 training regions to validate the effectiveness of the proposed regional features. All the regions for the cross-validation were visually consensus-classified into four classes of emphysematous severity by radiologists in advance. Table 4.4 and Table 4.5 are the contingency tables that show the cross-validation results of using LAGLM-based two-threshold features and LAGLM-based texture features, respectively. For comparison purpose, the author cross-validated the same regions by using: PI-based features, GLRLM-based features and GLGLM-based features. For PI-based features, the author used PI_{-940HU}, PI_{-950HU} and PI_{-960HU} as the regional features. For GLRLM-based features, the author used short run emphasis, long run emphasis, gray level distribution, run length distribution, run percentages, low gray level run emphasis and high gray level run emphasis as the regional features. For GLGLM-based features, the author used the features that are comparable to LAGLM-based texture features such as long gap emphasis, low gray level gap

Table 4.5: The contingency table of the cross-validation of 55 regions using LAGLM-based texture features.

		Actual regional emphysema type			
		N (%) (case)	DE (%) (case)	BEDE (%) (case)	BE (%) (case)
Predicted regional emphysema type	N (%) (case)	87.50 (14)	15.38 (2)	0	0
	DE (%) (case)	12.50 (2)	84.62 (11)	11.11 (1)	0
	BEDE (%) (case)	0	0 (0)	88.89 (8)	0
	BE (%) (case)	0	0	0	100.00 (17)

emphasis and high gray level gap emphasis, as the regional features.

The four-class cross-validation accuracies in the form of LAGLM-based two-threshold features /LAGLM-based texture features /PI /GLRLM /GLGLM were: N: 93.75% /87.50% /100% /62.50% /75.00%; DE: 92.31% /84.62% /84.62% /30.77% /23.08%; BEDE: 88.89% /88.89% /66.67% /55.56% /44.44%; and BE: 100% /100% /94.12% /76.47% /82.35%. The average four-class cross-validation accuracies in the form of LAGLM-based two-threshold features /LAGLM-based texture features /PI /GLRLM /GLGLM were: 93.74% /90.25% /86.35% /56.32% /56.22%. These results show that the proposed features, LAGLM-based two-threshold features and LAGLM-based texture features, are more expressive than the conventional methods in classifying regional radiographic emphysematous patterns into four classes especially in discriminating BEDE from DE and BE.

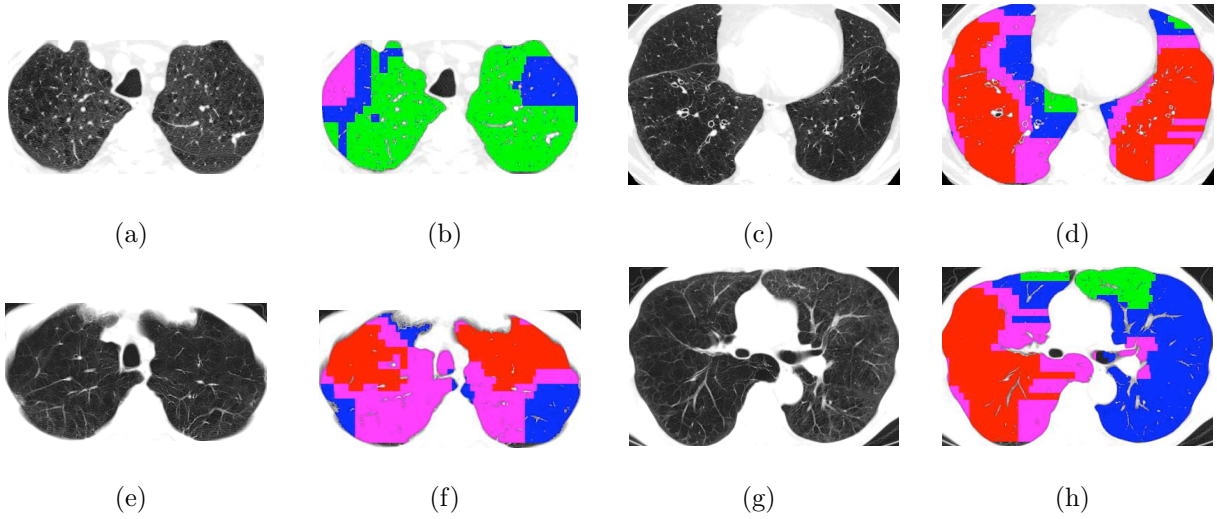

(a) (b) (c) (d)

(e) (f) (g) (h)

Fig. 4.8: Four examples of original and classified images: (a) original image no. 1 — little mildly bullous emphysema along with substantial normal lung tissue, (b) classified image no. 1, (c) original image no. 2 — the radiographic patterns suggest a severe destruction of airway walls, (d) classified image no. 2, (e) original image no. 3 — both severe and mild destruction of airway walls can be visually recognized, (f) classified image no. 3, (g) original image no. 4 — severe destruction of airway walls in the right lung and diffuse emphysema in the left lung and (h) classified image no. 4.

4.3.2 Classified images

The author trained the neural network using 55 training regions then by using the trained neural network, the author classified a total of 270 images from 27 subjects. Figure 4.8 shows four examples of classified images produced by using LAGLM-based two-threshold features. Green, blue, magenta and red regions correspond to N-, DE-, BEDE- and BE-oriented regions, respectively. The comments about the different radiographic emphysematous patterns in the original images in Fig. 4.8 were hand-annotated by radiologists. Figure 4.9 shows the comparison between original CT image with diseased areas annotated by radiologist and classified image produced by LAGLM-based two-threshold features and LAGLM-based texture features, respectively. By visual comparison, the author can see that the labeled dis-

eased areas in the original images correspond fairly to the classified regions in the classified images. Besides, the author can also see that there is a slight difference in classified regions between the classified images produced by LAGLM-based two-threshold features and the classified images produced by LAGLM-based texture features.

The author plotted the classification results, MPA, of five sample subjects which have significantly different emphysema severities in Fig. 4.10. From the figure, the author can relate the distribution of the percentage of different emphysematous lung tissues to the extent of the subject's emphysema severity. By looking at Fig. 4.10, there is an obvious increase in $MPA(:,4)$ from the case of severe to very severe emphysema and there is a general increase in $MPA(:,3)$ from normal to severe emphysema. This implies that $MPA(:,3)$ (BEDE-oriented lung tissues) and $MPA(:,4)$ (BE-oriented lung tissues) are significant indicators for the extent of the subjects' emphysema severity. Note that in Fig. 4.10, there are cases where the sum of MPA does not equal to 100% because some of the small edges of the lung in the images were not classified.

4.3.3 Classification of 105 test regions

In order to assess the accuracy of the classification results, the author randomly selected 105 regions from 270 images as the test regions and classified the regions. These regions had been carefully consensus-classified by radiologist in advance. The four-class classification accuracies of the 105 randomly selected regions in the form of LAGLM-based two-threshold features /LAGLM-based texture features /PI /GLRLM /GLGLM were: N: 92.31% /88.46% /96.15% /57.69% /61.54%; DE: 84.21% /78.95% /73.68% /31.58% /15.79%; BEDE: 85.71% /89.29% /71.43% /53.57% /50.00%; and BE: 93.75% /96.88% /90.62% /68.75% /78.12%. The average four-class classification accuracies in the form of LAGLM-based two-threshold features /LAGLM-based texture features /PI /GLRLM /GLGLM were: 89.00% /88.40% /82.97% /52.90% /51.36%. While LAGLM-based features apparently outperformed PI, GLRLM and GLGLM, the evaluation results also showed that LAGLM-based texture fea-

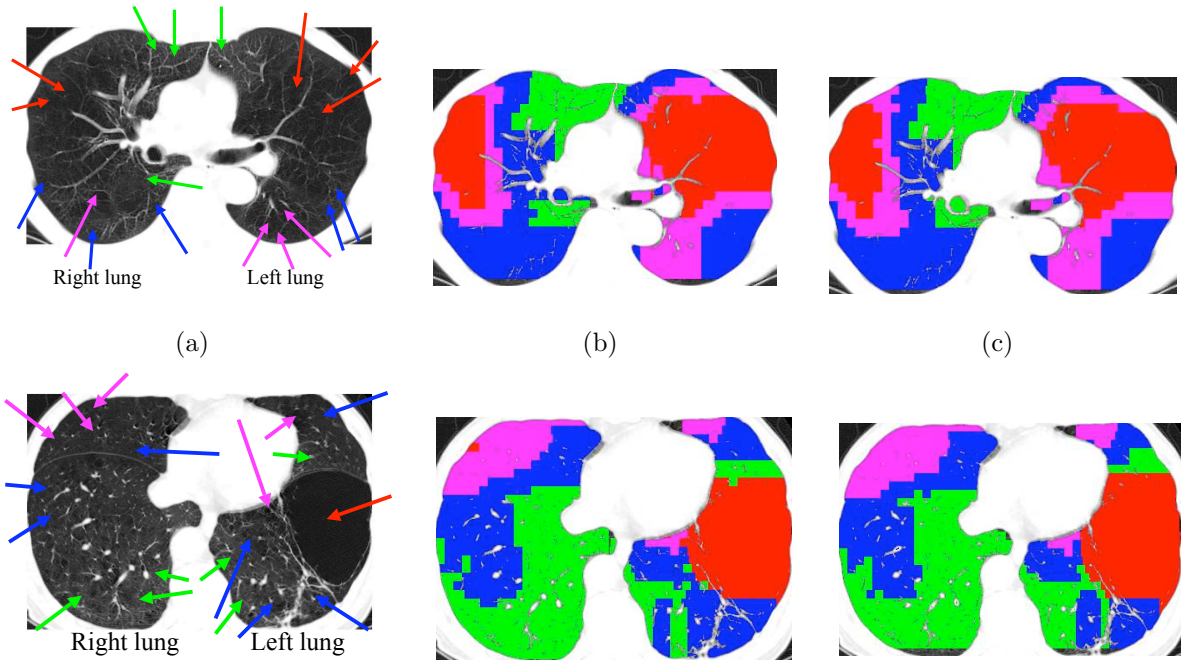

Fig. 4.9: A comparison between original image with diseased areas annotated by radiologist using colored arrows and the corresponding classified images produced by LAGLM-based two-threshold features and LAGLM-based texture features, respectively: (a) original image A — the radiographic patterns suggest moderate to severe destruction of airway walls along with diffuse emphysema where more destruction is observed in the left lung, (b) classified image A produced by LAGLM-based two-threshold features, (c) classified image A produced by LAGLM-based texture features, (d) original image B — obvious emphysematous bulla in the left lung and considerable concomitant diffuse emphysema in both the right and left lung, (e) classified image B produced by LAGLM-based two-threshold features and (f) classified image B produced by LAGLM-based texture features. The color green, blue, magenta and red correspond to N, DE, BEDE and BE, respectively.

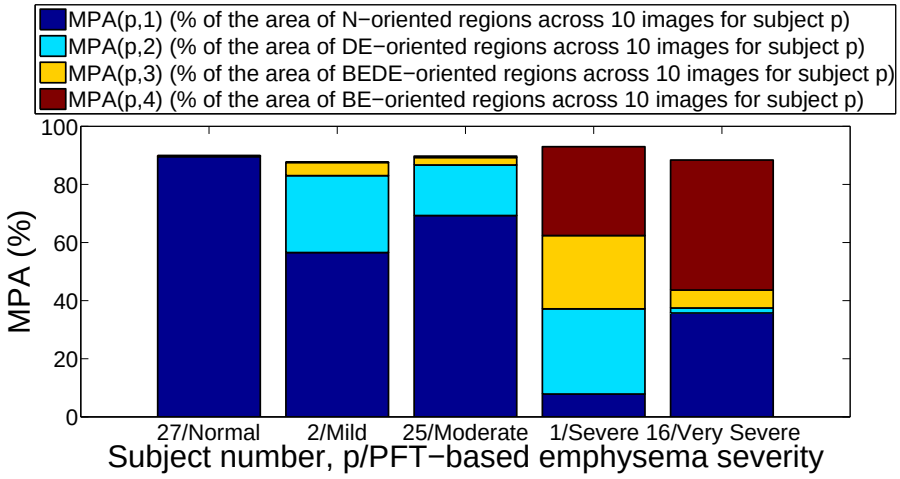

Fig. 4.10: The classification results of five sample subjects with significantly different emphysema severity.

tures are almost as effective as LAGLM-based two-threshold features for classifying regional emphysema into four classes as illustrated in Table 4.6 and Table 4.7.

4.3.4 Correlation analyses

For correlation analyses, the author focused on the classification results of 270 images produced by LAGLM-based two-threshold features and performed a series of correlation analyses between the classification results (MPA) and spirometry[‡] test results such as $FEV_1\%$ predicted [Forced Expiratory Volume in One Second (FEV_1) divided by Forced Vital Capacity (FVC)], FEV_1 (see Table A.3 in Appendix A.4) and PFT-based class (see Table A.4 in Appendix A.5). The correlation analyses were implemented using multiple linear regression. $FEV_1\%$ predicted and FEV_1 are usually used as the guidelines for determining the PFT-based class (severity) of subject (see Table A.4 [9] in Appendix B). The p-values of correlation of MPA to $FEV_1\%$ predicted, FEV_1 and PFT-based class, based on three different combinations of the percentage of classified regions: (1) BEDE and BE, (2) DE, BEDE and BE,

[‡]spirometry (meaning the measuring of breath) is the most common of the PFTs.

Table 4.6: The contingency table of the classification of 105 randomly selected regions from 270 images using LAGLM-based two-threshold features.

		Actual regional emphysema type			
		N (%) (case)	DE (%) (case)	BEDE (%) (case)	BE (%) (case)
Predicted emphysema type	N (%) (case)	92.31 (24)	5.26 (1)	0	0
	DE (%) (case)	7.69 (2)	84.21 (16)	14.29 (4)	0
	BEDE (%) (case)	0	10.53 (2)	85.71 (24)	6.25 (2)
	BE (%) (case)	0	0	0	93.75 (30)

Table 4.7: The contingency table of the classification of 105 randomly selected regions from 270 images using LAGLM-based texture features.

		Actual regional emphysema type			
		N (%) (case)	DE (%) (case)	BEDE (%) (case)	BE (%) (case)
Predicted regional emphysema type	N (%) (case)	88.46 (23)	5.26 (1)	0	0
	DE (%) (case)	11.54 (3)	78.95 (15)	7.14 (2)	0
	BEDE (%) (case)	0	15.79 (3)	89.29 (25)	3.12 (1)
	BE (%) (case)	0	0	3.57 (1)	96.88 (31)

Table 4.8: p-values of the correlation of $MPA(:, 3:4)$, $MPA(:, 2:4)$ and $MPA(:, 1:4)$ to $FEV_1\%$ predicted, FEV_1 and PFT-based class.

Classified regions (%)	$FEV_1\%$ predicted	FEV_1	PFT-based class
BEDE and BE $[MPA(:, 3:4)]$	$0.6374^{\ddagger}$	$0.5282^{\ddagger}$	$0.3746^{\ddagger}$
DE, BEDE and BE $[MPA(:, 2:4)]$	$0.6389^{\ddagger}$	$0.5415^{\ddagger}$	$0.3748^{\dagger}$
N, DE, BEDE and BE $[MPA(:, 1:4)]$	$0.6743^{\ddagger}$	$0.5524^{\ddagger}$	$0.3930^{\dagger}$

$^{\dagger}p < 0.05$

$^{\ddagger}p < 0.01$ (significant)

and (3) N, DE, BEDE and BE, were generally less than 0.01 as shown in Table 4.8. This implies that the region-by-region classification results correlated fairly well to PFT-based results.

4.4 Discussion

Former texture-based methods include GLGLM, GLRLM, SGLDM and GLDM (see Appendix A.1 for the detail of these methods). Among these methods, the two methods that are more similar to the proposed LAGLM are GLGLM and GLRLM. The following elaborate the differences that separate LAGLM from GLGLM and GLRLM.

GLGLM defines a gap as a peak or a valley between two pixels having the same gray level [63]. On the other hand, GLRLM defines a run length as some collinearly adjacent pixels having the same gray value [63, 25]. In this research, the proposed LAGLM defines a gap as some collinearly adjacent low-attenuation pixels where low-attenuation pixels refer to pixels

below a certain threshold. Therefore, LAGLM is different from GLRLM and GLGLM. Assume that $r_{GLGLM}(i, v|\theta)$ is a GLGLM [see Table 4.9(b)] that specifies the estimated number of times a region contains a gap length v, for gray level i, in the direction of angle θ, $r_{GLRLM}(i, j|\theta)$ is a GLRLM [see Table 4.9(c)] that specifies the estimated number of times a region contains a run length j, for gray level i, in the direction of angle θ, and $r_{LAGLM}(t, g|\theta)$ is an LAGLM [see Table 4.9(f)] that specifies the estimated number of times a region contains a thresholded gap length g, for threshold t, in the direction of angle θ, the author showed the differences among GLGLM, GLRLM and LAGLM based on a simple image [see Table 4.9(a)] in Table 4.9. The results in Table 4.9(c), 4.9(b) and 4.9(f) were calculated by assuming the run length of a pixel which has no adjacent pixels of the same gray value as one for GLRLM, the gap length of two neighboring pixels with identical gray level as one for GLGLM, and the gap length of a low-attenuation pixel which has no collinearly adjacent low-attenuation pixels as one for LAGLM.

The calculations of GLGLM-based and GLRLM-based texture features basically correspond to the calculation of LAGLM-based texture features [see Eq. (4.2) to (4.9)]. The only difference is the use of element, namely $r_{LAGLM}(t, g|\theta)$, $r_{GLGLM}(i, v|\theta)$ and $r_{GLRLM}(i, j|\theta)$ for LAGLM, GLGLM and GLRLM, respectively. For example, the calculation of GLGLM's short gap emphasis and GLRLM's short run emphasis correspond to the calculation of LAGLM's thresholded short gap emphasis, and so on. However, owing to the apparent conceptual difference among GLGLM, GLRLM and LAGLM, it results in different values for each corresponding feature.

The underlying rationale of the effectiveness of the proposed algorithm lies in the fact that LAGLM collectively takes into account both of the two key factors for discriminating regional emphysematous severity such as gray level distribution toward the lower end of the range of gray level and the extent of low-attenuation gap lengths in the region. For instance, *LTGE* derived from LAGLM indicates how extensive the low-attenuation gap lengths are toward the lower end of the range of the gray level threshold and therefore it is

Table 4.9: The differences between the proposed LAGLM and the classical texture-based methods such as GLGLM, GLRLM, SGLDM and GLDM, based on a simple image. The inter-sample spacing, d, for SGLDM is one.

(a) a simple image

2	0	2	1
0	1	3	2
2	2	1	0
1	0	0	2

(b) GLGLM: $r_{GLGLM}(i, v|\theta)$

$\theta = 0°$		gap length, v			
		1	2	3	4
gray level, i	0	1	0	0	0
	1	0	0	0	0
	2	1	1	0	0
	3	0	0	0	0

(c) GLRLM: $r_{GLRLM}(i, j|\theta)$

$\theta = 0°$		run length, j			
		1	2	3	4
gray level, i	0	3	1	0	0
	1	4	0	0	0
	2	4	1	0	0
	3	1	0	0	0

(d) SGLDM: $r_{SGLDM}(i, j|d, \theta)$ with inter-sample spacing, $d = 1$

$\theta = 0°$		gray level, j			
		0	1	2	3
gray level, i	0	1	1	2	0
	1	2	0	0	1
	2	1	2	1	0
	3	0	0	1	0

(e) GLDM: $r_{GLDM}(i, j|d, \theta)$

$\theta = 0°$		gray level difference, dif			
		0	1	2	3
inter-sample spacing, d,	1	2	6	4	0
	2	1	4	2	1
	3	0	2	2	0

(f) LAGLM: $r_{LAGLM}(t, g|\theta)$

$\theta = 0°$		thresholded gap length, g			
		1	2	3	4
gray level threshold, t	0	0	0	0	0
	1	3	1	0	0
	2	2	2	1	0
	3	1	1	0	3

able to reflect the extent of regional emphysematous severity. Similarly, LAGLM-based two-threshold features also have approximately the same effect as LAGLM-based texture features in terms of describing the severity of emphysema. It is because LAGLM-based two-threshold features extract the low-attenuation gap length distribution by separating gap lengths into four gap length classes based on a two thresholds: a lower threshold and an upper threshold (–940HU and –960HU). Therefore, the four-class classification accuracies of LAGLM-based texture features and LAGLM-based two-threshold features are approximately the same (see Table 4.6 and Table 4.7).

Chapter 5

Methodology 3: Bullae Congregation Index

5.1 Background

Figure 5.1 shows two simulated images of the lung with different bullae distributions [75] where Fig. 5.1(a) shows sparsely distributed bullae while Fig. 5.1(b) shows densely distributed bullae. Assuming that the lung area is highlighted in black, bullae in the lung area are highlighted in white, the bullae pixel intensities and the bulla sizes are identical in Fig. 5.1(a) and 5.1(b), classical emphysema describing indices like MLD, PI and BI would produce the same values for both of the cases. In other words, classical emphysema describing indices are not expressive for discriminating bullae distribution because these indices are not originally devised for measuring bullae distribution but emphysema severity. To further confirm the usefulness of the standard emphysema describing indices, standard statistical dispersion-based methods and standard texture-based methods for discriminating bullae distribution, the author simulated four images with almost the same bullae sizes but different bullae distributions as shown in Fig. 5.2 and recorded the results of these methods in response to the different bullae distributions in the simulated images as shown in

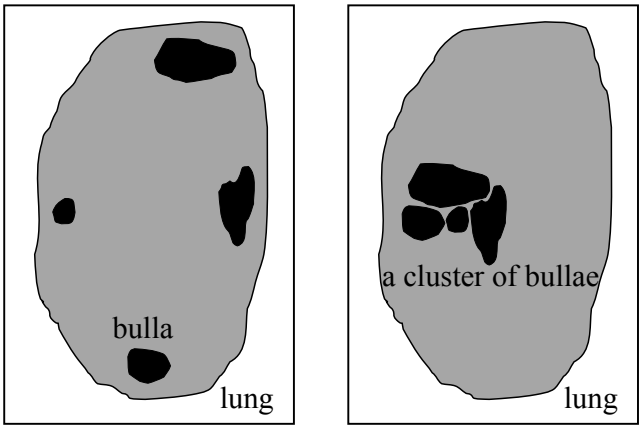

(a) (b)

Fig. 5.1: Different distributions of bullae in the lung regions: (a) bullae congregate in a cluster, and (b) sparsely distributed bullae. Grey and dark regions represent lung parenchyma and bullae, respectively.

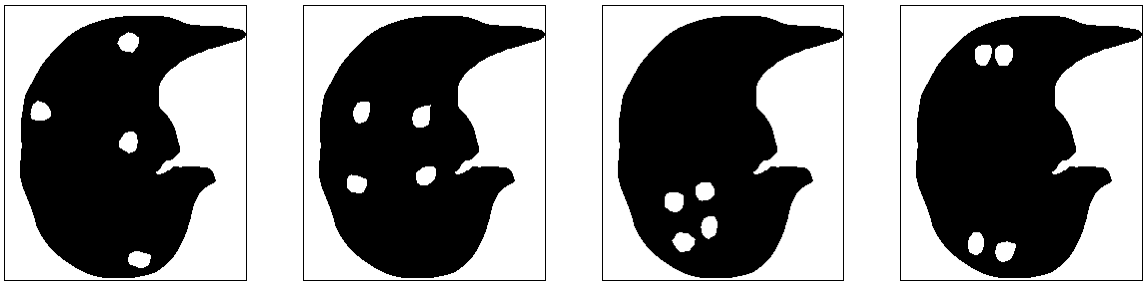

(a) (b) (c) (d)

Fig. 5.2: Four simulated cases of different distributions of bullae in 2D images: case #a, #b, #c, #d, #e, #f, #g and #h. Areas marked white and black are bullae in the lung and lung parenchyma, respectively.

Table 5.1. The standard statistical dispersion-based methods comprise of second moment of distance distribution (SM) [76]and root-mean-square distance ($RMSD$) [77]. The standard texture-based methods comprise of the features generated from SGLDM (see Appendix A.1.3 for the detailed explanation on SGLDM) which is one of the most successful methods for texture discrimination [25]. The features are angular second moment (ASM), contrast (CNT), variance (VAR), sum of variance (SV), sum of entropy (SEP) and entropy (EPY).

As expected, the author finds that there is almost no change of values in PI and BI from image #a to #d despite the obvious change of bullae distribution in these images. This means that PI and BI are not expressive for discriminating bullae distribution. The results of the standard statistical dispersion-based methods, SM and $RMSD$, in image #c and #d suggest that the change of values in these methods is not in good agreement with the visual recognition of the bullae congregation rate in the images. The results of the standard texture-based methods in image #c and #d are almost the same despite the obvious change of bullae distribution in these images. This suggests that these methods are not sufficiently expressive for discriminating bullae distribution. Consequently, the author proposes a new emphysema describing index called bullae congregation index (BCI) that indicates whether bullae gather in a specific area of the lung and form a nearly single mass, and how extensive the mass/cluster of bullae is in the lung. In other words, BCI describes the bullae congregation rate in the lung. BCI is not a texture-based method. The author hypothesizes that BCI correlates to the parameters of PFT (see Appendix A.4 for the explanation on the parameters of PFT) better than the standard emphysema describing indices, standard statistical dispersion-based methods and standard texture-based methods.

The goal of the BCI is to complement the existing set of emphysema describing indices to further approximate CT-based visual radiological diagnosis and produce a more informative emphysema diagnosis. BCI is expected to be especially useful when it comes to distinguishing the bullae congregation rate in the lung for cases with approximately the same PI, BI

Table 5.1: The results of the standard emphysema describing indices, standard statistical dispersion-based methods and standard texture-based methods for the four simulated images.

Image	standard emphysema describing indices		standard statistical dispersion-based methods and standard texture-based methods							
	PI	BI	SM	$RMSD$	ASM	CNT	VAR	SV	SEP	EPY
a	3.38	4.22	0.1496	88.56	0.93	0.0053	0.0322	0.1236	0.0739	0.0755
b	3.34	4.18	0.0495	50.34	0.9309	0.0054	0.0319	0.1222	0.0733	0.0749
c	3.35	4.19	0.1132	76.47	0.93	0.0052	0.0320	0.1228	0.0734	0.0749
d	3.35	4.19	0.1899	98.97	0.9308	0.0053	0.0320	0.1227	0.0733	0.0749

or PI and BI. Note that the BCI is not a specific index for describing emphysema severity.

5.2 Implementation of the BCI

For implementing the BCI, the author first extracts the pixels below –960 HU within the lung regions of the original image. The extracted areas are regarded as the LAAs. Each continuous LAA is regarded as a bulla. Then, the author labels the bullae in the image. In this research, bullae smaller than 2mm^2 are ignored. Note that emphysema is represented by the air-filled regions in the lung and air-filled regions appear as the LAAs in the CT (see Table 1.1). Therefore, the pixel intensity of emphysema in the CT generally ranges from –1000 HU to –900 HU. The gray level threshold for extracting emphysema is usually determined within the range from –900 to –990 HU. In this study, the threshold, –960 HU, is chosen based on the author's experience.

The author calculates the relative distance among the bullae. The distance between bullae m and n is defined as $L_{m,n}$ as shown in Eq. (5.1) where $Q_{m,n}$ is the distance between the centroids of bullae m and n as shown in Fig. 5.3 and r_m is the approximate radius of bullae m. Let N be the number of bullae that are larger than 2mm^2 in the image, assume all bullae in the lung are pure circle in shape, the calculations of $Q_{m,n}$ and r_m for all integers $1 \leq m \leq N$ and $1 \leq n \leq N$ are shown in Eq. (5.2) and (5.3), respectively:

$$L_{m,n} = Q_{m,n} - r_m - r_n, \tag{5.1}$$

where

$$Q_{m,n} = \sqrt{(x_m - x_n)^2 + (y_m - y_n)^2}, \tag{5.2}$$

$$r_m = \sqrt{\frac{v_m}{\pi}}, \tag{5.3}$$

where centroids of bullae m and n are (x_m, y_m) and (x_n, y_n), respectively, and v_m is the area of bullae m. $\boldsymbol{Q}$ is a $N \times N$ square matrix. Assuming that the 2D lung region is tightly fitted

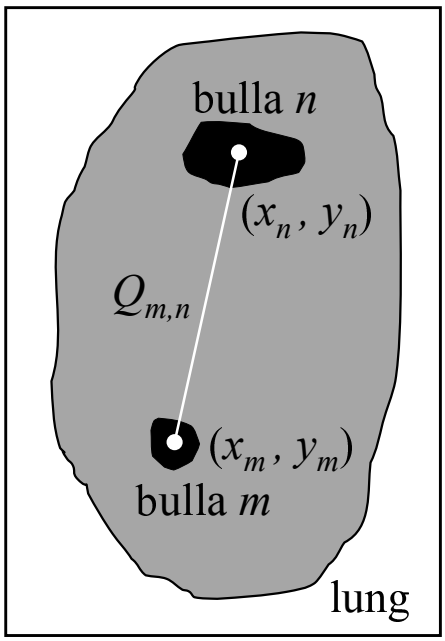

Fig. 5.3: Distance between the centroids of two bullae.

in a rectangle, l is the longest distance from any corner to the other corner of the rectangle, the author defines the distance between a pair of bullae as the ratio of $L_{m,n}$ to l multiplied by 100 as shown in Eq. (5.4):

$$S_{m,n} = \frac{L_{m,n}}{l} \times 100, \tag{5.4}$$

where $\boldsymbol{S}$ is a $N \times N$ square matrix with all right diagonal entries of the matrix assigned with NaN (Not-a-Number). All non-NaN entries in $\boldsymbol{S}$ that are less than zero are assigned with zeros. Hence, $\boldsymbol{S}$ ranges between and including 0 to 100, corresponding to very close proximity between the pair of bullae and to very far distance between the pair of bullae. The author adopts $L_{m,n}$ instead of just $Q_{m,n}$ in Eq. (5.4) to avoid inter-bullae-size variance. The underlying rationale of dividing $L_{m,n}$ by l is to standardize the bulla-to-bulla distance to avoid inter-lung-size variance.

Next, the author generates a vector of 201 linearly spaced points between and including 0 and 100, representing the 200 distance classes of $\boldsymbol{S}$. For example, $0 \leq S_{m,n} < 0.5$ corresponds

to distance class 1 and $99.5 \leq S_{m,n} \leq 100$ corresponds to distance class 200. Theoretically, the larger the number of distance class, the smaller the averaging effect which is caused by the varying distances in each distance class. The author defines 200 distance classes because the author hypothesizes that by using 200 distance classes, the distance class interval of $S_{m,n}$ becomes 0.5 and this interval is already sufficiently small for reducing the variance of distance in each distance class. The validation of the author's hypothesis for the selection of the number of distance class is elaborated in the next chapter: Results and Discussions. The author defines $H_{c,\beta}$ as the average area of the β^{th} pair of bullae that are separated by distance class c where integer $c = 1, 2, 3, ..., 200$. For example, $H_{2,3}$ represents the average area of the 3^{rd} pair of bullae that belongs to distance class 2. Let $total_c$ be the number of pairs of bullae that are separated by distance class c and a be the area of the lung, the author computes the percentage of area of bullae pairs that are separated by distance class c, P_c, as follows:

$$P_c = \frac{\sum_{\beta=1}^{total_c} H_{c,\beta}}{a} \times 100. \tag{5.5}$$

Next, the author defines D as the weighted sum of P_c across the 200 distance classes as shown in Eq. (5.6):

$$D = \frac{\sum_{c=1}^{200}(P_c \times w_c)}{N-1}, \tag{5.6}$$

where $\boldsymbol{w}$ is the weighting function as defined in Eq. (5.7):

$$w_c = \frac{t_c^3 + t_c^2}{40}, \tag{5.7}$$

where t_c represents the c^{th} value in the 200 linearly spaced points between and including seven to one and w_c represents the value of weight that corresponds to distance class c. The weighting function is illustrated in Fig. 5.4. The underlying rationale of the weighting function is that the closer the distance between the bullae, the higher weight is assigned. Note that instead of using just a few distance classes, the author uses 200 distance classes.

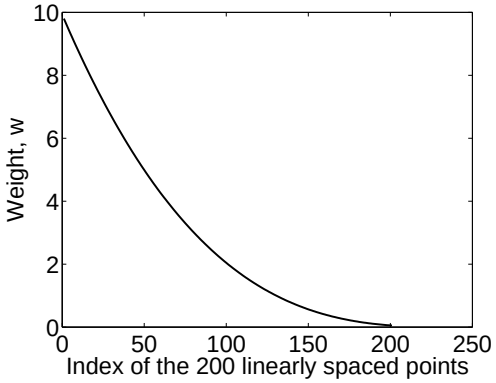

Fig. 5.4: Weighting function.

By doing this, the author substantially reduces the effect of averaging problem, which is caused by the varying bullae sizes in each distance class, on P_c.

Since D is the weighted sum of P_c (the distance-class-based percentage of area of bullae in the lung region), the author infers that using D alone to quantify the congregation of bullae in the lung region is premature because lung with different PI should have different reference value of D for deciding whether bullae congregate in the lung region. In other words, the reference value of D for deciding whether bullae congregate in the lung region is dependent on PI. Accordingly, based on an experiment using 114 images, the author defines BCI as follows:

$$BCI = \begin{cases} D \times cf & : PI > 1, \\ D \times (4/15) & : 0 < PI \leq 1, \\ 0 & : PI = 0, \end{cases} \tag{5.8}$$

where

$$cf = \frac{1 + 3/PI}{15}. \tag{5.9}$$

If BCI is greater than ten, then BCI equals ten. BCI ranges from zero to ten corresponding to sparsely distributed small bullae and to densely distributed big bullae that congregate in

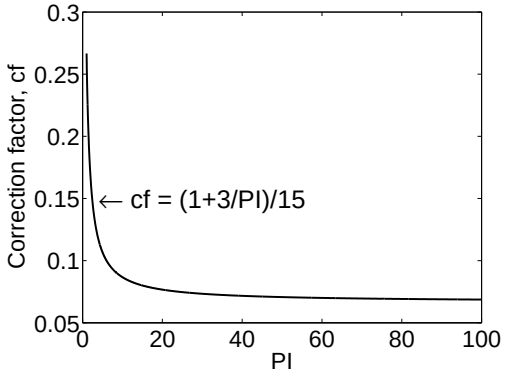

Fig. 5.5: PI versus correction factor, cf.

cluster(s) in the lung region. The relation between PI and cf is illustrated in Fig. 5.5. Note that D is related to the percentage of area of bullae based on 200 bulla-to-bulla distance classes. It is not related to the percentage of bulla-to-bulla distance. This notion originates from the fact that a big emphysematous lesion in the lung is formed by the collapse of a few or many nearby airway walls. Hence, the proposed algorithm treats big bullae as a dense cluster of bullae that have gathered very closely into a mass. Therefore, BCI for two big bullae is higher than that of two small bullae assuming that the bulla-to-bulla distances for both cases are the same. The author defines four bullae congregation classes based on BCI as shown in Table 5.2. These four BCI-based bullae congregation classes are used to compare with the four radiological consensus-classified bullae congregation classes (BCC[§]) as elaborated in the next section.

5.3 Results

To verify the proposed BCI, the author carried out two experiments using simulated images

[§]BCC is the abbreviation for radiological hand-annotated and consensus-classified bullae congregation class. BCC is based on radiologist's manual observation on the degree of bullae congregation in 2D slices. BCC ranges between and including one to four, corresponding to sparsely distributed bullae to densely distributed bullae.

Table 5.2: Four bullae congregation classes based on BCI.

class	range of BCI	interpretation of bullae congregation class
1	$BCI \leq 3.4$	bullae are sparsely distributed in the lung region
2	$3.4 < BCI \leq 4.8$	bullae slightly congregate and are moderately close to each other
3	$4.8 < BCI \leq 6.5$	bullae congregate and are close to each to each
4	$BCI > 6.5$	bullae congregate and are very close to each other forming dense cluster of bullae

and real images, respectively. To compare the author's results with standard statistical dispersion-based methods, the author computed a total of 47 features from spatial gray level dependence method (SGLDM) [25] (15 features), gray level difference method (GLDM) [25] (10 features), gray level run length method (GLRLM) [25] (11 features), gray level histogram method (GLHM) (seven features), second moment of distance distribution (SM) [76] (one feature), root-mean-square distance (RMSD) [77] (one feature), PI and BI. 10 out of the 47 features that showed higher correlation to BCC were chosen to be used to compare with BCI. These 10 features can be divided into three categories: 1) standard emphysema describing indices: PI and BI, 2) standard statistical dispersion-based methods: SM and $RMSD$, and 3) texture-based methods: SGLDM: angular second moment (ASM), contrast (CNT), variance (VAR), sum of variance (SV), sum of entropy (SEP) and entropy (EPY).

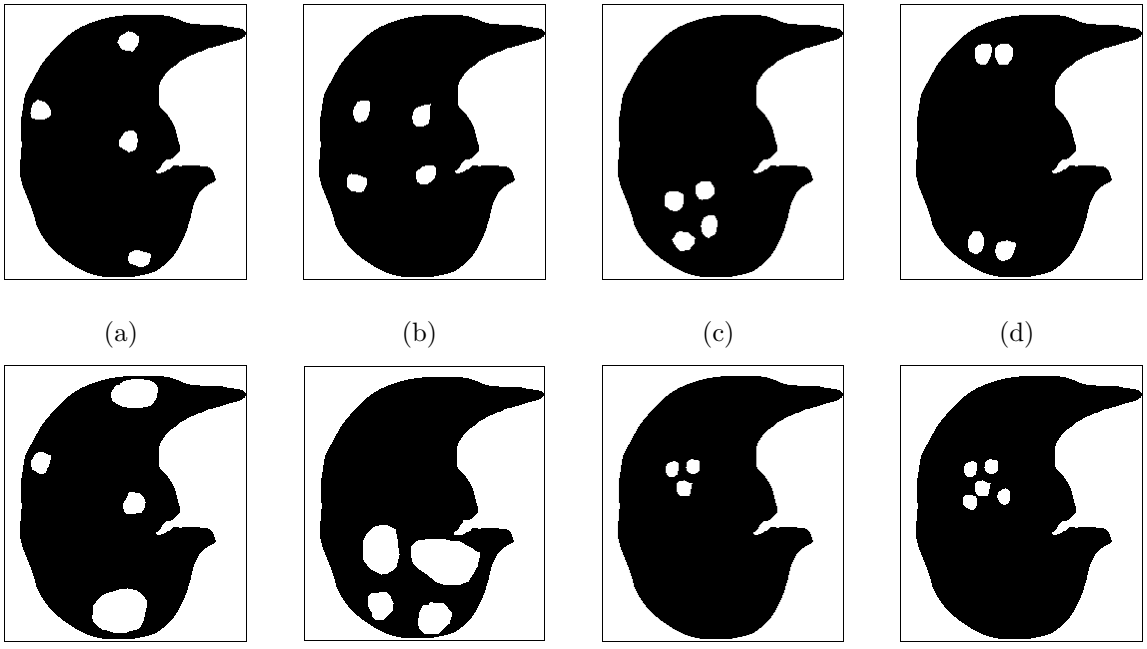

Fig. 5.6: Eight simulated cases of different distributions of bullae in 2D images: case #a, #b, #c, #d, #e, #f, #g and #h. Areas marked white and black are bullae in the lung and lung parenchyma, respectively.

5.3.1 Experiment results based on eight simulated images

Figure 5.6 shows eight simulated 2D images with different bullae distributions. BCI for the simulated images are tabulated in Table 5.3. Case #a, #b, #c and #d show four lungs that have almost the same PI and BI. Among these lungs, the lung with bullae that congregate has higher BCI than the lung with sparsely distributed bullae (see Table 5.3). The author noticed that the outputs of PI, BI, ASM, VAR, SV, SEP and EPY from case #a to #d are almost the same despite the different bullae distributions in these cases. Therefore without manual visual recognition, one can not distinguish the differences of bullae distribution across these four lungs by simply referring to PI, BI, ASM, VAR, SV, SEP or EPY (see Table 5.3). Besides, SM and $RMSD$ do not seem to agree with the

Table 5.3: Standard emphysema describing indices, BCI, standard statistical dispersion-based methods and standard texture-based methods for the simulated cases.

	standard emphysema describing indices		proposed method		standard statistical dispersion-based methods and standard texture-based methods							
#	PI	BI	D	BCI	SM	$RMSD$	ASM	CNT	VAR	SV	SEP	EPY
a	3.38	4.22	12.37	1.56	0.1496	88.56	0.93	0.0053	0.0322	0.1236	0.0739	0.0755
b	3.34	4.18	20.46	2.59	0.0495	50.34	0.9309	0.0054	0.0319	0.1222	0.0733	0.0749
c	3.35	4.19	27.01	3.41	0.1132	76.47	0.93	0.0052	0.0320	0.1228	0.0734	0.0749
d	3.35	4.19	14.00	1.77	0.1899	98.97	0.9308	0.0053	0.0320	0.1227	0.0733	0.0749
e	10.20	5.00	35.87	3.10	0.0166	89.05	0.8102	0.0087	0.0906	0.3535	0.1589	0.1616
f	14.72	5.00	107.33	8.61	0.0081	87.57	0.7410	0.0109	0.1241	0.4856	0.2009	0.2042
g	1.46	1.22	13.04	2.66	0.1433	43.18	0.9686	0.0030	0.0142	0.0537	0.0388	0.0397
h	2.38	1.98	20.22	3.05	0.0689	37.86	0.9492	0.0050	0.0229	0.0868	0.0578	0.0593

visual recognition of bullae congregation rate. This is because for both SM and $RMSD$, outputs for case #1 are higher than that of case #3 although case #1 apparently has lower bullae congregation rate compared to case #3. Consequently, among the methods in Table 5.3, BCI is the most effective index for describing the distributions of bullae from case #a to #d.

Case #a and #e have different PI and BI but the locations of bulleas in both lungs are almost the same. Case #e has much higher BCI compared to case #a owing to its bigger bullae. Also, bullae in case #c and #f are separated by approximately the same relative distances but BCI in case #f is much higher than that of case #c owing to its bigger bullae. Although case #g and #h have smaller bullae compared to case #a and #b, case #g and #h both have higher BCI compared to case #a and #b owing to their more densely located bullae. On the other hand, case #h has higher BCI compared to case #g because of its bigger mass/cluster of bullae.

5.3.2 Experiment results based on 18 sample CT images

18 samples (see Fig. 5.7) drawn from 114 image data set were assessed and the results are tabulated in Table 5.4. Note that PI and BI are indices that indicate the severity of emphysema. BCI is not a specific index for indicating emphysema severity. The purpose of BCI is to provide information about the distribution or congregation rate of bullae in the lung region.

From Table 5.4, BCI increases from case #a to #i indicating increasing bullae congregation rate across the cases (see the distribution of bullae from case #a to #i in Fig. 5.7). Case pairs: #e and #f, #d and #p, #c and #o, and #j and #k, each shows cases with approximately the same PI but different BCI. For instance, in case pair #e and #f, the cluster of bullae located at approximately the upper left of the lung region in case #f is radiologically more obvious and denser than the cluster of bullae located at approximately the middle of the lung region in case #e. Therefore, case #f has higher BCI than case #e.

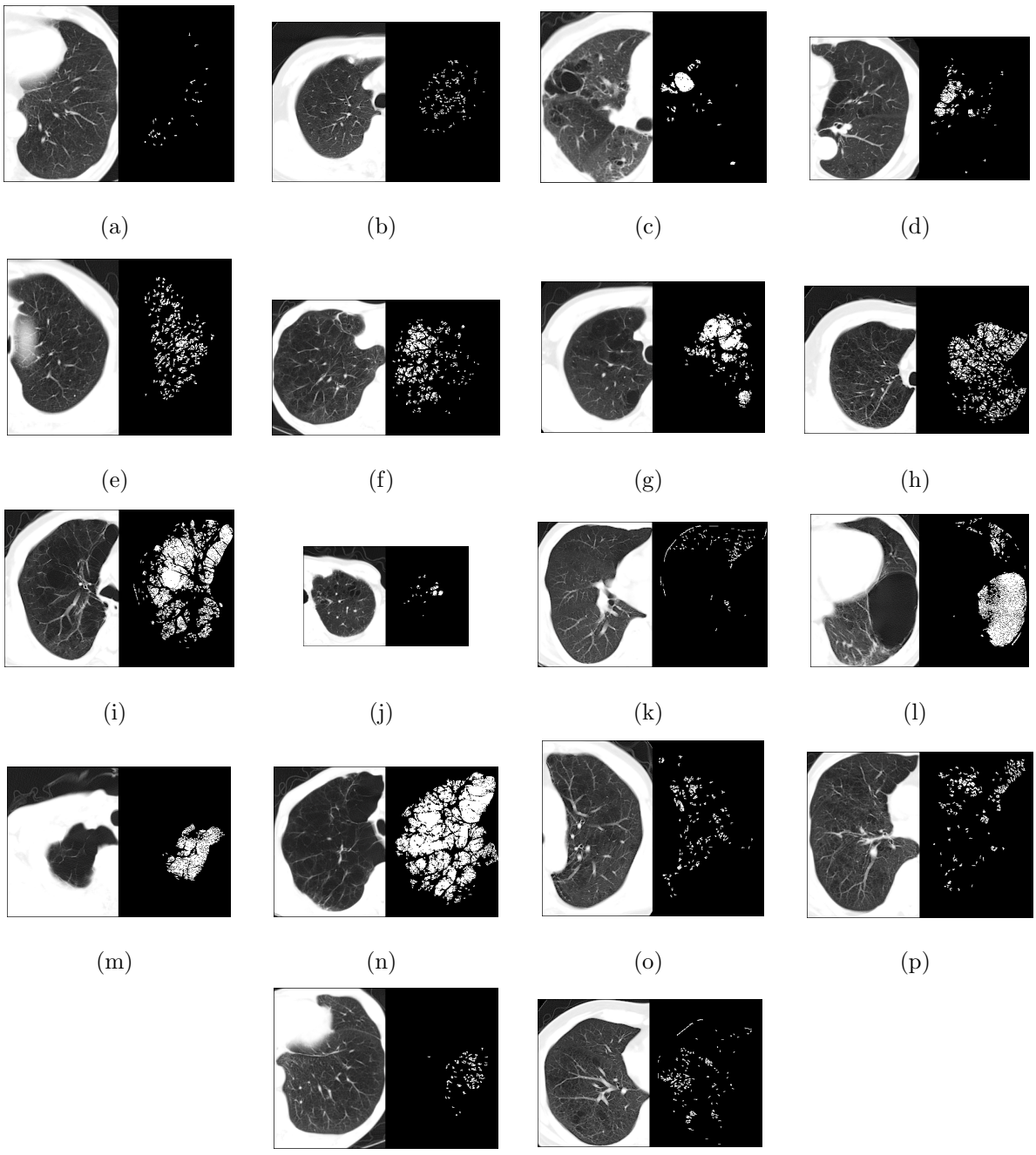

Fig. 5.7: 18 samples of 2D images: case #a to case #r. Areas marked white in in the figures with dark background are areas below –960 HU (bullae). Bullaes smaller than 2mm^2 are not displayed and are ignored in all calculations.

In case pair #d and #p, case #d has higher BCI than case #p owing to its more densely located and bigger bullaes. The same situation happens to case pair #c and #o where the former case has higher BCI than the latter case owing to its more densely located and bigger bullaes. As for case pair #j and #k, case #j has higher BCI than case #k although both cases have almost the same PI. This is because bullae in case #j gather into a small mass while bullae in case #k are sparsely distributed in the lung region.

On the other hand, case pairs: #l and #g, #g and #f, #d and #c, #m and #h, and #n and #h, each shows cases with roughly the same BI but different BCI. For instance, in case pair #l and #g, one can see the formation of a big cluster of bullae in both cases. Case #l has higher BCI than case #g because the cluster in case #l is denser and it covers a bigger ratio of area in the lung region compared to that of case #g. In case pair #g and #f, case #g has higher BCI than case #f owing to its more densely located and bigger bullae. In case pair #d and #c, although bullae sizes in both cases are approximately the same, the congregation of bullae in case #d forms a slightly bigger mass than that of case #c. Therefore case #d has slightly higher BCI than case #c.

In this study, since BCI is derived from D (the weighted sum of the percentage of area of bullae in the lung region based on 200 bulla-to-bulla distance classes), consequently, a bigger bulla is conceptually considered as a dense cluster of bullae that have gathered into a mass. Hence, bigger bulla contributes to higher BCI.

In conclusion, without doing visual examination on lung images and with just the standard emphysema describing indices: PI and BI, of two subjects, one can approximate only the differences in emphysema severity and bullae size between the subjects. BCI blends in to provide more information regarding how densely the bullae are distributed in the lung region. A dense cluster of bullae implies that a significant amount of airway walls in that specific area of the lung are destroyed. BCI is devised to be used along with the existing set of emphysema describing indices (PI and BI) for a more thorough knowledge about the sizes and distribution of bullae in the lung. This knowledge is potentially helpful for

Table 5.4: Standard emphysema describing indices, BCI, standard statistical dispersion-based methods and texture-based methods for the sample cases.

	standard emphysema indices			proposed		standard statistical dispersion-based methods and texture-based methods								BCC
#	MLD	PI (0–100)	BI (0–10)	D	BCI (0–10)	SM	$RMSD$	ASM	CNT	VAR	SV	SEP	EPY	(1–4)
a	-860	0.77	0	4.35	1.16	9.0800	62.72	0.9663	0.0130	0.0104	0.0286	0.0415	0.0454	1
b	-865	3.94	0.13	23.02	2.70	0.8059	47.86	0.8392	0.0656	0.0498	0.1336	0.1463	0.1660	1
c	-798	4.24	3.79	28.10	3.20	0.4329	51.85	0.8965	0.0210	0.0414	0.1447	0.1066	0.1130	1
d	-861	4.95	3.53	31.55	3.38	0.3328	61.97	0.8622	0.0398	0.0498	0.1594	0.1344	0.1464	1
e	-881	9.94	1.94	54.52	4.73	0.3822	59.68	0.6938	0.1175	0.1013	0.2879	0.2468	0.2822	2
f	-885	10.90	5.21	60.50	5.14	0.2093	63.68	0.7027	0.1005	0.1035	0.3136	0.2448	0.2751	3
g	-901	16.57	5.91	94.06	7.41	0.0669	57.22	0.6417	0.0863	0.1398	0.4729	0.2856	0.3116	4
h	-901	23.63	8.49	108.10	8.12	0.0936	61.62	0.4389	0.2366	0.1906	0.5259	0.3932	0.4644	4
i	-912	32.43	9.90	168.46	10.00	0.0483	84.83	0.3875	0.2053	0.2249	0.6941	0.4309	0.4927	4
j	-823	2.66	1.17	16.75	2.38	0.8930	43.59	0.9304	0.0179	0.0260	0.0862	0.0775	0.0829	1
k	-858	2.55	0.25	13.31	1.93	3.0495	103.74	0.8885	0.0449	0.0343	0.0924	0.1095	0.1230	1
l	-864	28.42	5.71	167.51	10.00	0.0424	112.22	0.4540	0.1589	0.2063	0.6662	0.3958	0.4437	4
m	-928	43.49	6.97	306.51	10.00	0.0123	41.12	0.3176	0.2568	0.2464	0.7289	0.4653	0.5426	4
n	-942	52.03	7.18	280.55	10.00	0.0092	82.52	0.3365	0.2087	0.2494	0.7891	0.4594	0.5222	4
o	-866	4.64	0.46	23.92	2.63	1.4659	71.58	0.8332	0.0629	0.0540	0.1530	0.1531	0.1720	1
p	-870	4.94	0.63	25.51	2.73	1.1966	84.76	0.8330	0.0610	0.0549	0.1587	0.1539	0.1723	1
q	-861	2.22	0.09	15.84	2.49	1.2900	43.38	0.9256	0.0275	0.0238	0.0678	0.0801	0.0884	1
r	-855	3.67	0.34	19.12	2.32	1.0718	67.91	0.8514	0.0587	0.0467	0.1281	0.1384	0.1561	1

a followup study on progressive monitoring of emphysema, especially for subjects with the same PI or BI or PI and BI. Note that although the calculation of BCI is related to PI and bullae size, BCI is not proportional to PI or to BI.

5.3.3 Initial investigation: assessment of the BCI using 114 thoracic CT images

To verify whether BCI agrees with BCC, the author compared the BCI-based bullae congregation classes with BCC using 114 CT images which were obtained from the data sets of 31 subjects. The images were hand-annotated and consensus-classified by radiologists into four bullae congregation classes in advance based on the visual impression of bullae congregation rate in the lung region. The author classified the bullae congregation rate of the images into four classes based on BCI. Figure 5.8 shows the relationship between BCI and BCC. Table 5.5 shows the contingency table of the four-class classification results based on the BCI-based bullae congregation classes (see Table 5.2) of the 114 CT images. The four-class classification accuracy using the BCI-based bullae congregation classes is: class 1: 93.10%, class 2: 81.25%, class 3: 82.35% and class 4: 96.15%. The average four-class classification accuracy using BCI is 88.21%. By the way, the author investigated the effect of changing the number of distance classes on the four-class classification accuracy of BCI. The author calculated the four-class classification accuracy of BCI for the case of using 50, 100, 150, 200 and 250 distance classes, respectively. The results showed that the four-class classification accuracy of BCI does not change for the cases of 100, 150, 200 and 250 distance classes; meanwhile, it slightly decreases for the case of 50 distance classes. The author concluded that the problem of averaging effect due to the varying distances in each distance class has an effect on the performance of BCI although the effect is small. Therefore, the author chose 200 as the number of distance class.

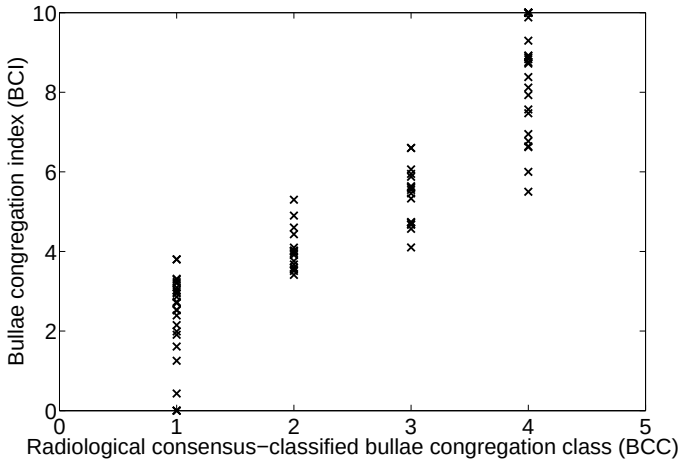

Fig. 5.8: BCC versus BCI.

Table 5.5: The contingency table of the classification of bullae congregation rate of 114 CT images using BCI.

		actual bullae congregation class			
		1 (%) (case)	2 (%) (case)	3 (%) (case)	4 (%) (case)
predicted bullae congregation class	1 (%) (case)	93.10 (27)	0 (0)	0	0
	2 (%) (case)	6.90 (2)	81.25 (13)	5.88 (1)	0
	3 (%) (case)	0	18.75 (3)	82.35 (14)	3.85 (2)
	4(%) (case)	0	0	11.77 (2)	96.15 (50)

Table 5.6: Correlation analyses and assessment of the average four-class classification accuracy of BCI and other methods using 114 CT images.

method	correlation analyses				AFC (%)
	BCC (1–4)		ES (1–4)		
	correlation coefficient	p-value	correlation coefficient	p-value	
BCI	0.9288	< 0.001	0.8468	< 0.001	88.21
PI	0.7821	< 0.001	0.7069	< 0.001	32.69
BI	0.9004	< 0.01	0.9200	< 0.001	72.42
SM	0.3521	< 0.01	0.3342	< 0.01	22.42
$RMSD$	0.3588	< 0.001	0.4212	< 0.001	32.64
ASM	0.7691	< 0.001	0.6643	< 0.001	13.97
CNT	0.8610	< 0.001	0.7063	< 0.001	65.99
VAR	0.9181	< 0.001	0.8180	< 0.001	84.70
SV	0.9053	< 0.001	0.8271	< 0.001	70.93
SEP	0.9183	< 0.001	0.8085	< 0.001	74.88
EPY	0.9162	< 0.001	0.7988	< 0.001	76.35

Table 5.6 shows two correlation analyses: 1) correlation of BCI and other standard methods with BCC, and 2) correlation of BCI and other standard methods with ES[¶]. In the first correlation analysis, the correlation coefficient and p-value of BCI were 0.9388 and less than 0.001, respectively. This shows that BCI significantly correlates with BCC. Besides, BCI's correlation performance with BCC is the highest among all the methods in Table 5.6. Four texture-based methods that are worth notice included VAR, SV, SEP and EPY. Their correlation performances with BCC approach that of BCI. In the second correlation analysis, the author finds that BCI has the second highest correlation with ES after BI among all the methods in Table 5.6. The author concludes that although the

[¶]ES is the abbreviation for emphysema severity class based on pulmonary function tests (PFT) results.

calculation of BCI is related to bullae size, as compared to BI, BCI is not a specific index for indicating emphysema severity.

The author calculated the average four-class classification accuracy, AFC[‖], of BCI and other standard methods based on the BCC of 114 CT images. The results are tabulated in Table 5.6. While the cutoff points for dividing the values of BCI into four classes are 3.4, 4.8 and 6.5, the cutoff points for other standard methods are hand-optimized based on a trial and error basis. From Table 5.6, VAR achieves the highest AFC among the standard methods. This is within the author's expectation because VAR is a measure that provides evidence on the statistical dispersion [78] in the image. The author finds that the proposed non-texture-based method, BCI, is able to perform as good as the texture-based feature, VAR, in terms of classifying bullae congregation rate in 2D images. In fact, based on the author's evaluation using 114 images, BCI achieves slightly higher correlation with BCC and higher AFC as compared to VAR. Besides, BCI evidently outperforms VAR in discerning the different distributions of bullae from case #a to #d of the simulated images (see Fig. 5.6 and Table 5.3 in Section 3.1). VAR is inexpressive for these cases. Hence, this shows the weakness of VAR in quantifying the congregation rate of bullae.

On the other hand, standard statistical dispersion-based methods, SM and $RMSD$, fail to achieve good results in both correlation with BCC and evaluation of AFC (see Table 5.6). This is because SM and $RMSD$ are supposed to measure distance-based statistics between pairs of equivalent objects [77]. However, bullae in the images used in this research are of different shapes and sizes. Hence, they are not supposed to be perceived as equivalent objects. Thus, SM and $RMSD$ are not expressive for measuring the congregation rate of bullae.

In conclusion, BCI is a non-texture-based method for assessing the distribution of bullae in the lung region. The calculation of BCI is computation-wise easier to implement com-

[‖]AFC is the abbreviation for average four-class classification accuracy based on radiological hand-annotated bullae congregation class (BCC).

pared to texture-based methods. BCI is devised to range from zero to ten corresponding to sparsely distributed bullae to densely distributed bullae. As compared to texture-based methods, BCI is an index that is much easier to interpret and more ready to be used by all users including those with minimum knowledge about statistics.

5.3.4 Further investigation: additional comparison between the BCI and VAR

The author's goal is to devise a user-friendly index that is able to discriminate the difference in bullae distribution particularly among cases with approximately the same PI. From Table 5.6 in Section 3.3, the author learned that, in terms of quantifying bullae congregation rate, VAR derived from SGLDM stands out the most among all standard statistical methods examined in this study. Therefore, it is important that the author compares the performance of the proposed method, BCI, with VAR, from this perspective.

Although VAR seems to perform equally well compared to BCI in the framework of four-class classification of bullae distribution, the author learned from the experiments in Fig. 5.6 and 5.7 that VAR, in some cases, produces undesirable values when it comes to discriminating the difference of bullae distribution among cases that belong to the same BCC and among cases with approximately the same PI. For example, bullae distributions in case #a, #b, #c and #d in Fig. 5.6 are apparently different but VAR for these cases are almost the same. This implies that VAR is not able to discriminate the difference of bullae distribution among these cases. The same scenario can be observed in real images such as case #b and #d in Fig. 5.7. These two cases belong to the same BCC. Based on radiologist's visual recognition, case #d has higher bullae congregation rate compared to that of case #b. However, VAR for these cases are almost the same. The same situation happens in case #d and #o in Fig. 5.7 where the former case has denser and bigger cluster of bullae compared to the latter case. However, VAR for case #d is doubtfully lower than that of case #o. While VAR performs poorly in discriminating the difference of bullae distribution among

the above mentioned cases, BCI consistently agree with radiologist's visual impression on bullae congregation rate in these cases. For example, radiologist's visual impression on bullae congregation rate for case #a, #b, #c and #d in Fig. 5.6 in descending order is case #c > #b > #d ≥ #a. The order of BCI in these cases agree with the order annotated by radiologist. In addition, radiologist's visual comparisons of bullae congregation rate between case #b and #d, #j and #k, and #d and #o in Fig. 5.7 are case #d > #b, #j ≥ #k, and #d > #o. Note that, the order of BCI in these cases agree with radiologist's annotations.

Based on the above observations, the author hypothesizes that the performance of BCI is significantly better than that of VAR when it comes to discriminating finer or less obvious difference of bullae distribution among cases that belong to the same BCC and among cases with approximately the same PI. In order to verify the author's hypothesis, the author carried out a series of correlation analyses. The author divided the cases in each class of BCC into two sub-classes and correlated BCI and VAR, respectively, to the sub-classes. Since it is laborious and time consuming for radiologist to manually divide images into more than four bullae congregation classes, the author gathered the cases that belong to the same BCC (class 1, 2, 3 and 4) and requested radiologist to divide the cases in each class into two sub-classes: upper sub-class (higher bullae congregation rate) and lower sub-class (lower bullae congregation rate). For example, both case #b and #d in Fig. 5.7 belong to class 1 of BCC and based on radiologist's annotation, case #d is categorized as upper sub-class while case #b is categorized as lower sub-class. The author evaluated the performance of correlation of BCI and VAR, respectively, to the sub-classes annotated by radiologist. The results of the correlation analyses are shown in Table 5.7. Based on the correlation coefficients in Table 5.7, BCI outperforms VAR in correlation to radiologist-annotated sub-classes especially in cases that belong to class 1, 2 and 3 of BCC, respectively. Next the author gathered two groups of cases with approximately the same PI from the lower end (3% to 5%) and the higher end (15% to 20%) of the range of PI, respectively. The author requested radiologist to divide the cases in each group into two sub-classes: upper sub-class

Table 5.7: Correlation of BCI and VAR, respectively, to the two sub-classes in each BCC (class 1, 2, 3 and 4) and to the two sub-classes in cases with approximately the same PI.

radiologist-annotated sub-classes in a certain class of BCC	BCI (0–10)		VAR	
	correlation coefficient	p-value	correlation coefficient	p-value
class 1 of BCC (29 cases)	0.8384	< 0.001	0.6876	< 0.001
class 2 of BCC (16 cases)	0.5783	0.0189	0.4166	0.1084
class 3 of BCC (17 cases)	0.6637	0.0037	0.4421	0.0756
class 4 of BCC (52 cases)	0.8836	< 0.001	0.8315	< 0.001
approximately same-PI cases (lower PI) (14 cases)	0.6817	0.0431	0.5734	0.1065
approximately same-PI cases (higher PI) (14 cases)	0.6073	0.0475	0.5023	0.1153

(higher bullae congregation rate) and lower sub-class (lower bullae congregation rate). The author evaluated the performance of correlation of BCI and VAR, respectively, to the sub-classes annotated by radiologist. The results of the correlation analyses are shown in Table 5.7. Based on the correlation coefficients in Table 5.7, BCI outperforms VAR in correlation to radiologist-annotated sub-classes in both lower-PI and higher-PI groups.

Table 5.8 describes the general conceptual differences between the calculation of BCI and VAR. Note that, in this study, the images used for calculation are binary images that contain only two values: zero or one. To further confirm that BCI performs better than VAR in corresponding to radiologist's visual recognition of bullae distribution among cases that belong to the same BCC such as case #b and #d in Fig. 5.7 and among cases with approximately the same PI, the author simulated five simple images as shown in Table 5.9 and calculated the BCI and VAR of the images. Pixel with the value of one in the images represents bullae pixel while pixel with the values of zero represents the background of the

Table 5.8: The general conceptual differences between the calculation of BCI and VAR.

concept	BCI	VAR
the definition of one element in the method	one element is represented by one bullae	one element is represented by one pixel
the kind of distance considered in the method	bulla-to-bulla distance	pixel-to-pixel distance
other considerations	1. size of bulla 2. number of bullae	1. number of bullae pixels in the image

image. Note that bulla in the images is represented by continuous pixels of the value of one. For example, there are four, four, two, two, and four bullae in image #1, #2, #3, #4 and #5, respectively. BCI and VAR of the images are shown in Table 5.10. Radiologist's visual impression on the bullae congregation rates of the five images in descending order is image #3 $\approx$ #4 $>$ #2 $\approx$ #1 $>$ #5. BCI in descending order for the five images is image #3 $\approx$ #4 $>$ #2 $\approx$ #1 $>$ #5. VAR in descending order for the five images is image #1 $\approx$ #2 $\approx$ #3 $\approx$ #4 $>$ #5. Therefore, the order of BCI agrees with the the order annotated by radiologist. On the contrary, VAR corresponds poorly to the order annotated by radiologist. In other words, VAR corresponds poorly to the variations of bullae distribution across the images. Note that VAR is irresponsive to the variations in bullae distribution from image #1 to #4.

From the results of correlation analyses in Table 5.7 and the results of experiment in Table 5.10, the author concludes that BCI is more expressive than VAR when it comes to discriminating the difference in bullae congregation rate among cases that belong to the same BCC and among cases with approximately the same PI.

Table 5.9: The five images simulated for experiment purposes (bullae pixel is represented by one in the images).

(a) image #1

0	0	0	0	0	0	0	0	0	0
0	0	0	0	1	1	0	0	0	0
0	0	0	0	0	0	0	0	0	0
0	0	0	0	1	1	0	0	0	0
0	0	0	0	0	0	0	0	0	0
0	0	0	0	1	1	0	0	0	0
0	0	0	0	0	0	0	0	0	0
0	0	0	0	1	1	0	0	0	0
0	0	0	0	0	0	0	0	0	0
0	0	0	0	0	0	0	0	0	0

(b) image #2

0	0	0	0	0	0	0	0	0	0
0	0	0	0	0	0	0	0	0	0
0	0	0	0	1	1	0	0	0	0
0	0	0	0	0	0	0	0	0	0
0	0	1	1	0	0	1	1	0	0
0	0	0	0	0	0	0	0	0	0
0	0	0	0	1	1	0	0	0	0
0	0	0	0	0	0	0	0	0	0
0	0	0	0	0	0	0	0	0	0
0	0	0	0	0	0	0	0	0	0

(c) image #3

0	0	0	0	0	0	0	0	0	0
0	0	0	0	0	0	0	0	0	0
0	0	0	0	1	1	0	0	0	0
0	0	0	0	1	1	0	0	0	0
0	0	0	0	0	0	0	0	0	0
0	0	0	0	1	1	0	0	0	0
0	0	0	0	1	1	0	0	0	0
0	0	0	0	0	0	0	0	0	0
0	0	0	0	0	0	0	0	0	0
0	0	0	0	0	0	0	0	0	0

(d) image #4

0	0	0	0	0	0	0	0	0	0
0	0	0	0	0	0	0	0	0	0
0	0	0	0	1	1	0	0	0	0
0	0	0	0	1	1	0	0	0	0
0	0	0	0	1	1	0	0	0	0
0	0	0	0	0	0	0	0	0	0
0	0	0	0	1	1	0	0	0	0
0	0	0	0	0	0	0	0	0	0
0	0	0	0	0	0	0	0	0	0
0	0	0	0	0	0	0	0	0	0

(e) image #5

0	0	0	0	1	1	0	0	0	0
0	0	0	0	0	0	0	0	0	0
0	0	0	0	0	0	0	0	0	0
0	0	0	0	0	0	0	0	0	0
1	1	0	0	0	0	0	0	1	1
0	0	0	0	0	0	0	0	0	0
0	0	0	0	0	0	0	0	0	0
0	0	0	0	0	0	0	0	0	0
0	0	0	0	0	0	0	0	0	0
0	0	0	0	1	1	0	0	0	0

Table 5.10: Comparing BCI and VAR based on five simulated images.

image #	BCI (0–10)	VAR	PI (0%–100%)
1	4.6686	0.0810	8
2	4.6449	0.0810	8
3	5.3360	0.0810	8
4	5.3360	0.0810	8
5	1.8672	0.0717	8

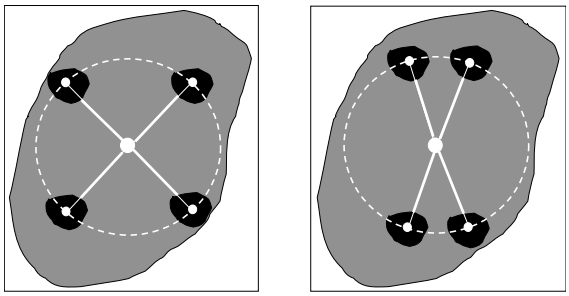

(a) (b)

Fig. 5.9: Distance calculation based on the center point of the lung region for case #a and case #b.

5.4 Discussion

The author did not calculate the distance between bullae based on the center point of the lung region. Assuming that bullae in Fig. 5.9(a) and 5.9(b) are located at equal distance from the center point of the lung region, BCI calculated based on the distance of bullae from the center point of the lung region are the same for both cases despite the different bullae distributions. In fact, the bullae congregation rate in Fig. 5.9(b) is generally considered as slightly higher than that of Fig. 5.9(a) because there is somewhat a formation of two clusters of bullae, in the upper and lower regions of the lung in Fig. 5.9(b).

Chapter 6

Conclusion

In order to facilitate a more thorough knowledge about emphysema for the purpose of diagnosis, the total computer aided diagnostic system is implemented (see Fig. 2.1 in Chapter 2). The system encompasses all three of the proposed methods including the multi-threshold method, the LAGLM and the BCI. Consequently, the system is capable of:

1. Classifying sub-volumetric emphysema severity and visualizing emphysema in three dimensions using the proposed multi-threshold method.

2. Classifying regional radiographic emphysematous patterns using the proposed LAGLM method.

3. Describing emphysema distribution uisng the proposed BCI and the multi-threshold method.

The proposed methods have different goals as mentioned above but they share the same motive which is to further describe and/or quantify the features of emphysema to assist medical experts to realize more objective and informative diagnosis of emphysema. It is essential to acquire more knowledge about emphysema before making a diagnosis due to the limitations of pulmonary function tests and the variance of the accuracy of diagnosis between experienced and inexperienced radiologists. The author is confident that the proposed system

is practical and efficient enough to help radiologists to verify their diagnoses and to facilitate follow-up study on progressive monitoring of the disease. Besides, the proposed system can be used to navigate CT slices in different planes and to identify both local (regional) and global (total) emphysema severity in the lung. Different color are employed to correspond to the different level of emphysema severities/patterns. For example, user can access to the 2D bullae congregation rate of a particular CT slice based on the BCI. User can also access to the regional emphysema severity based on the classified image produced by the LAGLM method (the classified image is located in the upper left of Fig. 2.1). In addition, user can easily interpret the distribution of emphysema severity in the entire lung by referring to the sub-volumetric classes generated by the multi-threshold algorithm as shown in the lower left of Fig. 2.1. The following are the separate conclusions of the proposed methods that are included in the total computer aided diagnostic system.

6.1 The multi-threshold method and visualization of emphysema

From the author's experiments (see Table 3.1, 3.2 and 5.6), the author finds that single-threshold method is premature for quantifying emphysema due to the subtle variations in radiographic gray levels. Therefore, the author proposes a multi-threshold method that utilizes ten thresholds chosen from the emphysema-related threshold range (from –900 HU to –990 HU) to extract the different potential emphysematous areas from CT images. Alongside the use of a neural network as the classifier, the author divides the lung into eight sub-volumes and classify the sub-volumetric emphysema severity into four classes. In conclusion, the author has presented an automated 3D-based multi-threshold method for quantifying emphysema. The author's method is practical and is intended to be used as a computer aided diagnostic tool to facilitate not only the knowledge of emphysema severity but also the knowledge of the distribution of emphysema severity across the entire lung in a more ef-

ficient manner. The author also implements a visualization technique called the transparent lung model for visualizing emphysema in three dimensions. Thus, the proposed algorithm incorporates both 3D quantitative analysis and visualization for producing a more comprehensive, easy-to-interpret (see Table 3.8) and effective medical assistant tool. It has higher correlation with the PFT's parameters compared to the classical emphysema-quantification methods.

The four-class classification accuracy of the proposed method based on the 248 test sub-volumes of the lung obtained from 31 subjects is 89.82%. We hypothesize that both the information of emphysema severity and the distribution of emphysema severity in the entire lung are essential for quantifying emphysema. We validate our hypothesis by showing that the correlation of the proposed method with the parameters of PFT is higher than those of the entire-lung multi-threshold PIs and BIs, and other classical single-threshold methods (see Table 5.6). In short, the author's method integrates the multi-threshold notion with the neural-network-based sub-volumetric classification to produce an algorithm that achieves higher correlation with the parameters of PFT compared to the classical methods.

The relationship between emphysema location and emphysema types (heterogeneity of emphysema) was reported in [34]. Even though, in this study, the author did not investigate the correlation between the location of emphysema and the PFT's parameters, the proposed method can be used to facilitate follow-up study bearing on the correlation between emphysema location and the overall functionality of the lung.

On the other hand, the preliminary assessment based on 30 multi-color-coded images suggests that the extracted color-coded areas in these image are in good agreement with both the visually perceivable and fuzzy emphysematous areas in the original CT images not only in terms of locations but also sizes and shapes [see the comparison between Fig. 3.3(a) and Fig. 3.3(b)]. Consequently, the author believes that the multi-color-coded 2D images can be used for 2D-based assessment of emphysema in follow-up study.

6.2 The LAGLM

The LAGLM aims at quantifying the regional emphysematous patterns in the CT. It takes into account the entire emphysema-related threshold range (from –900 HU to –1000 HU) and the bullae sizes. It is inspired by, but different, from the former texture-based methods. The LAGLM classifies the regional radiographic emphysematous patterns into four classes of severity automatically. Two categories of features were derived from LAGLM: LAGLM-based two-threshold features and LAGLM-based texture features. The effectiveness of these features were verified through cross validation of 55 training regions and classification of 105 test regions that were randomly selected from 270 images (27 subjects).

The algorithm focuses on the regional radiographic patterns in the image and recognizes whether the region is comprised of BE-, BEDE-, DE- or N-oriented lung tissue. The author showed that the proposed algorithm is more expressive in classifying regional radiographic emphysematous patterns into four classes compared to other similar systems such as PI, GLRLM and GLGLM. The proposed algorithm is found to be significantly more effective in discriminating BEDE-oriented tissues from DE- and BE-oriented tissues as compared to PI, GLRLM and GLGLM. Classifying the 2D images in a subject's CT data set using the proposed algorithm facilitates the access to the knowledge about the distribution of the different types of emphysematous tissues across the entire lung. This is particularly interesting for a follow-up study on improving the monitoring of radiographic morphological changes with progression of pulmonary disease. The LAGLM is published in [79].

6.3 The BCI

A new emphysema describing index, namely the bullae congregation index (BCI) is proposed. The BCI quantifies the congregation rate of bullae in 2D thoracic CT. The BCI ranges from zero to ten corresponding to sparsely distributed small bullae and to densely distributed big bullae that congregate in cluster(s) in the lung region. Standard emphysema

describing indices such as the MLD method, the PI and the BI are not expressive for describing the distribution of bullae. Consequently, the BCI is devised to complement the existing set of emphysema describing indices by providing information regarding the distribution of bullae in the lung. Along with the MLD method, the PI and the BI, the BCI helps to produce a more comprehensive description of the emphysematous conditions in the lung. The BCI is particularly useful when it comes to comparing subjects with approximately the same PI or BI or PI and BI. In addition, the implementation of the BCI can be easily extended from 2D to 3D. Hence, the author believes that the BCI may provide potentially helpful information for 3D-based comparison study of emphysema and progressive monitoring of emphysema.

The author evaluated the BCI by comparing the performance of the BCI with those of the standard statistical methods using correlation analyses. Since the VAR derived from the SGLDM method stands out the most among the standard statistical methods in the initial investigation (see Table 5.6 in Section 3.2.3), the author further compared the performance of the BCI with that of the VAR in terms of distinguishing bullae congregation rate among cases that belong to the same BCC and among cases with approximately the same PI. Based on the further investigation (see Table 5.7 and Table 5.10 in Section 3.4), the author finds that the BCI performs better than the VAR among cases that belong to the same BCC and among cases with approximately the same PI. Since the goal is to develop a user-friendly index that is able to discriminate the difference in bullae distribution particularly among cases with approximately the same PI, thus the author concludes that the BCI performs better than the VAR in meeting the goal.

Although the author did not verify as to what extent the difference in bullae distribution could result in the overall lung impairment in this study, the author believes that in order to fully describe the morphology and distribution of emphysema of different sizes in the lung, it is important that the author further explores other emphysema describing indices that describe not only the bullae sizes or the percentage of low attenuation areas but also the

distribution of bullae in the lung to approximate visual radiological diagnosis. The BCI is published in [80].

Appendix A

Appendices

A.1 Classical texture-based methods

A.1.1 GLGLM

The GLGLM method defines a gap as a peak or a valley between two pixels having the same gray level [63]. The GLGLM is a 2D array, $A(g, l|\theta)$, where g is the gray level, l is the gap length, and θ is the search direction. Given an image of $M \times N$ pixels with G gray levels from 0 to $G-1$, and L be the maximum gap length, the element of GLGLM at angle θ, $A(g, l|\theta)$, is defined as the frequency of encounter of gap length l of gray level g in the direction of θ. Several texture features can be extracted from the GLGLM method. Define that

- $A(g, l|\theta)$ is the $(g, l)^{th}$ element of the gap length matrix for a direction θ
- G is the number of gray levels,
- L is the longest gap length,
- l_0 is the start gap length, $l_0 = 0$ or 1,
- n is the number of pixels in the image.

$$\text{Number of Gaps, } m_{00} = NG, \tag{A-1}$$

$$NG = \sum_{g=0}^{G-1}\Big\{\sum_{l=l_0}^{L} A(g,l|\theta)\Big\}, \tag{A-2}$$

$$\text{Center of Mass 1, } \mu_l = \frac{\sum_{g=0}^{G-1}\big\{\sum_{l=l_0}^{L} lA(g,l|\theta)\big\}}{NG}, \tag{A-3}$$

$$\text{Center of Mass 2, } \mu_g = \frac{\sum_{g=0}^{G-1}\big\{\sum_{l=l_0}^{L} gA(g,l|\theta)\big\}}{NG}, \tag{A-4}$$

$$\text{Central Moments 1, } m_{20} = \frac{\sum_{g=0}^{G-1}\big\{\sum_{l=l_0}^{L} (l-\mu_l)^2A(g,l|\theta)\big\}}{NG}, \tag{A-5}$$

$$\text{Central Moments 2, } m_{02} = \frac{\sum_{g=0}^{G-1}\big\{\sum_{l=l_0}^{L} (g-\mu_g)^2A(g,l|\theta)\big\}}{NG}, \tag{A-6}$$

$$\text{Central Moments 3, } m_{11} = \frac{\sum_{g=0}^{G-1}\big\{\sum_{l=l_0}^{L} (l-\mu_l)(g-\mu_g)A(g,l|\theta)\big\}}{NG}. \tag{A-7}$$

The above moment parameters give a good description of the shape of the GLGLM. The features that can be extracted from GLGLM are as follows:

$$SGE = \frac{\sum_{g=0}^{G-1}\big\{\sum_{l=l_0}^{L} \frac{A(g,l|\theta)}{l^2}\big\}}{NG}, \tag{A-8}$$

$$LGE = \frac{\sum_{g=0}^{G-1}\big\{\sum_{l=l_0}^{L} l^2A(g,l|\theta)\big\}}{NG}, \tag{A-9}$$

$$GLF = \frac{\sum_{g=0}^{G-1}\big\{\sum_{l=l_0}^{L} A(g,l|\theta)\big\}^2}{NG}, \tag{A-10}$$

$$GLN = \frac{\sum_{l=l_0}^{L}\big\{\sum_{g=0}^{G-1} A(g,l|\theta)\big\}^2}{NG}, \tag{A-11}$$

$$GP = NG/n, \tag{A-12}$$

$$LGGE = \frac{\sum_{g=0}^{G-1}\big\{\sum_{l=l_0}^{L} \frac{A(g,l|\theta)}{g^2}\big\}}{NG}, \tag{A-13}$$

$$HGGE = \frac{\sum_{g=0}^{G-1}\big\{\sum_{l=l_0}^{L} g^2A(g,l|\theta)\big\}}{NG}, \tag{A-14}$$

where

- SGE — Short Gap Emphasis,
- LGE — Long Gap Emphasis,

- GLF — Gray Level Fluctuation,
- GLN — Gap Length Non-uniformity,
- GP — Gap Percentage,
- $LGGE$ — Low Gray Level Gaps Emphasis,
- $HGGE$ — High Gray Level Gaps emphasis.

A.1.2 GLRLM

The GLRLM method defines a run length as some collinearly adjacent pixels having the same gray value [63, 25]. In GLRLM, the gray level runs are characterized by the gray level of the run, the length of the run and the direction of the run. The GLRLM is based on computing the number of gray level runs of various lengths. The element, $[r'(i, j|\theta)]$, of the gray level run length matrix specifies the estimates number of times a picture contains a run of length j, for gray level i, in the direction of angle θ. The four principal directions are $0°$,

45°,90° and 135°. The features [66, 25] that can be extracted from GLRLM are as follows:

$$SRE = \frac{\sum_{i=0}^{N_G-1}\sum_{j=1}^{N_R}\frac{r'(i,j|\theta)}{j^2}}{T_R}, \quad \text{(A-15)}$$

$$LRE = \frac{\sum_{i=0}^{N_G-1}\sum_{j=1}^{N_R} j^2 r'(i,j|\theta)}{T_R}, \quad \text{(A-16)}$$

$$GLD = \frac{\sum_{i=0}^{N_G-1}\left\{\sum_{j=1}^{N_R} r'(i,j|\theta)\right\}^2}{T_R}, \quad \text{(A-17)}$$

$$RLD = \frac{\sum_{j=1}^{N_R}\left\{\sum_{i=0}^{N_G-1} r'(i,j|\theta)\right\}^2}{T_R}, \quad \text{(A-18)}$$

$$RP = \frac{\sum_{i=0}^{N_G-1}\sum_{j=1}^{N_R}\frac{r'(i,j|\theta)}{j^2}}{T_P}, \quad \text{(A-19)}$$

$$LGRE = \frac{\sum_{i=0}^{N_G-1}\sum_{j=1}^{N_R}\frac{r'(i,j|\theta)}{i^2}}{T_R}, \quad \text{(A-20)}$$

$$HGRE = \frac{\sum_{i=0}^{N_G-1}\sum_{j=1}^{N_R} i^2 r'(i,j|\theta)}{T_R}, \quad \text{(A-21)}$$

$$SRLGE = \frac{\sum_{i=0}^{N_G-1}\sum_{j=1}^{N_R}\frac{r'(i,j|\theta)}{i^2 j^2}}{T_R}, \quad \text{(A-22)}$$

$$SRHGE = \frac{\sum_{i=0}^{N_G-1}\sum_{j=1}^{N_R}\frac{r'(i,j|\theta)i^2}{j^2}}{T_R}, \quad \text{(A-23)}$$

$$LRLGE = \frac{\sum_{i=0}^{N_G-1}\sum_{j=1}^{N_R}\frac{r'(i,j|\theta)j^2}{i^2}}{T_R}, \quad \text{(A-24)}$$

$$LRHGE = \frac{\sum_{i=0}^{N_G-1}\sum_{j=1}^{N_R} i^2 j^2 r'(i,j|\theta)}{T_R}, \quad \text{(A-25)}$$

where N_G is the number of gray levels, and N_R is the number of run lengths in the matrix, T_R is shown below,

$$T_R = \frac{\sum_{i=0}^{N_G-1}\sum_{j=1}^{N_R} r'(i,j|\theta)}{T_R}. \quad \text{(A-26)}$$

T_P is the number of points in the image and the descriptions of the abbreviations used in the calculation are as follows:

- SRE — Short Run Emphasis,
- LRE — Long Run Emphasis,
- GLD — Gray Level Distribution,
- RLD — Run Length Distribution,
- RP — Run Percentage,
- $LGRE$ — Low Gray Level Run Emphasis,
- $HGRE$ — High Gray Level Run Emphasis,
- $SRLGE$ — Short Run Low Gray Level Emphasis,
- $SRHGE$ — Short Run High Gray Level Emphasis,
- $LRLGE$ — Long Run Low Gray Level Emphasis,
- $LRHGE$ — Long Run High Gray Level Emphasis.

A.1.3 SGLDM

The SGLDM method has been reported as one of the most successful methods for texture discrimination [25]. It is based on the estimation of the second order join conditional probability density function, $P(i, j|d, \theta)$: where $\theta = 0°$, $45°$, $90°$ and $135°$. Each $P(i, j|d, \theta)$ is the probability of going from gray level i to gray level j, given that the inter-sample spacing is

d and the direction is given by the angle θ. Given L the number of gray levels,

$$P_x(i|d,\theta) = \sum_{i=0}^{L-1} P(i,j|d,\theta), \tag{A-27}$$

$$P_y(j|d,\theta) = \sum_{j=0}^{L-1} P(i,j|d,\theta), \tag{A-28}$$

$$P_{x-y}(k|d,\theta) = \sum_{i=0}^{L-1}\sum_{j=0}^{L-1} P(i,j|d,\theta) \ (0 \leq k = |i-j| \leq L-1), \tag{A-29}$$

$$P_{x+y}(k|d,\theta) = \sum_{i=0}^{L-1}\sum_{j=0}^{L-1} P(i,j|d,\theta) \ (0 \leq k = i+j \leq 2L-2), \tag{A-30}$$

$$\mu_x = \sum_{i=0}^{L-1} iP(i,j|d,\theta), \tag{A-31}$$

$$\mu_y = \sum_{j=0}^{L-1} jP(i,j|d,\theta), \tag{A-32}$$

$$\sigma_x^2 = \sum_{i=0}^{L-1} (i-\mu_x)^2 P_x(i|d,\theta), \tag{A-33}$$

$$\sigma_y^2 = \sum_{j=0}^{L-1} (j-\mu_y)^2 P_y(j|d,\theta). \tag{A-34}$$

By using the above equations, the features of SGLDM are calculated as follows:

$$ASM = \sum_{i=0}^{L-1}\sum_{j=0}^{L-1}\{P(i,j|d,\theta)\}^2, \tag{A-35}$$

$$CNT = \sum_{k=0}^{L-1} P_{x-y}(k|d,\theta), \tag{A-36}$$

$$CRR = \frac{\sum_{i=0}^{L-1}\sum_{j=0}^{L-1} ijP(i,j|d,\theta) - \mu_x\mu_y}{\sigma_x\sigma_y}, \tag{A-37}$$

$$VAR = \sum_{i=0}^{L-1}\sum_{j=0}^{L-1}(i-\mu_x)^2 P(i,j|d,\theta), \tag{A-38}$$

$$IDM = \sum_{i=0}^{L-1}\sum_{j=0}^{L-1}\frac{P(i,j|d,\theta)}{1+(i-j)^2}, \tag{A-39}$$

$$SAV = \sum_{k=0}^{2L-2} kP_{x+y}(k|d,\theta), \tag{A-40}$$

$$SVR = \sum_{k=0}^{2L-2}(k-SAV)^2 P_{x+y}(k|d,\theta), \tag{A-41}$$

$$SEP = \sum_{k=0}^{2L-2} P_{x+y}(k|d,\theta)log\{P_{x+y}(k|d,\theta)\}, \tag{A-42}$$

$$EPY = \sum_{i=0}^{L-1}\sum_{j=0}^{L-1} P(i,j|d,\theta)log\{P(i,j|d,\theta)\}, \tag{A-43}$$

$$DVR = \sum_{k=0}^{L-1}\Big\{k - \sum_{k=0}^{L-1} kP_{x-y}(k|d,\theta)\Big\}^2 P_{x-y}(k|d,\theta), \tag{A-44}$$

$$DEP = -\sum_{k=0}^{L-1} P_{x-y}(k|d,\theta)log\big\{P_{x-y}(k|d,\theta)\big\}, \tag{A-45}$$

$$IM1 = \frac{EPY - HXY1}{\max\big\{HX, HY\big\}}, \tag{A-46}$$

$$IM2 = \sqrt{[1-\exp\big\{-(HXY2-EPY)\big\}]}, \tag{A-47}$$

where

$$HX = -\sum_{i=0}^{L-1} P_x(i|d,\theta) log\big\{P_x(i|d,\theta)\big\}, \quad \text{(A-48)}$$

$$HY = -\sum_{j=0}^{L-1} P_y(j|d,\theta) log\big\{P_y(j|d,\theta)\big\}, \quad \text{(A-49)}$$

$$HXY1 = -\sum_{i=0}^{L-1}\sum_{j=0}^{L-1} P(i,j|d,\theta) log\big\{P_x(i|d,\theta)P_y(j|d,\theta)\big\}, \quad \text{(A-50)}$$

$$HXY2 = -\sum_{i=0}^{L-1}\sum_{j=0}^{L-1} P_x(i|d,\theta)P_y(j|d,\theta) log\big\{P_x(i|d,\theta)P_y(j|d,\theta)\big\}, \quad \text{(A-51)}$$

where

- ASM — Angular Second Moment,
- CNT — Contrast,
- CRR — Correlation,
- VAR — Variance,
- IDM — Inverse Difference Moment,
- SAV — Sum Average,
- SVR — Sum Variance,
- SEP — Sum Entropy,
- EPY — Entropy,
- DVR — Difference Variance,
- DEP — Difference Entropy,
- $IM1$ — Information Measure of Correlation,
- $IM2$ — Information Measure of Correlation.

A.1.4 GLDM

GLDM describes the gray level difference in the image. Let $f'(r, j)$ be the gray level difference density function given inter-sample spacing distance, r and gray level difference, j, and search

direction θ [64],

$$DGD(j) = \sum_{r=1}^{n_r} f'(r,j), \tag{A-52}$$

$$DOD(r) = \sum_{j=0}^{n_j-1} jf'(r,j), \tag{A-53}$$

$$DAD(j) = \sum_{r=1}^{n_r} rf'(r,j), \tag{A-54}$$

$$LDE = \sum_{j=0}^{n_j-1} DGD(j)ln(K/j), \tag{A-55}$$

$$SHP = \sum_{j=0}^{n_j-1} j^3 DGD(j), \tag{A-56}$$

$$SMG = \sum_{j=0}^{n_j-1} DGD(j)^2, \tag{A-57}$$

$$SMO = \sum_{r=1}^{n_r} DOD(r)^2, \tag{A-58}$$

$$LDEL = \sum_{j=0}^{n_j-1} j^2 DAD(j), \tag{A-59}$$

$$CNT = \sum_{j=0}^{n_j-1} j^2 f'(r,j), \tag{A-60}$$

$$ASM = \sum_{j=0}^{n_j-1} \big\{f'(r,j)\big\}^2, \tag{A-61}$$

$$EPY = \sum_{j=0}^{n_j-1} f'(r,j)log\big\{f'(r,j)\big\}, \tag{A-62}$$

$$MEAN = \sum_{j=0}^{n_j-1} jf'(r,j), \tag{A-63}$$

$$IDM = \sum_{j=0}^{n_j-1} \frac{f'(r,j)}{j^2+1}, \tag{A-64}$$

where

- n_r = the maximum inter-sample spacing distance of r given the search direction θ,
- n_j is the number of gray levels in the image,
- K is a constant (assigned as 1 in this research),
- DGD — Distribution of Gray Level Difference,
- DOD — Distribution of Average Difference,
- DAD — Distribution of Average Distance,
- LDE — Large Difference Emphasis,
- SHP — Sharpness,
- SMG — Second Moment of DGD,
- SMO — Second Moment of DOD,
- $LDEL$ — Long Distance Emphasis for Large Difference.
- CNT — Contrast,
- ASM — Angular Second Moment,
- EPY — Entropy,
- $MEAN$ — Mean,
- IDM — Inverse Difference Moment.

A.2 Algorithm for region-by-region processing

1: **for** $p = 1$ to 27 **do** {*/integer p represents subject number}
2: **for** $s = 1$ to 10 **do** {*/integer s represents image number}

3: $A(s) \Leftarrow$ Area of the lung in image no. s
4: $S_i = 59$ {*/$S_i + 1$ = height of the region}
5: $S_j = 59$ {*/$S_j + 1$ = width of the region}
6: $i = 1$ {*/initial x-coordinate for the scan of qualified region}
7: $j = 1$ {*/initial y-coordinate for the scan of qualified region}
8: $slide_1 = 10$ {*/vertical sliding range of mask region}
9: $slide_2 = 10$ {*/horizontal sliding range of mask region}
10: $size_1$ = number of row in the image {*/vertical limit}
11: $size_2$ = number of column in the image {*/horizontal limit}
12: $run = 1$
13: **while** $run = 1$ **do**
14: **if** $(S_i + 1) > size_1$ **then**
15: break {*/if the vertical limit of the image is smaller than $(S_i + 1)$ then break}
16: **else** $\{(S_j + 1) > size_2\}$
17: break {*/if the horizontal limit of the image is smaller than $(S_j + 1)$ then break}
18: **else** $\{(i + S_i) > size_1\}$
19: break {*/if the mask region spans beyond the vertical limit of the image then break}
20: **end if**
21: $I \Leftarrow$ image no. s {*/store image no. s in variable I}
22: **if** $I(i$ to $(i+S_i), j$ to $(j+S_j))$ is covered by lung region by more than 70% **then**
23: $R \Leftarrow I(i$ to $(i + S_i), j$ to $(j + S_j))$ {*/store the qualified region in variable R}
24: Calculate regional features for region R
25: Classify region R into four emphysema types using neural network
26: Paint region R with the color that corresponds to its emphysema type
27: $j = j + slide_2$ {*/slide the mask region to the right by $slide_2$ pixels}

28: **else**

29: $j = j + 1$ {*/slide the mask region to the right by one pixel}

30: **end if**

31: **if** $j + S_j > size_2$ **then** {*/if the mask region spans beyond the horizontal limit of the image}

32: $j = 1$ {*/slide the mask region back to the leftmost position}

33: $i = i + slide_1$ {*/slide the mask region vertically towards the bottom by $slide_1$ pixels}

34: **end if**

35: **end while**

36: **for** $c = 1$ to 4 **do** {*/four colors corresponded by interger c}

37: $TA(s, c, p) \Leftarrow$ Area of color no. c in image no. s for subject no. p {*/calculate the area of each color on each classified image for the subject}

38: **end for**

39: **end for**

40: **for** $c = 1$ to 4 **do** {*/four colors corresponded by interger c}

41: $MPA(p, c) = \frac{\sum_{s=1}^{s=10} TA(s, c, p)}{\sum_{s=1}^{s=10} A(s)} \times 100$ {*/calculate the percentage of area of each color across 10 images for subject no. p}

42: **end for**

43: **end for**

A.3 Implementation of neural network as a multi-class classifier

A.3.1 Introduction of neural network

A neural network is a computing paradigm that is loosely modeled after cortical structures of the brain. It consists of interconnected processing elements called neurons that work together to produce an output function. The output of a neural network relies on the cooperation of the individual neurons within the network to operate. Processing of information by neural networks is often done in parallel rather than in series (or sequentially). Since it relies on its member neurons collectively to perform its function, a unique property of a neural network is that it can still perform its overall function even if some of the neurons are not functioning. That is, they are very robust to error or failure (i.e., fault tolerant). Neural networks are applied to:

1. Function approximation, or regression analysis, including time series prediction and modeling.

2. Classification, including pattern and sequence recognition, novelty detection and sequential decision making.

3. Data processing, including filtering, clustering, blind signal separation and compression.

Application areas include system identification and control (vehicle control, process control), game-playing and decision making (backgammon, chess, racing), pattern recognition (radar systems, face identification, object recognition and more), sequence recognition (gesture, speech, handwritten text recognition), medical diagnosis, financial applications, data mining (or knowledge discovery in databases), visualization and e-mail spam filtering

A.3.2 Network topology

Multilayer feedforward network is an important class of neural networks. Typically, the network consists of a set of sensory units (source nodes) that constitute the input layer, one or more hidden layers of computation nodes, and an output layer of computation nodes. The input signal propagates through the network in a forward direction, on a layer-by-layer basis. These neural networks are commonly referred to as multilayer perceptrons (MLPs), which represent a generalization of the single-layer perceptron.

The author chose a multilayer perceptron neural network as the classifier for his algorithm because over the past years, multilayer perceptrons have been applied successfully to solve some difficult and diverse problems by training them in a supervised manner with a highly popular algorithm known as the error back-propagation algorithm. This algorithm is based on the error-correction learning rule. As such, it may be viewed as a generalization of an equally popular adaptive filtering algorithm: the ubiquitous least-mean-square (LMS) algorithm for the special case of a single linear neuron.

A multilayer perceptron has three distinctive characteristics [58]:

1. The model of each neuron in the network includes a nonlinear activation function. The important point to emphasize is here is that the nonlinearity if smooth (i.e., differentiable everywhere). A commonly used form of nonlinearity that satisfies this requirement is a sigmoidal nonlinearity defined by the logistic function: $y_j = \frac{1}{1+\exp(-v_j)}$ where v_j is the induced local field (i.e., the weighted sum of all synaptic inputs plus the bias) of a neuron j, and y_j is the output of the neuron. The presence of non-linearities is important because otherwise the input-output relation of the network could be reduced to that of a single-layer perceptron. Moreover, the use of the logistic function is biologically motivated, since it attempts to account for the refractory phase of real neurons.

2. The network contains one or more layers of hidden neurons that are not part of the

input or output of the network. These hidden neurons enable the network to learn complex tasks by extracting progressively more meaningful features from the input patterns (vectors).

3. The network exhibits a high degree of connectivity, determined by the synapses of the network. A change in the connectivity of the network requires a change in the population of synaptic connections or their weights.

It is through the combination of these characteristics together with the ability to learn from experience through training that the multilayer perceptron derives its computing power. Figure A.1 shows an example of the architectural graph of the three-layer (one input layer, one hidden layer and one output layer) neural network. The multilayer perceptron neural network for the first proposed method (the multi-threshold method) consists of one input layer, one hidden layer and one output layer while the multilayer perceptron neural network for the second proposed method (the LAGLM method) consists of one input layer, two hidden layers and one output layer. There are n inputs in the input layer depending on the number of input features and m outputs in the output layer depending on the number of output classes. The number of hidden layers are determined based on the underlying rationale elaborated in Table A.1 [59] and the author's experience from trial and error. Deciding the number of hidden neuron layers is only a small part of the problem compared to determining how many neurons to be used in these hidden layers. Deciding the number of neurons in the hidden layers is a very important part of deciding the overall neural network architecture. Though these layers do not directly interact with the external environment, they have a tremendous influence on the final output [58, 59]. Both the number of hidden layers and the number of neurons in each of these hidden layers must be carefully considered. Using too few neurons in the hidden layers will result in something called underfitting. Underfitting occurs when there are too few neurons in the hidden layers to adequately detect the signals in a complicated data set. Using too many neurons in the hidden layers can result in several problems. First, too many neurons in the hidden layers may result in over fitting. Overfitting

Table A.1: Determining the number of hidden layers.

Number of hidden layers	Result
none	Only capable of representing linear separable functions or decisions.
1	Can approximate any function that contains a continuous mapping from one finite space to another.
2	Can represent an arbitrary decision boundary to arbitrary accuracy with rational activation functions and can approximate any smooth mapping to any accuracy.

occurs when the neural network has so much infomation processing capacity that the limited amount of information contained in the training set is not enough to train all of the neurons in the hidden layers. A second problem can occur even when the training data is sufficient. An inordinately large number of neurons in the hidden layers can increase the time it takes to train the network. The amount of training time can increase to the point that it is impossible to adequately train the neural network. Obviously, some compromise must be reached between too many and too few neurons in the hidden layers. There are many rule-of-thumb methods, as shown in Table A.2, for determining the correct number of neuron to use in the hidden layers as shown in Table A.2 [58, 59]. These three rules provide a starting point for consideration. Ultimately, the selection of an architecture for neural network will come down to trial and error. In this research, the number of neurons in the hidden layer(s) is determined as the rounded value of $(2n/3 + m)$ based on the rule number 2 in Table A.2. The network is fully connected. This means that a neuron in any layer of the network is connected to all the nodes or neurons in the previous layer. Signal flow through the network progresses in a forward direction, from left to right and on a layer-by-layer basis.

Figure A.2 depicts a portion of the multilayer perceptron. Two kinds of signals are

Table A.2: Determining the number of neurons in the hidden layers.

Rule number	Description
1	The number of hidden neurons should be between the size of the input layer and the size of the output layer.
2	The number of hidden neurons should be 2/3 the size of the input layer, plus the size of the output layer.
3	The number of hidden neurons should be less than twice of the size of the input layer.

identified in the network.

1. Function Signals — A function signal is an input signal (stimulus) that comes in at the input end of the network, propagates forward (neuron by neuron) through the network, and emerges at the output end of the network as an output signal. It is worthwhile to refer to such a signal as a function signal for two reasons. First, it is presumed to perform a useful function at the output of the network. Second, at each neuron of the network through which a function signal passes, the signal is calculated as a function of the inputs and associated weights applied to that neuron. The function signal is also referred to as the input signal.

2. Error Signals — An error signal originates at the output neuron of the network, and propagates backward (layer by layer) through the network. It is worthwhile to refer to it as an error signal because its computation by every neuron of the network involves an error-dependent function in one form or another.

The output neurons (computational nodes) constitute the output layers of the network. The remaining neurons (computational nodes) constitute hidden layers of the network. Thus the

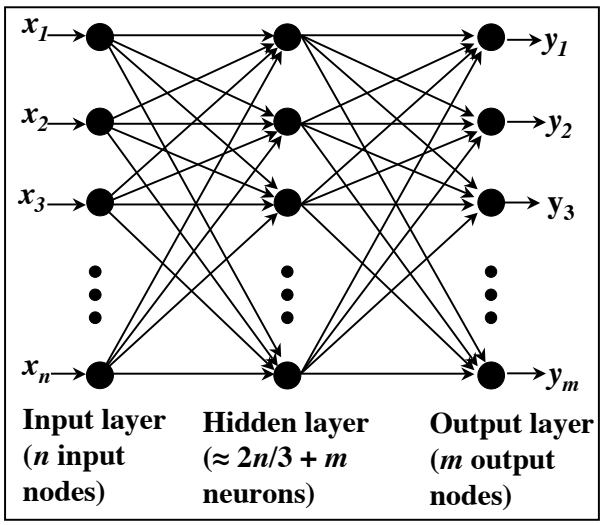

Fig. A.1: An example of a three-layer network topology.

hidden units are not part of the output or input of the network hence their designation as hidden. The first hidden layer if fed from the input layer made up of sensory units (source nodes); the resulting outputs of the first hidden layer are in turn applied to the next hidden layer; and so on for the rest of the network. Each hidden or output neuron of a multilayer perceptron is designed to perform two computations:

1. The computation of the function signal appearing at the output of a neuron, which is expressed as a continuous nonlinear function of the input signal and synaptic weights associated with that neuron.

2. The computation of an estimate of the gradient vector (i.e., the gradients of the error surface with respect to the weights connected to the inputs of a neuron), which is needed for the backward pass through the network.

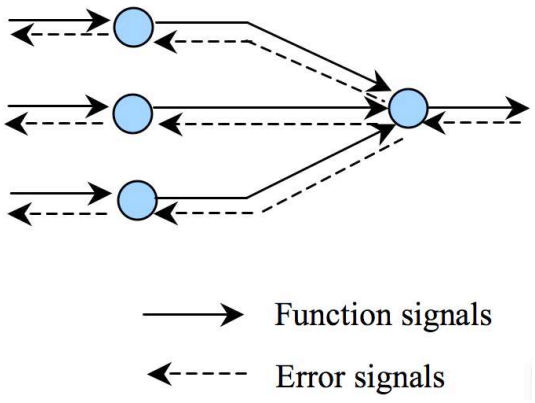

Fig. A.2: Illustration of the directions of two basic signal flows in a multilayer perceptron: forward propagation of function signals and back-propagation of error signals.

A.3.3 Neural network training using the back-propagation learning algorithm

Basically, error back-propagation learning consists of two passes through the different layers of the network: a forward pass and a backward pass [58]. In the forward pass, an activity pattern (input vector) is applied to the sensory nodes of the network, and its effect propagates through the network layer by layer. Finally, a set of outputs is produced as the actual response of the network. During the forward pass the synaptic weights of the networks are all fixed. During the backward pass, on the other hand, the synaptic weights are all adjusted in accordance with an error-correction rule. Specifically, the actual response of the network is subtracted from a desired (target) response to produce an error signal. This error signal is then propagated backward through the network, against the direction of synaptic connections hence the name error back-propagation. The synaptic weights are adjusted to make the actual response of the network move closer to the desired response in a statistical sense. The error back-propagation algorithm is also referred to in the literature as the back-propagation algorithm, or simply back-prop. The process performed with the back-propagation algorithm is called back-propagation learning.

The notation for implementing the back-propagation learning algorithm is illustrated as follows:

- The indices i, j and k refer to different neurons in the network; with signals propagating through the network from left to right, neuron j lies in a layer to the right of neuron i, and neuron k lies in a layer to the right of neuron j when neuron j is a hidden unit.
- In iteration (time step) n, the n^{th} training pattern (example) is presented to the network.
- The symbol $\xi(n)$ refers to the instantaneous sum of error squares or error energy at iteration n. The average of $\xi(n)$ over all values of n (i.e., the entire training set) yields the average error energy $\xi_{av}(n)$.
- The symbol $e_j(n)$ refers to the error signal at the output of neuron j for iteration n.
- The symbol $d_j(n)$ refers to the desired response for neuron j and is used to compute $e_j(n)$.
- The symbol $y_j(n)$ refers to the function signal appearing at the output of neuron j at iteration n.
- The symbol $w_{ji}(n)$ denotes the synaptic weight connecting the output of neuron i to the input of neuron j at iteration n. The correction applied to this weight at iteration n is denoted by $\Delta w_{ji}(n)$.
- The induced local field (i.e., weighted sum of all synaptic inputs plus bias) of neuron j at iteration n is denoted by $v_j(n)$; it constitutes the signal applied to the activation function associated with neuron j.
- The activation function describing the input-output functional relationship of the nonlinearity associated with neuron j is denoted by $\varphi_j(\cdot)$.

- The bias applied to neuron j is denoted by b_j; its effect is represented by a synapse of weight $w_{j0} = b_j$ connected to a fixed input equal to +1.
- The i^{th} element of the input vector (pattern) is denoted by $x_i(n)$.
- The k^{th} element of the overall output vector (pattern) is denoted by $o_k(n)$.
- The learning-rate parameter is denoted by η.
- The symbol m_l denotes the size (i.e., number of nodes) in layer l of the multilayer perceptron; $l = 0, 1, , L$, where L is the depth of the network. Thus m_0 denotes the size of the input layer, m_1 denotes the size of the first hidden layer, and m_L denotes the size of the output layer. The notation $m_L = M$ is also used.

The error signal at the output of neuron j at iteration n (i.e., presentation of the n^{th} training example) is defined by

$$e_j = d_j(n) - y_j(n), \tag{A-65}$$

where neuron j is an output node. We define the instantaneous value of the error energy for neuron j as $\frac{1}{2}e_j^2(n)$. Correspondingly, the instantaneous value $\xi(n)$ of the total error energy is obtained by summing $\frac{1}{2}e_j^2(n)$ over all neurons in the output layer; these are the only visible neurons for which error signals can be calculated directly. Thus,

$$\xi(n) = \frac{1}{2}\sum_{j \in C} e_j^2(n), \tag{A-66}$$

where the set C includes all the neurons in the output layer of the network. Let N denote the total number of patterns contained in the training set. The average squared error energy is obtained by summing $\xi(n)$ over all n and then normalizing with respect to the set size N, as shown by

$$\xi_{av} = \frac{1}{N}\sum_{n=1}^{N} \xi(n). \tag{A-67}$$

The instantaneous error energy $\xi(n)$, and therefore the average error energy ξ_{av}, is a function of all the free parameters (i.e., synaptic weights and bias levels) of the network. For a given training set, ξ_{av} represents the cost function as a measure of learning performance. The objective of the learning process is to adjust the free parameters of the network, which are the synaptic weights of the network, to minimize ξ_{av}. To do this minimization, an approximation similar in rationale to that used for the derivation of the least-mean-square algorithm. Specifically, a simple method of training in which the weights are updated on a pattern-by-pattern basis until one epoch, that is, one complete presentation of the entire training set has been dealt with. The adjustments to the weights are made in accordance with the respective errors computed for each pattern presented to the network.

A.3.4 The two passes of computation

In the application of the back-propagation algorithm, two distinct passes of computation are distinguished. The first pass is referred to as the forward pass, and the second is referred to as the backward pass [58].

In the forward pass the synaptic weights remain unaltered throughout the network, and the function signals of the network are computed on a neuron-by-neuron basis. The function signal appearing at the output of neuron j is computed as

$$y_j(n) \;=\; \varphi(v_j(n)), \tag{A-68}$$

where $v_j(n)$ is the induced local field of neuron j, defined by

$$v_j(n) \;=\; \sum_{i=0}^{m} w_{ji}(n) y_i(n), \tag{A-69}$$

where m is the total number of inputs (excluding the bias) applied to neuron j, and $w_{ji}(n)$ is the synaptic weight connecting neuron i to neuron j, and $y_i(n)$ is the input signal of neuron j or equivalently, the function signal appearing at the output of neuron i. If neuron j is in the first hidden layer of the network, $m = m_0$ and the index i refers to the i^{th} input terminal

of the network, for which

$$y_i(n) \;=\; x_i(n), \tag{A-70}$$

where $x_i(n)$ is the i^{th} element of the input vector (pattern). If, on the other hand, neuron j is in the output layer of the network, $m = m_L$ and the index j refers to the j^{th} output terminal of the network, for which

$$y_j(n) \;=\; o_j(n), \tag{A-71}$$

where $o_j(n)$ is the j^{th} element of the output vector (pattern). This output is compared with the desired response $d_j(n)$, obtaining the error signal $e_j(n)$ for the j^{th} output neuron. Thus the forward phase of computation begins at the first hidden layer by presenting it with the input vector, and terminates at the output layer by computing the error signal for each neuron of this layer.

The backward pass, on the other hand, starts at the output layer by passing the error signals leftward through the network, layer by layer, and recursively computing the δ (i.e., the local gradient) for each neuron. This recursive process permits the synaptic weights of the network to undergo changes in accordance with the delta rule equation as shown below: (Weight correction, $\Delta w_{ji}(n)$) = (learning-rate parameter, η)·(local gradient, $\delta_j(n)$)·(input signal of neuron j, $y_i(n)$).

$$\Delta w_{ji}(n) \;=\; \eta \cdot \delta_j(n) \cdot y_i(n). \tag{A-72}$$

For a neuron located in the output layer, the δ is simply equal to the error signal of that neuron multiplied by the first derivative of its nonlinearity. Eq. (A-72) is used to compute the changes to the weights of all the connection feeding into the output layer.

$$\delta_j(n) \;=\; \varphi_j'(v_j(n)) \sum_k \delta_k(n) w_{kj}(n), \tag{A-73}$$

where neuron j is hidden. Given the δs for the neurons of the output layer, Eq. (A-73) is used to compute the δs for all the neurons in the penultimate layer and therefore the changes

to the weights of all connections feeding into it. The recursive computation is continued, layer by layer, by propagating the changes to all synaptic weights in the network.

A.3.5 Activation function

The computation of the δ for each neuron of the multilayer perceptron requires knowledge of the derivative of the activation function $\varphi(\cdot)$ associated with that neuron. For this derivative to exist, the function $\varphi(\cdot)$ is required to be continuous. In basic terms, differentiability is the only requirement that an activation function has to satisfy. An example of a continuously differentiable nonlinear activation function commonly used in multilayer perceptrons is sigmoidal nonlinearity [58]; two terms are described:

1. Logistic Function — this form of sigmoidal nonlinearity in its general form is defined by

$$\varphi_j(v_j(n)) = \frac{1}{1+\exp(-av_j(n))}, \tag{A-74}$$

where $v_j(n)$ is the induced local field of neuron j. According to this nonlinearity, the amplitude of the output lies inside the range $0 \leq y_j \leq 1$. Differentiating Eq. (A-74) with respect to $v_j(n)$,

$$\varphi'_j(v_j(n)) = \frac{a[\exp(-av_j(n))]}{[1+\exp(-av_j(n))]^2}. \tag{A-75}$$

With $y_j(n) = \varphi_j(v_j(n))$, the exponential term $\exp(-av_j(n))$ is eliminated from Eq. (A-75), and so the derivative $\varphi'_j(v_j(n))$ is expressed as

$$\varphi'_j(v_j(n)) = ay_j(n)[1-y_j(n)], \tag{A-76}$$

2. Hyperbolic tangent function — another commonly used form of sigmoidal nonlinearity is the hyperbolic tangent function, which in its most general form is defined by

$$\varphi_j(v_j(n)) = a\tanh(bv_j(n)), \tag{A-77}$$

where $(a, b) > 0$, a and b are constants. In reality, the hyperbolic tangent function is just the logistic function rescaled and biased.

The logistic function was adopted in the author's algorithm as the activation function for the multilayer perceptron neural network.

A.3.6 Rate of learning

The back-propagation algorithm provides an approximation to the trajectory in weight space computed by the method of steepest descent. The smaller the learning-rate parameter η is made, the smaller the changes to the synaptic weights in the network will be from one iteration to the next, and the smoother will be the trajectory in weight space. This improvement, however, is attained at the cost of a slower rate of learning. If, on the other hand, the learning-rate parameter η is made too large in order to speed up the rate of learning, the resulting large changes in the synaptic weights assume such a form that the network may become unstable (i.e., oscillatory). A simple method of increasing the rate of learning yet avoiding the danger of instability, is by introducing a positive number so called the momentum constant α into the delta rule equation [58].

In the author's algorithm, a learning rate parameter of 0.3 and a momentum constant of 1×10^{-6} were used to achieve an acceptable rate of learning.

A.3.7 Mode of learning

For a given training set, back-propagation learning may proceed in one of two basic ways:

1. Sequential Mode — The sequential mode of back-propagation learning is also referred to as on-line, pattern, or stochastic mode. In this mode of operation weight updating is performed after the presentation of each training example [58]; this is the very mode of operation for which the derivation of the back-propagation algorithm presented applies. To be specific, consider an epoch consisting of N training examples (patterns) arranged

in the order $(x(1), d(1)), , (x(N), d(N))$. The first example pair $(x(1), d(1))$ in the epoch is presented to the network, and the sequence of forward and backward computations described previously is performed, resulting in certain adjustments to the synaptic weights and bias levels of the network. Then, the second example pair $(x(2), d(2))$ in the epoch is presented, and the sequence of forward and backward computation is repeated, resulting in further adjustments to the synaptic weights and bias levels. This process is continued until the last example pair $(x(N), d(N))$ in the epoch is accounted for.

2. Batch Mode — In the batch mode of back-propagation learning, weight updating is performed after the presentation for all the training examples that constitute an epoch.

In the author's algorithm, the sequential mode of training was selected because the sequential mode of training is simple to implement and it provides effective solutions to large and difficult problems.

A.3.8 Stopping the neural network training

In the author's algorithm, the Steady-State Identification (SSID) algorithm [60] was used to stop the neural network training automatically. In this method, the entire 100% of the data gathered is presented for training at each epoch. After each epoch, about 25% of the data is randomly selected as the validation set for that epoch. Therefore, each epoch has a unique validation set. Consequently, if the validation error is plotted versus epoch number, the graph would appear as a noisy signal which approached a steady-state (convergence in the error) as the neural network learns the data. A computationally efficient, automated SSID algorithm [60] can determine when the noisy sum of squares signal stops improving relative to the noise. When this happens, training is terminated.

The SSID algorithm is based on the ratio of variances (R), as measured on the same set of data by two different methods. More precisely, it is the ratio of an estimate of variance

based on the sum of squared differences from the mean (average) to an estimate of variance based on the sum of squared differences between successive data. The relevant equations are:

$$X_{f,i} = \lambda_1 X_i + (1-\lambda_1) X_{f,i-1}, \tag{A-78}$$

$$v^2_{f,i} = \lambda_2 (X_i - X_{f,i-1})^2 + (1-\lambda_2) v^2_{f,i-1}, \tag{A-79}$$

$$\delta^2_{f,i} = \lambda_3 (X_i - X_{i-1})^2 + (1-\lambda_3) \delta^2_{f,i-1}, \tag{A-80}$$

$$R_i = \frac{(2-\lambda_1) v^2_{f,i}}{\delta^2_{f,i}}, \tag{A-81}$$

where

- X_i : Current value of the noisy variable,
- X_{i-1} : Previous value of the noisy variable,
- $X_{f,i}$: Filtered value of the variable,
- $X_{f,i-1}$: Previous filtered value of the variable,
- $v^2_{f,i}$: Current value of the estimate of variance from average,
- $v^2_{f,i-1}$: Previous value of the estimate of variance from average,
- $\delta^2_{f,i}$: Current value of the estimate of variance from successive data,
- $\delta^2_{f,i-1}$: Previous value of the estimate of variance from successive data,
- $\lambda_1, \lambda_2, \lambda_3$: Filter constants,
- R_i : Ratio of variances.

If the process data is at steady-state, R_i will be near unity. A not at steady-state condition is implied by R_i being much greater than unity. The author assigned $\lambda_1 = 0.05$, $\lambda_2 = 0.05$, $\lambda_3 = 0.05$ and $R_{crit} = 1$, since the combination of these values of the parameters improve

the performance of the algorithm. R_{crit} is the threshold value of R_i. The hypothesis that the variable is at steady-state is accepted, if $R_i < R_{crit}$, five times in a row. As a move to improve the speed of response of the algorithm, the value of R_i is not allowed to rise beyond five. This is done by putting a clamp on the value of $v_{f,i}^2$ as:

$$v_{f,i}^2 = \frac{5\delta_{f,i}^2}{(2-\lambda_1)}. \tag{A-82}$$

This measure ensures that as soon as the variable stops changing relative to the noise, the algorithm does not take a long time to identify steady-state, by decreasing R_i from the value five [60]. Figure A.3(b) shows a plot of validation set error (noisy and filtered), steady-state (SS) counter and average squared error energy versus epoch of training where the green line represents the noisy error, the red line represents the filtered value, the dark line represents the SS counter and the blue line represents the average squared error energy. Figure A.3(a) shows a plot of the rate of change of squared error energy versus number of epochs. In this study, the neural network training is stopped when

1. The noisy sum of squared signal stops improving relative to the "noise", which is reflected by the SS counter hitting "1" five times consecutively [60] [see an example in Fig. A.3(a)].

2. The rates of change of squared error energy over the past 10 epochs are less than one [81] [see an example in Fig. A.3(b)].

The noisy error reached a steady state when the SS counter hit "1" five times in a row.

A.3.9 Summary of the back-propagation algorithm

The summary of the back-propagation algorithm is illustrated as follows:

1. Initialization — The synaptic weights and thresholds from a uniform distribution whose mean is zero and whose variance is chosen to make the standard deviation of the induced

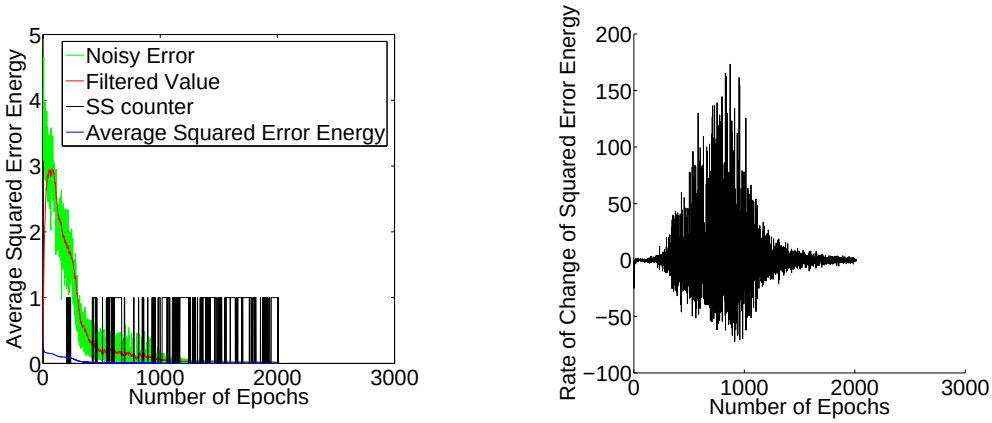

(a) (b)

Fig. A.3: Examples of neural network training results using the SSID stopping criteria: (a) change of average squared error energy versus number of epoch of training, and (b) rate of change of average squared error energy versus number of epoch of training.

local fields of the neurons lie at the transition between the linear and saturated parts of the sigmoid activation function was picked. Each input variable to the multilayer perceptron neural network was normalized to a range of [-1 1].

2. Presentation of Training Examples — The network was presented with an epoch of training examples. For each example in the set, ordered in some fashion, the sequence of forward and backward computations described under point three and four, was performed respectively.

3. Forward Computation — Let a training example in the epoch be denoted by $(x(n), d(n))$, with the input vector $x(n)$ applied to the input layer of sensory nodes and the desired response vector $d(n)$ presented to the output layer of computations nodes. The induced local fields and function signals of the network were computed by proceeding forward through the network, layer by layer. The induced local field $v_j^{(l)}$ for neuron j

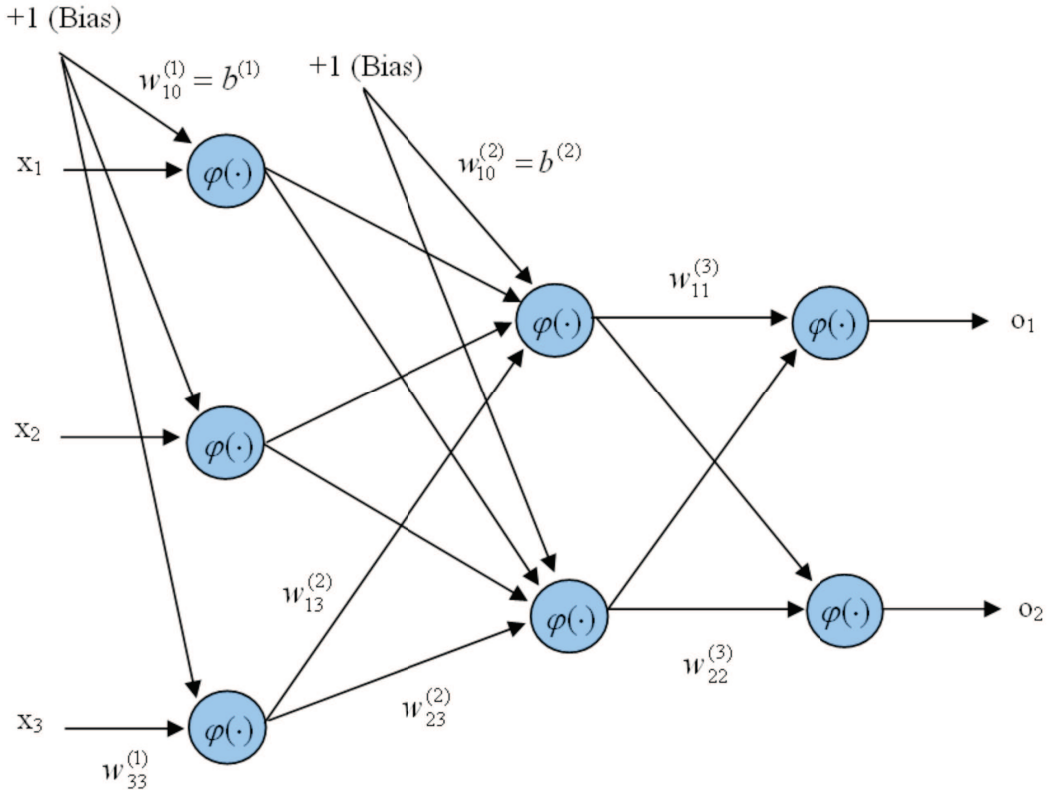

Fig. A.4: Signal-flow graphical summary of a back-propagation learning.

in layer l is

$$v_j^{(l)} = \sum_{i=0}^{m_0} w_{ji}^{(l)}(n) y_i^{(l-1)}(n), \tag{A-83}$$

where $y_i^{(l-1)}(n)$ is the output (function) signal of neuron i in the previous layer $l-1$ at iteration n and $w_{ji}^{(l)}$ is the synaptic weight of neuron j in layer l that is fed from neuron i in layer $l-1$. For $i = 0$, $y_0^{(l-1)}(n) = +1$ and $w_{j0}^{(l)} = b_j^{(l)}(n)$ is the bias applied to neuron j in layer l. The logistic function was used as the activation function and is denoted by $\varphi(\cdot)$. The output signal of neuron j in layer l is

$$y_j^{(l)} = \varphi_j(v_j(n)). \tag{A-84}$$

If neuron j is in the first hidden layer (i.e., $l = 1$), then

$$y_j^{(0)}(n) \quad = \quad x_j(n), \tag{A-85}$$

where $x_j(n)$ is the j^{th} element of the input vector $x(n)$. If neuron j is in the output layer (i.e., $l = L$, where L is referred to as the depth of the network), then

$$y_j^{(L)} \quad = \quad o_j(n). \tag{A-86}$$

The error signal was computed as follow:

$$e_j(n) \quad = \quad d_j(n) - o_j(n), \tag{A-87}$$

where $d_j(n)$ is the j^{th} element of the desired response vector $\boldsymbol{d}(n)$.

4. Backward Computation — The δs (i.e., local gradients) of the network, defined by

$$\delta_j^l(n) = \begin{cases} e_j^{(L)}(n)\varphi_j'(v_j^{(L)}(n)), & \text{for neuron } j \text{ in output layer } L, \\ \varphi_j'(v_j^{(l)}(n)) \sum_k \delta_k^{(l+1)}(n) w_{kj}^{(l+1)}(n), & \text{for neuron } j \text{ in output layer } l, \end{cases} \tag{A-88}$$

where the prime in $\varphi'(\cdot)$ denotes differentiation with respect to the argument. The synaptic weights of the network in layer l was adjusted according to the generalized delta rule:

$$w_{ji}^{(l)}(n+1) \quad = \quad w_{ji}^{(l)}(n) + \alpha[w_{ji}^{(l)}(n-1)] + \eta\delta_j^{(l)}(n) y_i^{(l-1)}(n), \tag{A-89}$$

where η is the learning-rate parameter and α is the momentum constant.

5. Iteration — The forward and backward computations under points three and four were iterated by presenting new epochs of training examples to the network until the stopping criteria was met. The order of presentation of training examples was randomized from epoch to epoch. The momentum and learning-rate parameter were typically adjusted as the number of training iterations increased.

The order of the output node, o_j, that has the greatest output value corresponds to the output class. For example, if o_2 has the greatest output value among the output values, the output class is class two.

A.4 The parameters of pulmonary function test

Spirometry test is one of the many pulmonary function tests. Explanation on the common test values in a spirometry test is shown in Table A.3 [9].

A.5 Diagnosis of COPD

The severity of COPD can be classified using post-bronchodilator spirometry as shown in Table A.4 [7, 8, 9].

A.6 The parameters of pulmonary function test for 15 sample subjects

Table A.5 shows the PFT-based parameters, FEV_1/FVC and $FEV_1\%$ predicted, and classes of the 15 sample subjects based on the guidelines in Table A.4. Note that the content of Table A.5 corresponds to that of Table 3.8 in Chapter 3.

Table A.3: Explanation on the common test values in a spirometry test.

Abbreviation	Name	Description
FVC	Forced Vital Capacity	This is the total amount of air that can forcibly be blown out after full inspiration, measured in liters.
FEV_1	Forced Expiratory Volume in One Second	This is the amount of air that you can forcibly blow out in one second, measured in liters. Along with FVC, it is considered one of the primary indicators of lung function.
FEV_1/FVC	$FEV_1\%$	This is the ratio of FEV_1 to FVC. In healthy adults this should be approximately $75 - 80\%$.
DL_{CO}	Diffusing capacity of the Lung for Carbon Monoxide	This is a measurement of the lung's ability to transfer gases.
VA	Alveolar Volume	Lung capacity or the volume of gas per unit time that reaches the alveoli, the respiratory portions of the lungs where gas exchange occurs.
DL_{CO}VA	Diffusing capacity of the Lung for Carbon Monoxide divided by Alveolar Volume	This is a measurement of the lung's ability to transfer gases divided by lung capacity.

Table A.4: Diagnosis of COPD using post-bronchodilator spirometry.

PFT-based class (severity)	Post-bronchodilator FEV_1	FEV_1% predicted
Normal (1)	> 0.7	≥ 80
Mild COPD (2)	≤ 0.7	≥ 80
Moderate COPD (3)	≤ 0.7	50-79
Severe COPD (4)	≤ 0.7	30-49
Very severe COPD (5)	≤ 0.7	< 30 or 30-50 with Chronic Respiratory Failure symptoms

Table A.5: Diagnoses of the 15 sample subjects based on spirometry test values (FEV_1/FVC and FEV_1%).

Patient no.	FEV_1/ FVC	FEV_1% predicted	Presence of chronic respiratory failure symptoms	PFT-based class
1	0.18	18	Yes	5
2	0.30	40	Yes	5
3	0.32	42	Yes	5
4	0.29	35	No	4
5	0.40	45	No	4
6	0.34	36	No	4
7	0.41	54	No	3
8	0.70	78	No	3
9	0.67	115	No	2
10	0.64	88	No	2
11	0.64	85	No	2
12	0.83	98	No	1
13	0.86	100	No	1
14	0.78	100	No	1
15	0.73	91	No	1

Acknowledgements

First and foremost I offer my sincerest gratitude to my academic supervisor, Prof. Toshiyuki Tanaka, who has supported me throughout my graduate study with his patience and knowledge whilst allowing me the room to work in my own way. Without him this thesis would not have been completed. One simply could not wish for a better or friendlier supervisor.

I would like to thank Dr. Hidetoshi Nakamura from Tokyo Electric Power Hospital, Japan, Dr. Toru Shirahata and Dr. Hiroaki Sugiura from the Division of Pulmonary Medicine, Department of Medicine, Keio University, Japan, for collaborating with me and offering much advice and insight from the perspective of medicine for the purpose of the research presented in this thesis. I am heartily thankful to Prof. Eitaro Aiyoshi, Prof. Satoshi Honda, Prof. Eiji Okada, Prof. Hideo Saito and Prof. Akiyoshi Hatayama from the Faculty of Science and Technology, Keio University, Japan, for their inspirational and constructive comments on my thesis.

I offer my regards and blessings to all of those who supported me in any respect during the completion of this thesis including Mr. Alexandre Suryadi who first helped me get on the road to LaTeX, Dr. Ken Lee Chee Jian who provided me an experienced ear for my doubts about writing thesis using LaTeX, Mr. Tominaga Shunsuke who generously shared with me his knowledge about digital image processing and Mr. Yuji Kitazawa who offered an ear to the problems I encountered.

Finally, I thank my family especially my mother for supporting and helping me unconditionally throughout all my studies at University.

Bibliography

[1] A. G. Webb, *Introduction to Biomedical Imaging*. Wiley Corporate Headquarters, 111 River Street, Hoboken, NJ 07030-5774, USA: Wiley-IEEE Press, 1 ed., Dec 2002.

[2] N. L. Muller, "Advances in imaging," *Eur. Respir. J.*, vol. 18, no. 5, pp. 867–871, 2001.

[3] B. C. M. Association, *Guidelines and Protocols Advisory Committee — Chronic Obstructive Pulmonary Disease (COPD)*. PO Box 9642 STN PROV GOVT Victoria BC V8W 9P1: British Columbia Ministry of Health, 2007.

[4] J. M. Longmore, M. Longmore, I. Wilkinson, and S. R. Rajagopalan, *Oxford Handbook of Clinical Medicine*. Oxford, Oxfordshire: Oxford University Press, 2004.

[5] V. Hodgev, S. Kostianev, G. Hadgigeogiev, I. Todorov, P. Mandulova, and D. Iluchev, "Functional paramters in pulmonary bullous emphysema," *Folia Med.*, vol. 41, no. 1, pp. 157–160, 1999.

[6] R. A. Blechschmidt, R. Werthschutzky, and U. Lorcher, "Automated ct image evaluation of the lung: a morphology-based concept," *IEEE Trans. on Medical Imaging*, vol. 20, no. 5, pp. 434–442, 2002.

[7] G. L. Snider, J. Kleinermann, W. M. Thurlbeck, and Z. H. Bengali, "The definition of emphysema. report of a national heart, lung and blood institute, division of lung diseases workshop," *Amer. Rev. Respir. Dis.*, vol. 132, pp. 182–185, 1985.

[8] W. M. Thurlbeck and N. L. Mueller, "Emphysema: Definition, imaging and quantification," *AJR Amer. J. Roentgenol.*, vol. 163, no. 5, pp. 1017–1025, 1994.

[9] K. F. Rabe, S. Hurd, A. Anzueto, P. J. Barnes, S. A. Buist, P. Calverley, Y. Fukuchi, C. Jenkin, R. R. Roisin, C. V. Weel, and J. Zielinski, "Global strategy for the diagnosis, management, and prevention of chronic obstructive pulmonarry disease: Gold executive summary," *Am. J. Respir. Crit. Care Med.*, vol. 176, no. 6, pp. 532–555, 2007.

[10] M. Zompatori, L. Fasano, A. M. Pacilli, G. Battista, M. Cavina, and S. Pezzi, "Automatic evaluation of total lung capacity and of emphysema involvement with spiral computerized tomography (ct) in obstructive pneumonia," *Radio. Med. (Torino)*, vol. 101, no. 1, pp. 18–24, 2001.

[11] Y. Xu, M. Sonka, J. Guo, and E. A. Hoffman, "Mdct-based 3-d texture classification of emphysema and early smoking related lung pathologies," *IEEE Trans. on Medical Imaging*, vol. 25, no. 4, pp. 464–475, 2006.

[12] K. Yamaguchi and H. Matsubara, "Computed tomographic diagnosis of chronic obstructive pulmonary disease," *Curr. Opinion Pulmonary Med.*, vol. 6, no. 2, pp. 92–98, 2000.

[13] Y. Nakano, H. O. Coxson, S. Bosan, R. M. Rogers, F. C. Sciurba, R. J. Keenan, K. R. Walley, P. D. Pare, and J. C. Hogg, "Core to rind distribution of severe emphysema predicts outcome of lung volume reduction surgery," *American Journal of Respiratory and Critical Care Medicine*, vol. 164, no. 12, pp. 2195–2199, 2001.

[14] W. A. Kalender, R. Rienmuller, W. Seissler, J. Behr, M. Welke, and H. Fichte, "Measurement of pulmonary parenchymal attenuation: use of spirometric gating with quantitative ct," *Radiology*, vol. 175, no. 1, pp. 265–268, 1990.

[15] C. Keyzer and P. A. Gevenois, "Quantitative computed tomography of pulmonary emphysema," *Rev. Mal. Respir.*, vol. 16, no. 4, pp. 455–460, 1999.

[16] H. O. Coxson, R. M. Rogers, K. P. Whittall, Y. D'yachkova, P. D. Pare, F. C. Sciurba, and J. C. Hogg, "A quantification of the lung surface area in emphysema using computed tomography," *American Journal of Respiratory and Critical Care Medicine*, vol. 159, no. 3, pp. 851–856, 1999.

[17] H. Guenard, M. H. Diallo, F. Laurent, and J. vergeret, "Lung density and lung mass in emphysema," *Chest*, vol. 102, no. 1, pp. 198–203, 1992.

[18] S. B. Shaker, A. Dirksen, L. C. Laursen, N. Maltbaek, L. Christensen, U. Sander, N. Seersholm, L. T. Skovgaard, L. Nielsen, and A. Kok-Jensen, "Short-term reproducibility of computed tomography-based lung density measurements in alpha-1 antitrypsin deficiency and smokers with emphysema," *Acta Radiologica*, vol. 45, no. 4, pp. 424–430, 2004.

[19] A. Heremans, J. A. Verschakelen, L. V. Fraeyenhoven, and M. Demedts, "Measurement of lung density by means of quantitative ct scanning. a study of correlations with pulmonary function tests," *Chest*, vol. 102, no. 3, pp. 805–811, 1992.

[20] G. A. Gould, A. T. Redpath, M. Ryan, P. M. Warren, J. J. Best, E. J. Cameron, and W. MacNee, "Parenchymal emphysema measured by ct lung density correlates with lung function in patients with bullous disease," *Eur. Respir. J.*, vol. 6, no. 5, pp. 698–704, 1993.

[21] M. Kinsella, N. L. Muller, R. T. Abboud, N. J. Morrison, and A. DyBuncio, "Quantitation of emphysema by computed tomography using a "density mask" program and correlation with pulmonary function tests," *Chest*, vol. 97, pp. 315–321, Feb. 1990.

[22] M. S. Brown, M. F. M. Gray, N. J. Mankovich, J. G. Goldin, J. Hiller, L. S. Wilson, and D. R. Aberle, "Method for segmenting chest ct image data using an anatomical model: Preliminary results," *IEEE Trans. Med. Imag.*, vol. 16, pp. 828–839, Dec 1997.

[23] R. Uppaluri, T. Mitsa, M. Sonka, E. A. Hoffman, and G. McLennan, "Quantification of pulmonary emphysema from lung computed tomography images," *American Journal of Respiratory and Critical Care Medicine*, vol. 156, no. 1, pp. 248–254, 1997.

[24] R. Uppaluri, G. McLennan, M. Sonka, and E. A. Hoffman, "Interstitial lung disease: a quantitative study using the adaptive multiple feature method," *American Journal of Respiratory and Critical Care Medicine*, vol. 159, no. 2, pp. 519–525, 1999.

[25] A. H. Mir, M. Hanmandlu, and S. N. Tandon, "Texture analysis of ct images," *Engineering in Medicine and Biology Magazine, IEEE*, vol. 14, no. 6, pp. 781–786, 1995.

[26] D. H. Xu, A. S. Kurani, J. D. Furst, and D. S. Raicu, "Run-length encoding for volumetric texture," in *Proc. of Visualization, Imaging and Image Processing*, (Marbella, Spain), Aug 2004.

[27] R. C. Gonzalez, R. E. Woods, and S. L. Eddins, *Digital Image Processing Using MATLAB (DIPUM).* Upper Saddle River, NJ: Prentice Hall, 1st ed., Sep 2004.

[28] A. C. Bovik, M. Clark, and W. S. Geisler, "Multichannel texture analysis using localized spatial filters," *IEEE Trans. on Pattern Analysis and Machine Intelligence*, vol. 12, no. 1, pp. 55–73, 1990.

[29] X. Wang, F. Albregtsen, and B. Foyn, "Grey level gap length matrix: A new approach for texture analysis," in *Proceeding of ICARV'94, 3rd International Conference on Automation, Robotics and Computer Vision*, vol. 2, (Singapore), pp. 648–652, 1994.

[30] E. R. Dougherty, J. B. Pelz, F. Sand, and A. Lent, "Morphological image segmentation by local granulometric size distributions," *Jour. Elec. Imaging*, vol. 1, no. 1, pp. 46–60, 1992.

[31] R. Lerski, "Texture analysis of medical images," in *Proceeding of INternational Symposium on Physics of Medical Imaging and Advances in Computer Applications*, pp. 64–64, 1993.

[32] M. Prasad, "Online feature selection for classifying emphysema in hrct images," *Investigative Radiology*, vol. 1, no. 2, pp. 127–133, 2008.

[33] Y. Park, J. Seo, N. Kim, E. Chae, Y. Oh, S. Lee, Y. Lee, and S. H. Kang, "Texture-based quantification of pulmonary emphysema on high-resolution computed tomography: Comparison with density-based quantification and correlation with pulmonary function test," *Investigative Radiology*, vol. 43, no. 6, pp. 395–402, 2008.

[34] K. Cederlund, U. Tylen, L. Jorfeldt, and P. Aspelin, "Classification of emphysema in candidates for lung volume reduction surgery: a new objective and surgically oriented model for describing ct severity and heterogeneity," *Chest*, vol. 122, pp. 590–596, Mar 2002.

[35] R. M. Rogers, H. O. Coxson, and F. C. Sciurba, "Preoperative severity of emphysema predictive of improvement after lung volume reduction surgery: Use of ct morphometry," *Chest*, vol. 118, pp. 1240–1247, 2000.

[36] Y. Nakano, S. Muro, H. Sakai, T. Hirai, K. Chin, M. Tsukino, K. Nishimura, H. Itoh, P. D. Pare, J. C. Hogg, and M. Mishima, "Computed tomographic measurements of airway dimensions and emphysema in smokers," *American Journal of Respiratory and Critical Care Medicine*, vol. 162, no. 3, pp. 1102–1108, 2000.

[37] H. U. Kauczor, C. P. Heussel, B. Fischer, R. Klamm, P. Mildenberger, and M. Thelen, "Assessment of lung volumes using helical ct at inpiration and expiration: comparison with pulmonary function tests," *AJR. American Journal of Roentgenology*, vol. 171, no. 4, pp. 1091–1095, 1998.

[38] P. J. Mergo, W. F. Williams, R. Gonzalez-Rothi, R. Gibson, P. R. Ros, E. V. Staab, and T. Heimberger, "Three-dimensional volumetric assessment of abnormally low attenuation of the lung from routine helical ct: inspiratory and expiratory quantification," *AJR. American Journal of Roentgenology*, vol. 175, no. 5, pp. 1355–1360, 1998.

[39] A. E. McNamara, N. L. Muller, M. Okazawa, J. Arntorp, B. R. Wiggs, and P. D. Pare, "Airway narrowing in excised canine lungs measured by high-resolution computed tomography," *J. Appl. Physiol.*, vol. 73, pp. 307–316, 1992.

[40] J. Ley-Zaporozhan, S. Ley, O. Weinheimer, S. Iliyushenko, S. Erdugan, R. Eberhardt, A. Fuxa, J. Mews, and H. U. Kauczor, "Quantitative analysis of emphyseam in 3d using mdct: influence of different reconstruction algorithms," *European Journal of Radiology*, vol. 65, no. 2, pp. 235–236, 2008.

[41] A. R. Froese, K. Ask, R. Labiris, T. Farncombe, D. Warburton, M. D. Inman, J. Gauldie, and M. Kolb, "Three-dimensional ct imaging in an animal model of emphysema," *European Respiratory Journal*, vol. 30, pp. 1082–1089, Aug. 2007.

[42] A. A. Postnov, K. Meurrens, H. Weilers, D. V. Dyck, H. Xu, P. Terpstra, and N. M. D. Clearck, "In vivo assessment of emphysema in mice by high resolution x-ray microtomography," *Journal of Microscopy*, vol. 220, no. 1, pp. 70–75, 2005.

[43] A. Dirksen, M. Friss, K. P. Olesen, L. T. Skovgaard, and K. Sorensen, "Progress of emphysema in severe alpha 1-antirypsin deficiency as assessed by annual ct," *Acta Radiologica*, vol. 38, no. 5, pp. 826–832, 1997.

[44] B. C. Stoel, M. E. Bakker, J. Stolk, A. Dirksen, R. A. Stockley, E. Piitulainen, E. W. Russi, and J. H. Reiber, "Comparison of sensitivities of 5 different computed tomography scanners for the assessment of the progression of pulmonary emphysema: a phantom study," *Investigative Radiology*, vol. 39, no. 1, pp. 1–7, 2004.

[45] N. Otsu, "A threshold selection method from gray level histograms," *IEEE Transactions on Systems, Man, and Cybernetics*, vol. 9, no. 1, pp. 62–66, 1979.

[46] M. Prasad, A. Sowmya, and P. Wilson, "Multi-level classification of emphysema in hrct lung images," *Pattern Analysis and Applications Journal*, Sept. 2007 (in press).

[47] S. Joo, W. K. Moon, and H. C. Kim, "Computer-aided diagnosis of solid breast nodules on ultrasound with digital image processing and artificial neural network," in *Proceedings of the 26th Annual International Conference of the IEEE EMBS*, (San Francisco, CA, USA), pp. 1397–1400, Sep 2004.

[48] J. Zaporozhan, S. Ley, and R. Eberhardt, "Paired inspiratory/expiratory volumetric thin-slice ct scan for emphysema analysis: Comparison of different quantitative evaluations and pulmonary function test," *Chest*, vol. 128, pp. 3212–3220, 2005.

[49] T. Saitoh, H. Koba, N. Shijubo, H. Tanaka, and F. Sugaya, "Lobar distribution of emphysema in computed tomographic densitometric analysis," *Invest. Radiol.*, vol. 35, pp. 235–243, 2000.

[50] A. A. Bankier, V. D. Maertelaer, and C. Keyzer, "Pumonary emphysema: Subjective visual grading versus objective quantification with macroscopic morphometry and thin-section ct densitometry," *Radiology*, vol. 211, pp. 851–858, 1999.

[51] D. Chen, R. Chang, W. Chen, and W. Moon, "Computer-aided diagnosis for 3-dimensional breast ultrasonography," *Arch. Surg.*, vol. 138, no. 3, pp. 296–302, 2003.

[52] K. L. Tan, T. Tanaka, H. Nakamura, and A. Ishizaka, "Classification of emphysema using fractal features and neural network," in *Malaysian-Japan International Symposium on Advanced Technology (MJISAT)*, (Kuala Lumpur, Malaysia), Nov. 2007.

[53] D. Hanselman and B. Littlefield, *Mastering MATLAB 6—A Comprehensive Tutorial and Reference*. Upper Saddle River, NJ: Prentice Hall, 2001.

[54] T. Mathworks, *MATLAB, The Language of Technical Computing—Using MATLAB Graphics*. Natick, MA: The Mathworks, Inc., Jan. 1998.

[55] J. F. S. Hill, *Computer Graphics Using Open GL*. Upper Saddle River, NJ: Prentice Hall, 2nd ed., 2001.

[56] F. Labelle and J. R. Shewchuk, "Isosurface stuffing: Fast tetrahedral meshes with good dihedral angles," in *SIGGRAPH Conf.*, (San Diego, California, USA), Aug. 2007.

[57] S. J. Marshall, R. F. Harrison, and R. Kennedy, "Neural classification of chest pain symptoms: a comparative study," in *2nd International Conf. on Artificial Neural Networks*, (Bournemouth, UK), pp. 200–204, Nov. 1991.

[58] S. Haykin, *Neural Networks: A Comprehensive Foundation*. Upper Saddle River, NJ: Prentice Hall, 2nd ed., 1999.

[59] J. T. Heaton, *Introduction to Neural Networks with Java*. Heaton Research, Inc, 2 ed., Oct 2008.

[60] S. Natarajan and R. R. Rhinehart, "Automated stopping criteria for neural network training," in *Proc. of the American Control Conf.*, vol. 4, (Albuquerque, USA), pp. 2409–2413, Jun. 1997.

[61] J. Vikgren, O. Friman, M. Borga, M. Boijsen, S. Gustavsson, A. Ekberg-Jansson, B. Bake, and U. Tylen, "Detection of mild emphysema by computed tomography density measurements," *Acta Radiologica*, vol. 46, no. 3, pp. 237–245, 2005.

[62] O. Weinheimer, T. Achenbach, C. Buschsiewke, C. P. Heussel, T. Uthmann, and H. U. Kauczor, "Quantification and characterization of pulmonary emphysema in multislice-ct: A fully automated approach," in *Medical Data Analysis, Lecture Notes in Computer Science Springer Verlag*, vol. 2868, Oct. 2003.

[63] X. Wang, F. Albregtsen, and B. Foyn, *Theory and Applications of Image Analysis II*. River Edge, NJ, USA: World Scientific Publishing Co., Inc., 1996.

[64] S. I. Kim, K. C. Choi, and D. S. Lee, "Texture classification using run difference matrix," in *Ultrasonics Symposium*, pp. 1091–1100, Aug 1991.

[65] Y. Uchino, "Classification of gastric tumors using image processing," m. eng. thesis, Graduate School of Science and Technology, Keio University, Yokohama, Japan, mar. 2004.

[66] X. Tang, "Texture information in run-length matrices," *IEEE Trans. on Medical Imaging*, vol. 7, no. 11, pp. 1602–1609, 1998.

[67] C. M. Wu, Y. C. Chen, and K. S. Hsieh, "Texture features for classification of ultrasonic liver images," *IEEE Trans. Med. Imaging*, vol. 11, pp. 141–152, 1992.

[68] H. Sujana, S. Swarnamani, and S. Suresh, "Artificial neural networks for the classification of liver lesions by image texture parameters," *Ultrasound Med. Biol.*, vol. 22, no. 9, pp. 1177–1181, 1996.

[69] G. Rahbar, A. C. Sie, G. C. Hansen, J. S. Prince, M. L. Melany, H. E. Reynolds, V. P. Jackson, J. W. Sayre, and L. W. Bassett, "Benign versus malignant solid breast masses: Us differentiation," *Radiology*, vol. 213, pp. 889–894, 1999.

[70] A. N. Esgiar, R. N. G. Naguib, B. S. Sharif, M. K. Bennett, and A. Murray, "Microscopic image analysis for quantitative measurement and feature identification of normal and cancerous colonic mucosa," *IEEE Trans. Inform. Technol. Biomed.*, vol. 2, pp. 197–203, Mar 1998.

[71] T. Randen and J. H. Husoy, "Filtering for texture classification: A comparative study," *IEEE Trans. Pattern Anal. Mach. Intell.*, vol. 21, no. 4, pp. 291–310, 1999.

[72] J. W. Gurney, K. K. Jones, R. A. Robbins, G. L. Gossman, K. J. Nelson, D. Daughton, J. R. Spurzem, and S. I. Rennard, "Regional distribution of emphysema: Correlation of high-resolution ct with pulmonary function tests in unselected smokers," *Radiology*, vol. 183, pp. 457–463, 1992.

[73] P. A. Gevenois, P. D. Vuyst, and V. D. Maertelaer, "Comparison of computed density and microscopic morphometry in pulmonary emphysema," *Am. J. Respir. Crit. Care Med.*, vol. 154, pp. 187–192, 1996.

[74] M. Mura, M. Zompatori, A. Mussoni, L. Fasano, A. M. Pacilli, O. Ferro, M. Schiavina, and M. Fabbri, "Bullous emphysema versus diffuse emphysema: A functional and radiologic comparison," *Respiratory Medicine*, vol. 99, no. 1/2, pp. 171–178, 2005.

[75] N. Sakai, M. Mishima, K. Nishimura, H. Itoh, and K. Kuno, "An automated method to assess the distribution of low attenuation areas on chest ct scans in chronic pulmonary emphysema patients," *Chest*, vol. 106, pp. 1319–1325, 1994.

[76] R. M. Roth and G. Seroussi, "On the second moment of the distance distribution of binary codes," in *International Symposium on Information Theory*, pp. 931–935, Sep 2005.

[77] O. Carugo and J. Sussman, "Statistical validation of the root-mean-square-distance, a measure of protein structural proximity," *Protein Engineering, Design and Selection*, vol. 20, no. 1, pp. 1–5, 2007.

[78] W. H. Press, S. A. Teukolsky, W. T. Vetterling, and B. P. Flannery, *Numerical Recipes: The Art of Scientific Computing*. Cambridge University Press, 1986.

[79] K. L. Tan, T. Tanaka, H. Nakamura, T. Shirahata, and H. Sugiura, "Classification of regional radiographic emphysematous patterns using low-attenuation gap length matrix," *SICE Journal of Control, Measurement, and System Integration*, vol. 2, no. 5, pp. 307–316, 2009.

[80] K. L. Tan, T. Tanaka, H. Nakamura, T. Shirahata, and H. Sugiura, "Quantification of emphysema: A bullae distribution based approach," *SICE Journal of Control, Measurement, and System Integration*, vol. 2, no. 6, pp. 392–400, 2009.

[81] K. L. Tan, T. Tanaka, H. Nakamura, and A. Ishizaka, "A neural network based computer-aided diagnosis of emphysema using ct lung images," in *SICE Annual Conf.*, (Takamatsu, Japan), pp. 703–709, Sep 2007.